Master's thesis

NTNU
Norwegian University of Science and Technology
Faculty of Engineering
Department of Marine Technology

Vebjørn Nicholas Brevik

Elasticity, Wave Load Modeling and Upscaling of Spar Floating Wind Turbine

Master's thesis in Marine Technology
Supervisor: Erin Bachynski
June 2021

NTNU
Kunnskap for en bedre verden

Vebjørn Nicholas Brevik

Elasticity, Wave Load Modeling and Upscaling of Spar Floating Wind Turbine

Master's thesis in Marine Technology
Supervisor: Erin Bachynski
June 2021

Norwegian University of Science and Technology
Faculty of Engineering
Department of Marine Technology

NTNU
Norwegian University of
Science and Technology

Elasticity, Wave Load Modeling and Upscaling of Spar Floating Wind Turbine

Master Thesis in Marine Technology

Vebjørn Nicholas Brevik

Spring 2021

NTNU

Norwegian University of Science and Technology
Faculty of Engineering and Technology
Department of Marine Technology

Abstract

This thesis investigates elasticity, wave modeling and upscaling of spar-type floating wind turbine (FWT) foundations. A literature review was conducted to gain information about the topics. A method for computing the radiation and diffraction pressures from linear potential flow theory and implementing it to an elastic structure was adapted from Svendsen [33]. A 10 MW spar developed by Hegseth et al. [17] was used to support the 10 MW DTU wind turbine [4]. An upscaled version of the 10 MW spar was made to support the 15 MW IEA wind turbine [1] and a tower developed by Gaertner et al. [15].

Four models were created for the 10 MW spar; a model with rigid hull and wave loads based on linear potential flow theory (PFT, using HydroD), a model with rigid hull and wave loads according to Morison's equation (ME), a flexible model based on ME and a flexible model based on linear PFT (using WAMIT). The same four concepts was used for the upscaled spar. Aero-hydro-servo-elastic analysis was performed using SIMA, and the aerodynamics of the wind turbines are based on blade element momentum (BEM) theory. The flexible models are based on beam theory and created using RIFLEX elements. Rigid models are represented by rigid body dynamics, and panel models made in GeniE are used.

The upscaled spar displayed similar hydrodynamic behavior to the 10 MW spar. PFT and ME models had similar wave excitations for small wave frequencies, but ME exhibited larger excitations for large freqencies ($\omega > 1$). The added mass was greater for the ME models in surge and pitch. Damping was similar for both PFT models, except that WAMIT estimates a larger value in pitch. Radiation damping was not included in the ME models. Constant wind tests verified expected rotor behavior. The natural periods found from decay tests were similar in surge, heave and pitch, but the yaw period is larger for the rigid models. Natural bending frequencies at the tower base were well within the stiff-stiff region for the 10 MW models, and the rigid models had higher natural frequencies. 15 MW models had natural frequencies closer to the blade passing frequency (3p), and the PFT models displayed larger frequencies.

Response amplitude operators (RAO) produced from regular waves tests expressed similar results in surge, heave and pitch, apart from a deviation in heave for the flexible ME model. Bending moment RAOs showed that the bending moment is most significant at the tower's base and top of the spar. The bending stress RAOs displayed an even distribution along the 10 MW towers, while the 15 MW towers had larger stress at the middle. ME models exhibited larger values in surge, pitch, moment and stress for $\omega > 1$, and the 15 MW ME models showed a more considerable difference to PFT. Irregular waves tests were performed for fifteen sea conditions, and the fatigue damage was larger for the ME models for low peak periods (T_p). Damage equivalent loads (DELs) did not show the same deviation between ME and PFT. The spectral analysis revealed that surge and pitch are mainly excited by wind. The bending moment spectra showed small peaks close to the natural bending frequencies. For condition 4 ($T_p = 5$ s), the ME models were significantly excited at the natural frequencies compared to PFT models.

In conclusion, the upscaling was successful and the rotors behaved as expected. The inertia from ballast was missing for the flexible models, which explains why the natural periods in yaw were larger for rigid spars. Inspections were made to ensure the yaw motion was small. The natural bending frequencies for the 15 MW FWTs were closer to 3p since it is longer and the increase in steel weight for the hull was minimized (only 36% larger mass than the original spar). RAOs for the motions verified that the models behaved similarly, except for the flexible ME model in heave. Heave motion was small for the spars and should not have affected the results. The different stress distributions along the towers can be explained by the 10 MW tower being an optimized design that likely had the same maximum stress constraint for all sections. In contrast, the 15 MW tower is a more conventional tower. The ME models overestimated the wave excitations for $\omega > 1$ since the method assumes large wave periods. That lead to larger moment, stress and fatigue damage for low wave periods. The natural bending frequencies were excited by waves for 15 MW models, but the natural frequencies for 10 MW models were well outside the wave frequency region. They could have been excited by a multiple of 3p. This suggested that other excitations than waves can be affected by choice of wave load model.

Sammendrag

Denne oppgaven undersøker elastisitet, bølgelast modellering og oppskalering av flytende vindturbiner med spar fundament. En litteraturstudie ble gjennomført for å få samle inn informasjon om emnene. En metode for å beregne stråling og diffraksjonstrykk fra lineær potensialstrømningsteori og implementere det til en elastisk struktur ble brukt basert på Svendsen [33]. En 10 MW spar utviklet av Hegseth et al. [17] ble brukt til å støtte 10 MW DTU vindturbinen [4]. En oppskalert versjon av 10 MW sparen ble laget for å støtte 15 MW IEA vindturbinen [1] og et tårn utviklet av Gaertner et al. [15].

Fire modeller ble laget for 10 MW sparen; en modell med stivt skrog og bølgelaster basert på lineær potensialstrømningsteori (PFT, ved bruk av HydroD), en modell med stivt skrog og bølgelaster i henhold til Morisons ligning (ME), en fleksibel modell basert på ME og en fleksibel modell basert på lineær PFT (ved bruk av WAMIT). De samme fire konseptene ble brukt for den oppskalerte sparen. Aero-hydro-servo-elastiske analyser ble utført ved bruk av SIMA, og aerodynamikken til vindturbinene er basert på teorien om "blade element momentum" (BEM) teorien. De fleksible modellene er basert på bjelketeorien og laget med RIFLEX-elementer. Stive modeller er representert med "rigid body" dynamikk, og panel-modeller laget i GeniE ble brukt.

Den oppskalerte sparen viste lignende hydrodynamisk oppførsel som 10 MW sparen. PFT- og ME-modeller hadde lignende bølgeekspitasjoner for små bølgefrekvenser, men ME utviste større eksitasjoner for store frekvenser ($\omega > 1$). Tillegsmassen var større for ME-modellene i jag og trim. Dempning var lik for begge PFT-modellene, bortsett fra at WAMIT estimerer en større verdi i trim. Strålingsdemping var ikke inkludert i ME-modellene. Konstant vindtester bekreftet forventet rotoradferd. De naturlige periodene som ble funnet fra "decay testene" var like i surge, hiv og trim, men gir er større for de stive modellene. Naturlige bøyefrekvenser ved tårnbunnen var godt innenfor "stiff-stiff" regionen for 10 MW-modellene, og de stive modellene hadde høyere naturlige frekvenser. 15 MW-modeller hadde naturlige frekvenser nærmere bladets passeringsfrekvens (3p), og PFT-modellene viste større frekvenser.

"Response amplitude operators" (RAO) ble laget basert på resultatene fra regulære bølgetester, og uttrykte lignende resultater i jag, hiv og trim, bortsett fra et avvik i hiv for den fleksible ME-modellen. Bøyemoment RAO viste at bøyemomentet er størst ved tårnets base og toppen av sparen. RAOs for bøyespenningen viste en jevn fordeling langs 10 MW tårnene, mens 15 MW tårnene hadde større belastning i midten. ME-modeller viste større verdier i jag, trim, moment og spenning for $\omega > 1$, og 15 MW ME-modellene viste en mer betydelig forskjell fra PFT. Irregulære bølgetester ble utført for femten sjøforhold, og utmattelsesskaden var større for ME-modellene for lave bølgeperioder (T_p). "Damage equivalent loads" (DEL) viste ikke det samme avviket mellom ME og PFT. Spektralanalysen avslørte at surge og trim hovedsakelig var eksitert av vind. Bøyemomentsspektrene viste små topper nær de naturlige bøyefrekvensene. For tilstand 4 ($T_p = 5$ s) ble ME-modellene betydelig eksitert for de naturlige frekvensene sammenlignet med PFT-modeller.

For å konkludere, så var oppskaleringen vellykket og rotorene oppførte seg som forventet. Tregheten fra ballast manglet for de fleksible modellene, noe som forklarer hvorfor de naturlige periodene i gir var større for stive spar. Det ble gjort inspeksjoner for å sikre at gir var liten i testene. De naturlige bøyefrekvensene for 15 MW FWT var nærmere 3p siden den er lengre og økningen i stålvekt for skroget var minimal (bare 36% større masse enn den opprinnelige sparen). RAOs for bevegelsene bekreftet at modellene oppførte seg

på samme måte, bortsett fra den fleksible ME-modellen i hiv. Hiv bevegelsen var liten for sparene og burde ikke ha påvirket resultatene. De forskjellige spenningsfordelingene langs tårnene kan forklares med at 10 MW tårnet er et optimalisert design som sannsynligvis hadde samme maksimale spenningsbegrensning for alle seksjoner. Derimot er 15 MW tårnet et mer konvensjonelt tårn. ME-modellene overvurderte bølgeekspitasjonene for $\omega > 1$ siden metoden forutsetter store bølgeperioder. Det fører til større moment, spenning og utmattelseskader for lave bølgeperioder. De naturlige bøyefrekvensene ble eksitert av bølger for 15 MW-modeller, men de naturlige frekvensene for 10 MW-modeller var godt utenfor bølgefrekvensområdet. De kan ha blitt eksitert av en "multiple" av 3p. Dette antyder at andre eksitasjoner enn bølger kan påvirkes av valg av bølgelastmodell.

Preface

This master's thesis is submitted as a final assignment for obtaining a Master of Science degree in Marine Technology at the Norwegian University of Science and Technology (NTNU). The thesis was conducted during the spring of 2021 at the Department of Marine Technology in Trondheim, Norway.

I am immensely grateful to my supervisor, Professor Erin Bachynski-Polić from the Department of Marine Technology, for her invaluable support throughout this project. The amount of time and effort she put into guiding me went beyond my expectations. From sharing her expertise within floating wind turbines and SIMA (among other subjects), I gained more understanding within a short period of time than I would ever be able to learn on my own.

I would like to thank Jørgen Kvaleid (COWI) for sharing his knowledge and experience in order to make the thesis more relevant for the wind industry. Furthermore, I want to thank Vetle Kallåk (COWI) for providing me with information regarding damage equivalent loads.

I also want to express my gratitude to Stian Høegh Sørum (Department of Marine Technology) for allowing me to use the control system he developed for a 15 MW turbine, and for his helpful and swift response while I was implementing it for my models. The 15 MW tests would not have been feasible without this controller.

Vebjørn N. Brevik

Vebjørn N. Brevik

Trondheim, 24.06.2021

Thesis Assignment

NTNU Trondheim
Norwegian University of Science and Technology
Department of Marine Technology – Group of Marine Structures

PROJECT THESIS IN MARINE TECHNOLOGY

SPRING 2021

FOR

STUD.TECHN. Vebjørn Brevik

Elasticity, Wave Load Modelling and Upscaling of Spar Floating Wind Turbine
Elastisitet, bølgelast modellering og oppskalering av flytende vindturbiner med spar fundament

Background:
The offshore wind industry is moving toward deeper water, farther from land, where floating wind turbines (FWTs) become more economical than bottom-fixed turbines. The costs of FWTs still far exceed their bottom-fixed counterparts, and researchers are actively searching for opportunities for cost reduction. Increasing the turbine size and reducing the steel weight of the substructure are seen as possible methods to bring costs down. These trends will then tend to result in a more elastic floating wind turbine substructure, which requires new modelling approaches in order to include both elasticity and hydrodynamic loads.

Assignment:
The following tasks should be addressed in the project work:

1. Literature review regarding floating offshore wind turbine dynamic modelling, focusing on methods for modelling elasticity in the hull, and on potential flow theory.

2. Build and compare the wave-induced responses of 4 SIMA models for the optimized 10 MW spar wind turbine developed by Hegseth et al. (2020): a model with rigid hull and wave loads according to potential flow theory, a model with rigid hull and wave loads according to Morison's equation, a model with flexible hull and wave loads according to Morison's equation, and a model with flexible hull and wave loads according to distributed potential flow theory.

3. Assess the impact of the substructure elasticity and the hydrodynamic load modelling on the fatigue analysis of several points along the floater and tower (considering a small subset of environmental conditions including both wind and wave loads).

4. Scale the optimized floater to support the IEA 15 MW wind turbine, and repeat the investigations to better understand the effects of substructure flexibility for a larger turbine.

5. Report and conclude on the investigation.

The work scope could be larger than anticipated. Subject to approval from the supervisor, topics may be deleted from the list above or reduced in extent.

In the project, the candidate shall present his personal contribution to the resolution of problem within the scope of the project work.

Theories and conclusions should be based on mathematical derivations and/or logic reasoning identifying the various steps in the deduction.

The candidate should utilize the existing possibilities for obtaining relevant literature.

The project report should be organized in a rational manner to give a clear exposition of results, assessments, and conclusions. The text should be brief and to the point, with a clear language. Telegraphic language should be avoided.

The project report shall contain the following elements: A text defining the scope, preface, list of contents, main body of the project report, conclusions with recommendations for further work, list of symbols and acronyms, reference and (optional) appendices. All figures, tables and equations shall be numerated.

The supervisor may require that the candidate, in an early stage of the work, present a written plan for the completion of the work. The plan should include a budget for the use of computer and laboratory resources that will be charged to the department. Overruns shall be reported to the supervisor.

The original contribution of the candidate and material taken from other sources shall be clearly defined. Work from other sources shall be properly referenced using an acknowledged referencing system.

Erin Bachynski
Supervisor

Deadline: 24.06.2021

Table of Contents

Acronyms

BEM	Blade Element Momentum
BFOWT	Bottom-fixed Offshore Wind Turbine
COG	Center of Gravity
FWT (FOWT)	Floating (Offshore) Wind Turbine
LCOE	Levelized Cost of Energy
MW	Megawatt
MWh	Megawatt-hour
NREL	National Renewable Energy Laboratory
NTNU	Norwegian University of Science and Technology
TLP	Tension Leg Platform
WT	Wind turbine

Symbols

$\boldsymbol{A_{wp}}$	Waterplane area
$\boldsymbol{A_{ij}}$	Added mass in motions i,j
B	Number of blades
B_{ij}	Damping in in motions i,j
$\boldsymbol{C_d}$	Drag coefficient
$\boldsymbol{C_l}$	Lift coefficient
$\boldsymbol{C_T}$	Thrust coefficient (sometimes C_{T1}, C_{T2})
$\boldsymbol{C_{33}}$	Hydrostatic restoring coefficient in heave
D	Diameter (rotor, spar)
$\boldsymbol{E_t}$	Total energy generated during lifetime
F	Prandtl factor
$\boldsymbol{H_s}$	Significant wave height
$\boldsymbol{T_p}$	Peak wave period
V	Velocity vector
$C_{i,j}$	Restoring stiffness in motions i,j
M	Mass
R	Outer radius of the rotor
r	Inner radius of the rotor
$\boldsymbol{T_{n,i}}$	Natural period in motion i (1 is surge, 2 is sway etc.)
$\boldsymbol{T_p}$	Peak wave period [s]
t	Year
U_w	Incoming wind speed [m/s]
W	New induced velocity vector
$\boldsymbol{W_{qs}}$	Quasi static induced velocity vector
1p	First excitation frequency of tower (constant rotational speed)
3p	Second exciation frequency of tower (rotor blade passing frequency)
$\boldsymbol{\phi}$	Angle that trailing vortices make with the rotorplane
$\boldsymbol{\tau}$ ($\boldsymbol{\tau_1}$, $\boldsymbol{\tau_2}$)	Time constants
$\boldsymbol{\omega_{n,i}}$	Natural angular frequency in motion i (1 is surge, 2 is sway etc.)

List of Figures

List of Tables

1 Introduction

1.1 Background

After being in the wind for quite some time, wind energy is looking to become one of the giants within clean energy solutions. Following the public's demand for more renewable energy, well-established energy companies such as Equinor and Aker are starting to make serious investments related to wind the industry [26]. Land-based and bottom-fixed offshore wind turbines (BFOWTs) are well-established concepts [6]. But challenges regarding noise, visual impact and wildlife interference have made these (especially land-based) concepts less popular. Additionally, the BFOWTs become less profitable as the water gets deeper [9]. As a response, the offshore wind industry is moving toward deeper water, where floating wind turbines (FWTs) are more economical than BFOWTs. However, the costs of FWTs are currently much higher than BFOWTs, and reducing the costs is viewed as an important enabler for floating wind.

The offshore wind industry is looking for methods to cut costs. One possibility is to build bigger turbines since using larger turbines offers cost savings within other segments of a wind farm project [29]. As a result, larger substructures are needed to support the wind turbines. Increasing the size of the turbine and floater will change the dynamics of the system. Optimizing the substructure to reduce the weight is another option, which will reduce the stiffness. A combination of these methods results in larger turbines on top of optimized foundations and will result in more elastic substructures. In order to include both elasticity and hydrodynamic loads in a global analysis, new modeling procedures are required.

In 2016, Svendsen [33] modelled a flexible tension leg platform (TLP). The first-order radiation and diffraction pressures were computed for each section of a panel model using WAMIT and then added to each section of the flexible model (using SIMO-bodies). The software used by Svendsen has been upgraded since then, including a new feature that allows the user to add hydrodynamic loads into the cross-sections without the use of SIMO-bodies. Therefore, an approach similar to the work of Svendsen was used for a spar and tower (Hegseth et al. [17]) that supports the 10 MW DTU reference turbine [4]. In order to study the effect upscaling has on the results, an upscaled version supporting the IEA 15 MW WT [1] was created. The tower used for the 15 MW FWT is based on the same tower used for the UMaine VolturnUS-S reference platform, which is a semi-submersible made to support the IEA 15 MW WT [15].

Aero-hydro-servo-elastic analysis was used to study the FWTs. The aerodynamics are given from blade element momentum (BEM) theory. Hydrodynamic loads are represented by linear potential wave theory and Morison's equation (ME), used for separate models to compare the wave load modeling methods. The flexible models are based on beam theory to model elastic behavior. Rigid models based on rigid body dynamics were made for comparison reasons. A control system was used to regulate the behavior of the wind turbines, i.e. pitch control of the blades. The catenary mooring line configuration consists of three lines spread symmetrically with respect to the vertical axis.

1.2 Procedure

The 10 MW spar from Hegseth et al. [17] was used in this thesis. An upscaled version was made to support a 15 MW turbine, and the upscaling procedure is described in Section 3.7. The models were created using various software (explained in Section 4.7). Wave excitations, added mass and damping were extracted from the models to compare hydrodynamic properties.

Constant wind tests were carried out to verify that the turbines behaved as expected. Mean values for rotor speed, thrust, torque, power, blade pitch and platform motions were examined. Decay tests were performed to determine the natural periods and damping coefficients. The tower base natural bending period in pitch was found and compared to the constant rotational speed (1p) and rotor blade passing (3p) frequencies.

Regular waves tests were used to create response amplitude operators (RAOs) for surge, heave, pitch, bending moment and stress. The models were tested for fifteen sea conditions in irregular waves with turbulent winds. Fatigue damage on the towers and spars was calculated according to DNV-RP-C205 [8], and damage equivalent loads (DELs) were determined for comparison. Spectral analysis was used to investigate the different sea conditions.

1.3 Aim

The aim of this project is to investigate how modeling the elasticity in the hull affects the spar's performance compared to rigid hulls. Wave loads are modeled according to linear potential flow theory and Morison's equation to explore differences between the methods. In order to study the effects of substructure flexibility for larger turbines, both a 10 MW spar and an upscaled 15 MW spar are evaluated.

The tasks assigned to this project are:

1. Conduct a literature review regarding FWT dynamic modeling, focusing on methods for modeling elasticity in the hull, and on potential flow theory
2. Build and compare the wave-induced responses of 4 SIMA models for the optimized 10 MW spar wind turbine developed by Hegseth et al. [17]:
    - a model with rigid hull and wave loads according to potential flow theory
    - a model with rigid hull and wave loads according to Morison's equation
    - a model with flexible hull and wave loads according to Morison's equation
    - a model with flexible hull and wave loads according to distributed potential flow theory
3. Assess the impact of the substructure elasticity and the hydrodynamic load modeling on the fatigue analysis of several points along the floater and tower (considering a small subset of environmental conditions including both wind and wave loads).
4. Scale the optimized floater to support the IEA 15 MW wind turbine [1], and repeat the investigations to better understand the effects of substructure flexibility for a larger turbine.
5. Report and conclude on the investigation.

2 Literature Review

The wind industry is rapidly changing with new technology and solutions emerging. As a consequence, new challenges arise. It is important to stay updated and be aware of the current trends. The literature review is conducted to gain knowledge and understanding of similar topics studied in the past. In Section 2.1, previous work on dynamic modeling of FWTs, elasticity in hulls and PFT is explored. Section 2.2 investigates spar-type foundations, and introduces the model optimized by Hegseth et al. [17] which is used in this project. Finally, a dive into upscaling of FWTs in Section 2.3.

2.1 Dynamic Modeling of Floating Wind Turbines

In 2016, Svendsen [33] performed a dynamic analysis of a flexible tension leg platform (TLP) wind turbine in SIMA with focus on elasticity in the hull. Radiation and diffraction pressures from first-order potential theory were computed for each panel of the 3-D hull model by using WAMIT [23]. MATLAB was used to integrate the panel pressures to generate frequency-dependent added mass, damping and excitation input for each hull section. The results were compared to Bachynski's work from 2014 [3], where the same TLP with a rigid hull was tested with hydrodynamic loads according to first-order potential theory and quadratic damping. The comparison revealed that the natural periods increased for the flexible model, most significantly in heave (43%) and pitch (18%). Furthermore, the flexible model predicted larger motions, larger bending moments at the tower base and higher tendon tensions at the top of each tendon.

The method used by Svendsen (see flowchart from Svendsen [33] in Figure 1) to include both flexibility and hydrodynamic loads in a global analysis of a TLP revealed encouraging results. On top of that, SIMA has been upgraded since then and it would be interesting to use a similar approach. A new modeling functionality called "Potential Flow Library" is currently under development in SIMA, which allows the user to provide frequency-dependent radiation and diffraction data to cross-sections [32]. In comparison, Svendsen added hydrodynamic loads to SIMO-bodies (step 4 in flowchart, see Figure 1). Hence, only the last step of Svendsen's method is going to be changed.

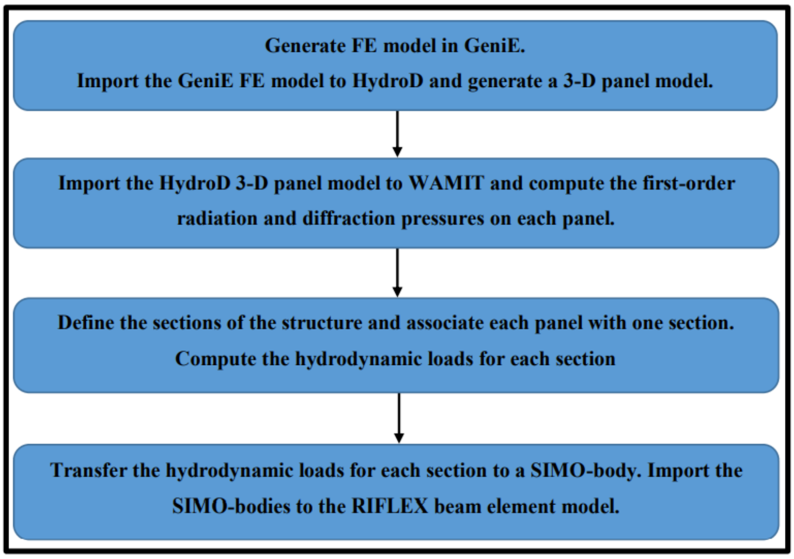

Generate FE model in GeniE.
Import the GeniE FE model to HydroD and generate a 3-D panel model.

Import the HydroD 3-D panel model to WAMIT and compute the first-order radiation and diffraction pressures on each panel.

Define the sections of the structure and associate each panel with one section.
Compute the hydrodynamic loads for each section

Transfer the hydrodynamic loads for each section to a SIMO-body. Import the SIMO-bodies to the RIFLEX beam element model.

Figure 1: Flowchart of modeling procedure from Svendsen [33]

2.2 Spar

Hegseth et al. [17] developed an optimized 10 MW FWT design using integrated design optimization of the spar, tower, mooring system and blade-pitch controller. To find optimal design solutions, gradient-based optimization with fatigue and extreme response constraints and an objective function based on system cost and power quality was used. The optimized spar has an interesting shape (resembles an hourglass), which differ from a classical, constant diameter spar. A small diameter in the wave zone limit the wave loads on the spar, and the large diameter at the bottom increases added mass in heave. Based on the promising results, the optimized design from Hegseth et al. is used in this project. The properties of the spar and tower is given in Section 4.1. An illustration of the design is given in Section 4.7.2.

2.3 Upscaling

Increasing the turbine size is considered a possible method to reduce costs since larger turbines offer greater savings within other segments, such as foundations [29]. Equinor installed a 2.3 MW WT in 2009 (Hywind Demo [11]), five 6 MW WTs in 2017 (Hywind Scotland [12]) and are planning to install eleven 8 MW WTs in 2022 (Hywind Tampen [13]). Equinor experienced a cost reduction in capital expenditures (CAPEX) of 70% in euros per megawatt-hour from the Hywind Demo to Hywind Scotland, and expects an additional 40% decrease between Hywind Scotland and Hywind Tampen [10] (see illustration from Equinor in Figure 2).

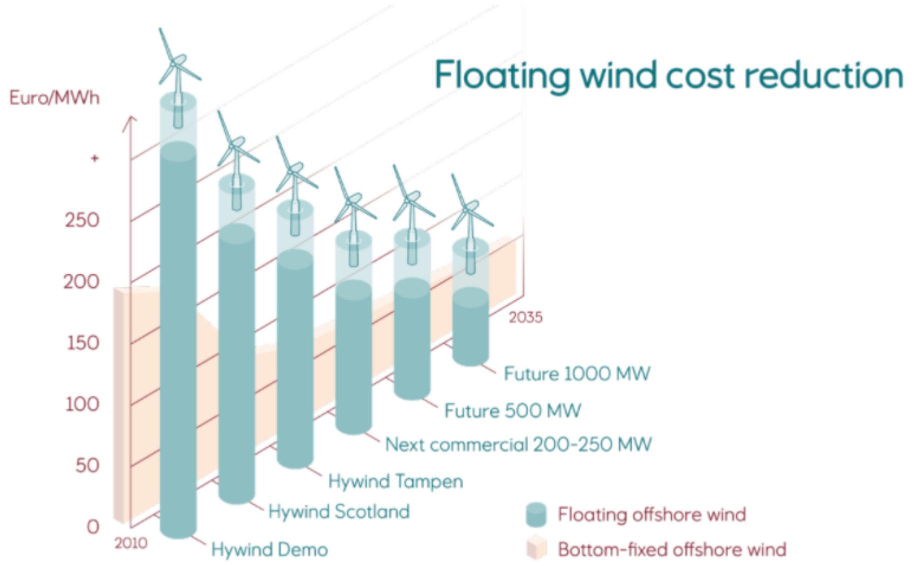

Figure 2: Floating wind cost reduction estimates, taken from Equinor [10]

In March 2020, the International Energy Agency (IEA) published a technical report defining a 15 MW offshore reference WT, which was developed in a collaboration between the National Renewable Energy Laboratory (NREL), the Technical University of Denmark (DTU) and the University of Maine [1]. The report documents the design, performance and properties of the 15 MW WT, and it is possible to use their WT for an upscaled 15 MW version of the spar presented by Hegseth et al. [17]. However, a monopile is used in

IEA's report. The tower is therefore designed for a monopile and is most likely not suited for a FWT.

In July 2020, another technical report issued by IEA [15] presented an FWT semi-submersible design that supports the same 15 MW WT described in the report from March 2020 [1]. A tower experience increased inertial and gravity loads due to the platform motions for an FWT. Thus it has higher stiffness requirements than a tower made for a BFOWT. Consequently, the cross-sections have larger thicknesses and the tower weighs 46.5% more than the tower made for the monopile. Also, the FWT tower has a higher natural frequency (0.5 Hz, compared to 0.18 Hz for the BFOWT tower) and is in the stiff-stiff region. Placing the tower on a floating platform makes it unfeasible to resist the loads while remaining in the soft-stiff region. Since the tower is specifically designed for an FWT and the properties are accessible, it was used for the upscaled 15 MW spar design.

The spar needs to be upscaled in order to support the 15 MW turbine and tower. In 2016, Leimeister et al. [24] upscaled a 5 MW semi-submersible FWT to support a 7.5 MW WT. A geometrical scaling factor based on the power rating ratio squared was used since the power is proportional to the rotor diameter squared. However, they soundly state that simple geometrical upscaling is inadequate for FWT systems due to their complex nature. Consequently, they made a number of considerations in order to maintain similar hydrodynamic behavior of the floating system. Based on their work, the importance of making rational design requirements based on the model at hand when upscaling is illustrated. As a result, several assumptions were made when upscaling the spar (presented in Section 3.7).

3 Theoretical Background

The analyses of FWTs in SIMA are aero-hydro-servo-elastic, which means that several disciplines need to be considered. First, BEM theory is presented to explain the aerodynamics of a wind turbine (Section 3.1). In Section 3.2, hydrodynamics are introduced, involving linear potential flow theory, Morison's equation and strip theory. Rigid body dynamics, beam formulation and decay tests are presented in Section 3.3. A brief introduction to the control system of wind turbines is given in Section 3.4.

In Section 3.5, the theory for RAOs is given. Since mooring lines are used in this project, some background is provided in Section 3.6. The upscaling procedure is described in Section 3.7. Also, a fatigue study was conducted for various sea conditions in the report. Consequently, fatigue damage and damage equivalent loads are introduced in Section 3.8.

3.1 Aerodynamics

The aerodynamic background is shown here. First, the BEM theory is presented, followed by some important correction factors to this theory. All the information provided in this section is based on the RIFLEX theory [31].

3.1.1 BEM theory

The aerodynamics of a wind turbine can be modeled by blade element momentum (BEM) theory. In BEM theory, the thrust and torque are established from an annular ring based on momentum theory. If an incoming wind speed along an airfoil section is imagined, the lift and drag forces can be established. Now, the force normal to the rotor plane and tangential to the rotor plane is given, along with the flow angle which is the sum of the angle of attack and blade pitch angle.

From the normal and tangential forces, the solidity ratio, normal and tangential forces is derived. The normal and tangential forces are functions of the lift and drag coefficients. Now, an iteration process is needed. The normal and tangential induction factors need to be guessed, then the flow angle can be calculated. This gives the angle of attack and the lift and drag coefficients. Then, the induction factors are updated using the relation mentioned earlier. If the solution has converged, the process is finished. If not, the flow angle has to be calculated again using the updated induction factors, and the other steps needs to be repeated as well.

3.1.2 Corrections

BEM theory is not valid for induction factors greater than 0.4. The Glauert correction is used for induction factors larger than 0.4, and the empirical thrust curve by Burton et al. (2011) is used:

$$a = \frac{(C_T/F - C_{T1})}{C_{T2} - C_{T1}}(a_2 - a_1) + a_1 \tag{1}$$

where $a_2 = 1.0$, $C_{T2} = 1.82$, $a_1 = 1.0 - 0.5\sqrt{C_{T2}}$, $C_{T1} = 4a_1(1 - a_1)$, and F is the Prandtl factor, given in Equation 2. The Prandtl correction factor accounts for the tip and hub loss on a blade due to a finite number of blades, and is given as a function of the radial location r:

$$F = \frac{2}{\pi} \cos^{-1}(e^{-f}) \tag{2}$$

where

$$f = \frac{B}{2} \frac{(R - r)}{2r \sin \phi} \tag{3}$$

Here, B is the number of blades, R is the outer radius of the rotor, and ϕ is the angle that the trailing vortices make with the rotor plane. ϕ is assumed to be the same as the angle of incoming flow, neglecting tangential induced velocity.

In BEM theory, the induction factor a is updated immediately if incoming wind velocity, blade pitch angle or rotor speed change. In reality, the larger flow field takes time to react to such changes. The time scale of the reaction can be on the order of D/U, where D is the rotor diameter and U is the incoming wind speed. Dynamic wake correction is used to account for this effect, where the Stig Øye dynamic inflow model can be utilized. It will act as a filter for the induced velocities, see Equation 4 and 5:

$$W + \tau_2 \frac{dW}{dt} = W_{int} \tag{4}$$

$$W_{int} + \tau_1 \frac{dW_{int}}{dt} = W_{qs} + 0.6\tau_1 \frac{dW_{qs}}{dt} \tag{5}$$

where W_{qs} is the quasi-static induced velocity vector, W is the new induced velocity vector, τ_1 and τ_2 are time constants. C_l and C_d is given as static input, but when a blade sees dynamic incoming wind, there may be sudden attachment and re-attachment of flow. Then C_l and C_d do not follow static values. This can lead to very large transient loads. The dynamic stall correction is used (models need to be used, i.e. Øye).

3.2 Hydrodynamics

The hydrodynamics aspects of this thesis are explained in this section. The linear potential flow theory is presented in Section 3.2.1, followed by restoring forces and moments in Section 3.2.2. An introduction to Morison's equation and strip theory is given in Section 3.2.3, and the drag and mass coefficients used for Morison's equation are established in Section 3.2.4.

3.2.1 Linear Potential Flow Theory

Linear potential flow theory is used to evaluate the sea motions and loads acting on a structure, and the following description is based on Faltinsen [14]. The velocity potential ϕ is used to formulate the velocity vector $\mathbf{V}$ at the time t and point $\mathbf{x} = (x,y,z)$ in a Cartesian coordinate system fixed in space,

$$\mathbf{V} = \nabla\phi \equiv \mathbf{i}\frac{\partial\phi}{\partial x} + \mathbf{j}\frac{\partial\phi}{\partial y} + \mathbf{k}\frac{\partial\phi}{\partial z} \tag{6}$$

where $\mathbf{i}$, $\mathbf{j}$ and $\mathbf{k}$ are unit vectors along the x-, y- and z-axes, respectively, and ∇ is the gradient defined as

$$\nabla = \left(\frac{\partial}{\partial x}, \frac{\partial}{\partial y}, \frac{\partial}{\partial z}\right) \tag{7}$$

The fluid is assumed to be incompressible and inviscid, and the fluid motion is considered to be irrotational:

$$\nabla \cdot \mathbf{V} = 0 \tag{8}$$

$$\nabla \times \mathbf{V} = 0 \tag{9}$$

Following the assumption that the fluid is incompressible, the velocity potential has to satisfy the Laplace equation,

$$\frac{\partial^2\phi}{\partial x^2} + \frac{\partial^2\phi}{\partial y^2} + \frac{\partial^2\phi}{\partial z^2} = 0 \tag{10}$$

and the corresponding boundary conditions. The first boundary condition is the kinematic body boundary condition, which for a body moving with velocity $\mathbf{U}$ can be written as

$$\frac{\partial\phi}{\partial n} = \mathbf{U} \cdot \mathbf{n} \tag{11}$$

where $\frac{\partial}{\partial n}$ denotes differentiation along the normal to the body surface. Equation 11 states that no fluid enters or leaves the body surface. The non-linear free-surface conditions assume that a fluid particle on the free surface stays on the free surface. This is inconvenient since the free surface is unknown before solving the problem. Linearizing the free-surface conditions simplifies the problem. For linear theory, the velocity potential is proportional to the wave amplitude ($\phi \propto \zeta_a$), and is valid if the wave amplitude is relatively small compared to the wavelength and body dimension (i.e. diameter of cylinder). According to Faltinsen [14], Taylor expansion can be used to transfer the free-surface conditions from the free-surface position ($z = \zeta(x, y, t)$) to the mean free-surface at $z = 0$. If the linear terms in the wave amplitude are kept, the non-linear free-surface conditions (see Faltinsen [14]) can be linearized into

$$\frac{\partial \zeta}{\partial t} - \frac{\partial \phi}{\partial z} = 0 \tag{12}$$

$$g\zeta + \frac{\partial \phi}{\partial t} = 0 \tag{13}$$

for $z = 0$. Equation 12 is the kinematic free-surface boundary condition, and Equation 13 is the dynamic free-surface boundary condition. The later states that the fluid pressure (p) at the free-surface is equal to the atmospheric pressure (p_0). The free-surface elevation ζ can be found from Equation 13 if the velocity potential is known. Combining Equation 12 and 13 yields

$$\frac{\partial^2 \phi}{\partial t^2} + g\frac{\partial \phi}{\partial z} = 0 \tag{14}$$

for $z = 0$. Assuming a horizontal seabed and a free surface of infinite horizontal extent, linear wave theory for propagating waves can be derived. The seabed boundary condition can be found by using Equation 14 together with the Laplace equation (Equation 10):

$$\frac{\partial \phi}{\partial z} = 0 \tag{15}$$

for z = -h, where h is the water depth. Linear wave theory for propagating waves can now be derived. Following the discussion above, the hydrodynamic loads in regular waves will now be presented. Assuming a structure in incident, regular sinusoidal waves of small wave steepness and steady-state condition, the hydrodynamic problem can be split into two - the diffraction and the radiation problem [14].

The diffraction problem involves the hydrodynamics loads on a structure restrained from oscillating with incident regular waves acting. These loads consist of the Froude-Krylov and diffraction forces and moments, and are referred to as the wave excitation loads. The radiation problem considers the forces and moments on a structure forced to oscillate with the wave excitation frequency while no incident waves are acting. These loads consist of added mass, damping, and restoring forces and moments. Assuming linearity (as discussed earlier), the loads mentioned for the diffraction and radiation problems can be added in order to give the total hydrodynamic forces [14].

3.2.2 Restoring Forces and Moments

According to Faltinsen [14], the restoring forces of a freely floating body will stem from hydrostatic and mass considerations. If the submerged volume of the body is symmetric to the x-z plane, the only non-zero coefficients will be

$$C_{33} = \rho g A_{wp} \tag{16}$$

$$C_{35} = C_{53} = -\rho g \iint_{A_{wp}} (x) ds \tag{17}$$

$$C_{44} = \rho g V (z_B - z_G) + \rho g \iint_{A_{wp}} (y^2) ds = \rho g V \overline{GM}_T \tag{18}$$

$$C_{55} = \rho g V (z_B - z_G) + \rho g \iint_{A_{wp}} (x^2) ds = \rho g V \overline{GM}_L \tag{19}$$

where A_{wp} is the waterplane area, V is the displaced volume of water, z_G and z_B are the center of gravity and buoyancy, respectively. $\overline{GM}_T$ and $\overline{GM}_L$ are the transverse and longitudinal metacentric heights, respectively. If the body mass (M) is not equal to the buoyancy (ρV), Equation 18 and 19 are not valid. C_{44} and C_{55} can then be expressed as:

$$C_{44} = \rho g V z_B - M g z_G + \rho g I_{wp,y} \tag{20}$$

$$C_{55} = \rho g V z_B - M g z_G + \rho g I_{wp,x} \tag{21}$$

where $I_{wp,y}$ and $I_{wp,x}$ are the moments of inertia about the y- and x-axis, respectively. For a symmetric spar, $I_{wp,y} = I_{wp,x}$ (hence, $C_{44} = C_{55}$).

For a moored structure, relevant restoring forces should be added (for example in surge, sway and yaw). An example of a restoring force matrix for a moored spar is

$$C = \begin{bmatrix} C_{11} & 0 & 0 & 0 & C_{15} & 0 \\ 0 & C_{22} & 0 & C_{24} & 0 & 0 \\ 0 & 0 & C_{33} & 0 & 0 & 0 \\ 0 & C_{42} & 0 & C_{44} & 0 & 0 \\ C_{51} & 0 & 0 & 0 & C_{55} & 0 \\ 0 & 0 & 0 & 0 & 0 & C_{66} \end{bmatrix} \tag{22}$$

where the coupled surge-pitch (C_{15}, C_{51}) and sway-roll (C_{24}, C_{42}) coefficients are related to the fairlead location (z_f) and stiffness in surge and sway, respectively.

3.2.3 Morison's Equation

Morison's equation (ME) is often used to calculate wave loads on circular, slender structures. ME is a long-wave approximation, which means that the diameter of the structure (D) should be small compared to wavelength (λ). ME is considered valid for $\lambda/D \geq 5$. If the wavelength is not large compared to the diameter, diffraction effects should be considered. Strip theory is applied, which assumes an elongated, slender structure and small wavelength. The ME calculates the horizontal force on a strip with length dz of a vertical rigid circular cylinder [14]:

$$dF = \rho \frac{\pi D^2}{4} dz C_m a_1 + \frac{\rho}{2} C_D D dz |u| u \tag{23}$$

where ρ is the density of water, D is the cylinder diameter, C_m and C_d are the mass and drag coefficients, respectively. The excitation forces in surge and pitch when using ME can be estimated as:

$$dF_{1,ME,i} = (C_m \rho \frac{\pi D_i^2}{4} \dot{u}) dz_i = (C_m \rho \frac{\pi D_i^2}{4} \omega^2 \zeta_a e^{\frac{\omega^2}{g} z_i}) dz_i \tag{24}$$

$$dF_{5,ME,i} = (dF_{1,ME,i}) z_i \tag{25}$$

where z_i is the vertical distance from MSL to the center of the strip. ME does not give estimates for heave excitation. Instead, it is possible to estimate it by adding the Froude-Krylov force (F_{FK}) by the product of added mass in heave (A_{33}) and g, and then dividing with the draft (d),

$$dF_{3,ME,i} = \frac{F_{FK} + A_{33} g}{d} = \frac{\rho g \zeta_a e^{\frac{\omega^2}{g} z_i} + A_{33} g}{d} \tag{26}$$

where added mass in heave for example can be estimated according to Lamb [20],

$$A_{33} = \frac{1}{3} \rho D^3 \tag{27}$$

The added mass in surge, sway-roll, surge-pitch and pitch can be estimated with Morison's equation by using strip theory:

$$dA_{11,ME,i} = \left(\rho C_a \frac{\pi D_i^2}{4} \right) dz_i \tag{28}$$

$$dA_{24,ME,i} = \left(\rho \frac{\pi D_i^2}{4} BG_z \right) dz_i \tag{29}$$

$$dA_{15,ME,i} = - \left(\rho \frac{\pi D_i^2}{4} BG_z \right) dz_i \tag{30}$$

$$dA_{55,ME,i} = (dA_{11,ME,i}) z_i^2 \tag{31}$$

where BG_z is the vertical distance between the center of buoyancy (COB) and center of gravity (COG). Due to the symmetry of the spar, sway and roll are identical to surge and pitch, respectively. The coupled motions are also the same, except that the sway-roll couplings are positive and the surge-pitch couplings are negative.

3.2.4 Drag and Mass Coefficients

The drag (C_d) and mass (C_m) coefficients used in ME (Section 3.2.3) must be estimated empirically [14]. According to DNV-RP-C205 [7], C_d and C_m are dependent on the Reynolds number (Re), Keulegan-Carpenter (KC) number and non-dimensional roughness. However, since Re and KC depend on velocity and wave period (only KC) they will change during simulations. To account for this is considered to be unpractical in relation to what one would gain, since it would not contribute to the comparison of the models. Constant values for Cd and Cm are used instead. The same values are used for all models.

The drag coefficient is determined from Figure 6-6 in DNV-RP-C205 [7], using a roughness of 10^{-4} and assuming to be in the post-critical flow regime. Thus, $C_d = 0.8$. The mass coefficient is given by $C_m = 1 + C_a$, where C_a is the added mass coefficient. KC decreases with water depth, and therefore low KC values are expected for most of the spar. For low KC (< 3), C_a can be assumed independent of KC and set to 1. Thus, $C_a = 1$ and $C_m = 2$.

3.3 Structural Dynamics

In this section, rigid body dynamics is introduced first in Section 3.3.1. The beam theory is presented to describe how elasticity is represented for the elastic models (Section 3.3.2). In Section 3.3.3, the theory for decay tests is shown, which is used to establish natural periods and damping coefficients.

3.3.1 Rigid Body Dynamics

The equation of motion for a 6-DOF rigid body is given by

$$(M + A)\ddot{\eta} + B\dot{\eta} + C\eta = F(\omega) \tag{32}$$

where M is the mass matrix, A is the added mass matrix, B is the damping matrix, C is the stiffness matrix, F is the excitation matrix and ω is the angular wave frequency [21].

The following is relevant for the spectral analysis. When solving the equation of motion in the frequency domain, the excitation can be written as an infinite sum of harmonic components (which can be expressed mathematically by Fourier-transformation). The response is transformed into the frequency domain. Due to the angular frequency dependency, solving Equation 32 expresses the structure's sensitivity to the load frequency. This approach is suited for analyses of response to stochastic loads (i.e. waves). Additionally, it is useful for structures with frequency-dependent M, A, B and C [21].

3.3.2 Beam Formulation and Euler-Bernoulli

Beam formulation is presented here. This is important for relating the deformation, moment, shear force and curvature of the beam to the material properties. The RIFLEX formulation for beam elements is related to the Euler-Bernoulli beam theory, but with some modifications to make it applicable for large displacements [31]. This is more relevant for the blades. The elasticity of the spar and tower is of interest in this report, which should not experience large displacements. Therefore, the Euler-Bernoulli beam theory is presented below based on Haukaas [16].

The Euler-Bernoulli beam theory assumes that the material is linear elastic (Hooke's law) and that plane sections remain plane and perpendicular to the neutral axis. Equilibrium equations are established by assuming equilibrium in x-direction for an infinitesimal beam element:

$$q(x) = -\frac{dV}{dx} \tag{33}$$

w is the vertical load at a point x along the beam. Moment equilibrium yields the following expression for shear force (V):

$$V(x) = \frac{dM}{dx} \tag{34}$$

M is the moment. Considering an infinitesimal beam element undergoing bending and a small angle between the z-axis and the local coordinate system of the beam element, the curvature of the beam (κ) can be approximated as

$$\kappa = \frac{\mathrm{d}^2\mathrm{v}}{\mathrm{d}x^2} \tag{35}$$

where v is the transverse displacement and $\frac{\mathrm{d}^2\mathrm{v}}{\mathrm{d}x^2}$ is the change in transverse displacement per unit length. The curvature can also be expressed as:

$$\kappa = \frac{M}{EI} \tag{36}$$

where E is the modulus of elasticity and I is the moment of inertia. By setting Equation 35 equal to Equation 36, the following expression is obtained:

$$\frac{\mathrm{d}^2\mathrm{v}}{\mathrm{d}x^2} = \frac{M}{EI} \tag{37}$$

Combining the equilibrium equations from earlier, Equation 33 and Equation 34, yields:

$$q(x) = -\frac{\mathrm{d}^2 M}{\mathrm{d}x^2} \tag{38}$$

Inserting Equation 38 into Equation 37 leads to the Euler-Bernoulli equation:

$$-q(x) = \frac{\mathrm{d}^2}{\mathrm{d}x^2}(EI\frac{\mathrm{d}^2 v}{\mathrm{d}x^2}) \tag{39}$$

Derivating Equation 39 yields the following equations for M and V:

$$M = -EI\frac{\mathrm{d}^2 v}{\mathrm{d}x^2} \tag{40}$$

$$V = -\frac{\mathrm{d}}{\mathrm{d}x}(EI\frac{\mathrm{d}^2 v}{\mathrm{d}x^2}) \tag{41}$$

The bending stress (σ) can be calculated if the displacement due to the load has been determined. For pure bending, it can be given as:

$$\sigma = \frac{Mz}{I} = -zE\frac{\mathrm{d}^2 v}{\mathrm{d}x^2} \tag{42}$$

where z is the distance from the neutral axis to the point of interest.

3.3.3 Decay tests

Free decay tests can be used to establish the natural period (T_n), linear (b_1) and quadratic (b_2) damping coefficents. The tests are performed by initially applying an excitation force on the system and then study how the system oscillates when undisturbed. The logarithmic decrement method [22] is used to determine the natural period, assuming that the amplitudes follow a logarithmic decrement according to

$$\Lambda = \frac{1}{n}\ln\frac{x_0}{x_n} \tag{43}$$

where Λ is the logarithmic decrement, x_0 is the initial amplitude and x_n is the amplitude n peaks from x_0. The logarithmic decrement is connected to the damping ratio as

$$\Lambda = 2\pi\xi\frac{\omega_n}{\omega_d} \tag{44}$$

Here ω_n is the natural angular frequency, and ω_d is the damped natural frequency given mathematically as

$$\omega_d = \omega_n\sqrt{1-\xi^2} \tag{45}$$

where ξ is the damping ratio. Since ξ usually is a small number [22], the following approximation is made:

$$\frac{\omega_n}{\omega_d} \approx 1 \tag{46}$$

Using Equation 46 in Equation 44 leads to the following expression:

$$\Lambda = 2\pi\xi \tag{47}$$

Rearranging Equation 47 and inserting Equation 43 yields

$$\xi \simeq \frac{1}{2\pi n} \ln \frac{x_0}{x_n} \tag{48}$$

The damped natural frequency is found from the period of oscillation from the decay tests, and the natural angular frequency can be determined by rearranging Equation 45:

$$\omega_n = \frac{\omega_d}{\sqrt{1-\xi^2}} \tag{49}$$

Now the natural period and natural frequency (f_n) can be determined by

$$T_n = \frac{2\pi}{\omega_n} \tag{50}$$

$$f_n = \frac{1}{T_n} \tag{51}$$

In addition, the results from the free decay tests can be used to establish the linear (b_1) and quadratic (b_2) damping coefficients. In this report, they were determined by using an approach developed by Hoff [18]. This involves linearization of the coefficients, which changes the units. The unit of b_1 is rad/s, and the unit of b_2 is 1/m for motions and 1/deg for rotations. They serve only as a comparison between the models. For more details regarding the approach, reference is made to the technical report from 2001 made by Hoff [18] and Bachynski's doctoral thesis from 2014 [3].

3.4 Control System of Wind Turbines

A short introduction to control systems of wind turbines is given in this section. Parameters such as rated power, minimum and rated rotor speed, minimum and maximum pitch angle can be set in the control system. Pitch control is a power control technique that pitches the turbine blades out of the wind when the power level goes above a prescribed safe limit. If the power level gets lower, the blades are pitched into the wind at an optimal angle of attack to maintain rated power. This ensures minimal power loss and results in the captured power being equal to the electrical power produced by the wind generator [2].

3.5 Response Amplitude Operator

Response amplitude operators (RAOs) can be used to describe how motions (i.e. surge, η_1) or loads (i.e. bending moment, M_b) will act for different wave angular frequencies (ω).

If regular waves are only acting in one direction with the same wave amplitude (ζ_a), RAOs can be expressed independently of direction as

$$RAO(\omega) = \frac{|x_0(\omega)|}{|\zeta_a|} \tag{52}$$

where x_0 is the response amplitude of an arbitrary response (i.e. η_1 or M_b). The unit of the RAO depends on the response. For motions (in meters) the unit will be [m/m], while for bending moment (in Nm) the unit is [Nm/m] [22].

3.6 Mooring

The cross-sectional area (A_{moor}) and mass per unit length (m_{moor}) of the mooring lines is to be determined. In order to determine m_{moor}, the weight in water ($w_{s,moor}$) is needed. The following equations, suggested by Barltrop [5], are used:

$$w_{s,moor} = 0.1875 D_{moor}^2 \tag{53}$$

$$EA_{moor} = 90000 D_{moor}^2 \tag{54}$$

D_{moor} (given in mm) and EA_{moor} are the diameter and axial stiffness of the mooring lines, respectively. The submerged weight of a mooring line in equilibrium can be formulated as:

$$w_{s,moor} = m_{moor} g - \rho g A_{moor} \tag{55}$$

Rearranging Equation 55 yields

$$m_{moor} = \frac{w_{s,moor} + \rho g A_{moor}}{g} \tag{56}$$

and the cross-sectional area for a cylindrical mooring line can be given as

$$A_{moor} = \frac{\pi}{4} D_{moor}^2 \tag{57}$$

3.7 Upscaling Procedure

The upscaling procedure for the 15 MW spar is described here. According to Leimeister et al. [24], simple geometrical scaling based on turbine rating is insufficient for an FWT. In order to maintain stability and flotation abilities of a support structure (i.e. spar), considerations based on the structure at hand needs to be made. In this case, the nacelle-rotor assembly (NRA) and tower are already determined for the 15 MW turbine. It is only the spar that needs to be scaled. The turbine needs to be considered during the upscaling procedure. The spar is going to be scaled based on the following steps and requirements:

1. Determine scaling factor based on the cube root of the turbine-mass ratio between the 10 and 15 MW turbines.
2. Determine the desired spar mass (including ballast) based on 10 MW spar and scaling factor.
3. Determine the desired displaced volume based on the known weight of the tower, NRA and upscaled spar.
4. The top diameter of the spar has to be downscaled to 10 m to fit the bottom of the 15 MW tower.
5. Minimize increase in draft by using larger scaling factor for some of the diameters.
6. Achieve desired displaced volume and draft.
7. Achieve approximately the same mean pitch angle as for the 10 MW turbine.
8. Minimize the amount of steel weight for the spar, while still fulfilling the requirements.

The scaling factor (s) is determined by calculating the cube root of the NRA (M_{NRA}) and tower (M_{tower}) mass ratio between the 10 and 15 MW turbines [19]:

$$s = \sqrt[3]{\frac{M_{NRA,15MW} + M_{tower,15MW}}{M_{NRA,10MW} + M_{tower,10MW}}} \tag{58}$$

An alternative approach is to take the square root of the power rating (P_{rated}) ratio between the turbines, as suggested by Leimeister et al. [24]:

$$s_2 = \sqrt{\frac{P_{rated,15MW}}{P_{rated,10MW}}} \tag{59}$$

The former scaling factor ($s = 1.098$) is used in this report. The mass of the 15 MW spar including ballast ($M_{spar,15MW}$) should then be equal to the mass of the 10 MW spar including ballast ($M_{spar,10MW}$) times s to the power of three:

$$M_{spar,15MW} = (M_{spar,10MW})s^3 \tag{60}$$

The same should apply for the displaced volume of the 15 MW spar (∇_{15MW}),

$$\nabla_{15MW} = (\nabla_{10MW})s^3 \tag{61}$$

where ∇_{10MW} is the displaced volume of the 10 MW spar. This needs to be checked by dividing the mass of the entire FWT by ρ,

$$\nabla_{15MW} = \frac{M_{NRA,15MW} + M_{tower,15MW} + M_{spar,15MW}}{\rho} \tag{62}$$

After establishing the desired $M_{spar,15MW}$ and ∇_{15MW}, the scaling of the spar geometry is carried out. First of all, the length of all the spar sections is simply scaled with s. This results in the length of the spar also being increased by s, but since the top of the 15 MW spar is located at 15 m above SWL (compared to 10 m for the 10 MW spar) the draft (d) is increased by a lower factor, $s_d = 1.048$ (see resulting vertical position of cross-sections in Table 1). This is beneficial with regard to installation.

The diameters and wall thicknesses of the spar sections are then scaled while ensuring that the desired $M_{spar,15MW}$, ∇_{15MW} and d is fulfilled. At the same time, it is desirable to limit the amount of steel (M_{steel}), not change C_{33} too much compared to the 10 MW spar, and have the largest BG and C_{55} as possible. C_{33} and C_{55} are calculated based on Equation 16 and 21 in Section 3.2.2, respectively. In addition, it is preferable to achieve a mean pitch angle similar to the 10 MW spar. The 1 DOF and 2 DOF tests presented in Section 3.7.1 and 3.7.2, respectively, are used to check this. The scaling factors used for diameters and thicknesses are given in Table 1.

Elevation wrt. SWL [m]	**s, diameters**	**s, thicknesses**
-84.313	1.2	1.2
-78.423	1.15	1.15
-70.793	1.098	1.098
-64.349	1.098	1.098
-57.751	1.098	1.098
-51.640	1.098	1.098
-44.649	1.098	1.098
-30.670	1.15	1.15
-16.662	1.098	1.098
-5.583	1	1
5	1	1
15	0.79	1.36

Table 1: Scaling factors (s) used for cross-sections of upscaled spar

3.7.1 1 DOF Test

The 1 DOF test assumes that the FWT only has one degree of freedom, which is in pitch. The maximum thrust (T_{max}) from constant wind tests is used. The thrust is acting at the hub height, h_{hub}. The restoring moment in pitch (C_{55}) is the only other load present. The pitch bending moment (M_b) is given as:

$$M_b = T_{max} h_{hub} \tag{63}$$

The mean pitch angle (θ) in degrees can then be found from static equilibrium:

$$\theta = \frac{M_b}{C_{55}} \frac{180}{\pi} \tag{64}$$

3.7.2 2 DOF Test

The 2 DOF test assumes that the FWT has two degrees of freedom, namely surge and pitch. A stiffness in surge (C_{11}) is introduced at the vertical location of the fairleads ($z_{fairlead}$). This leads to the following system of equations:

$$\begin{bmatrix} C_{11} & -C_{11} z_{fairlead} \\ -C_{11} z_{fairlead} & C_{55} + C_{11} z_{fairlead}^2 \end{bmatrix} \begin{bmatrix} x \\ \theta \end{bmatrix} = \begin{bmatrix} T_{max} \\ T_{max} h_{hub} \end{bmatrix} \tag{65}$$

Here, x is the displacement in surge. If x and θ are the only unknowns, Equation 65 is an equation set consisting of two equations and two unknowns. It is then possible to solve for x and θ.

3.8 Fatigue

3.8.1 Fatigue Damage

The fatigue damage due to axial stress is to be determined. The DNV-RP-C203 standard is used for reference [8]. The axial stress (σ) is calculated using the following equation:

$$\sigma = \frac{N_x}{A} + \frac{M_y}{I_y} r \sin\theta + \frac{M_z}{I_z} r \cos\theta \tag{66}$$

where N_x is the axial force, M_y is the moment about local y-axis, M_z is the moment about local z-axis, and (r,θ) is the location of the cross-section in polar coordinates. Since the wind and waves are aligned in x-direction, only one point needs to be considered on the outer radius and θ is set to 270°.

The time history of stress at the given point is computed in the SIMA analysis. Now, rainflow counting needs to be used to compute the number of stress cycles [27]. Afterward, an SN-curve that fits in this case needs to be chosen in order to compute the damage [8]. Now it is needed to choose the correct SN-curve, how many cycles (N) the cross-section will be subject to, material factors (m and log$\bar{a}$), stress limit ($\Delta\sigma$), slope (k) and the reference thickness (t_{ref}).

The number of cycles until failure can now be calculated based on the following equation [8]:

$$\log(N) = \log(\bar{a}) - m\log(\Delta\sigma(\frac{t}{t_{ref}})^k) \tag{67}$$

where t is the thickness of the cross-section. Then, Miner's rule [30] can be applied to find the fatigue damage (D):

$$D = \sum_{i=1}^{k} \frac{n_i}{N_i} \tag{68}$$

where n is the number of cycles of a given stress amplitude and k is the number of different amplitude levels of the cycles. Failure occurs when the damage is equal to 1.

3.8.2 Damage Equivalent Load

Based on correspondence with COWI, the following relationship is used for damage equivalent loads (DEL):

$$DEL = \left(\frac{\sum_{i=1}^{n} F_i^m N^i}{N_{ref}}\right)^{\frac{1}{m}} \tag{69}$$

where n is the no. of cycle bins, F_i and N_i is the load range and number of cycles in bin i (found from rainflow counting [27]), respectively. N_{ref} is the reference number of cycles and m is the Wöhler curve exponent. $N_{ref} = 10^7$ and $m = 4$ will be used in this report.

4 Modeling

In this chapter, the modeling part of the project is presented. First, the properties and geometry of the 10 MW spar based on Hegseth et al. [17] is introduced in Section 4.1. The upscaled 15 MW spar is presented in Section 4.2, followed by a description of the DTU 10 MW and IEA 15 MW wind turbines in Section 4.3. The tower characteristics are shown in Section 4.4, and the mooring configuration is introduced in Section 4.5. An overview of all the models is given in Section 4.6. Then, the modeling procedure involving GeniE, HydroD, WAMIT and RIFLEX is described in Section 4.7. The control system of the 10 and 15 MW wind turbines is presented in Section 4.8. The generation of wind files using TurbSim is explained in Section 4.9, and the filtering process of results is illustrated in Section 4.10.

4.1 10 MW Spar

The optimized spar design developed by Hegseth et al. [17] is used to support the 10 MW turbine in this project. The diameter and thickness vary with height, and the cross-section properties are given in Table 2. Physical parameters are given in Table 3. More background information regarding the spar design is given in Section 2.2. An illustration of the design is given in Figure 6a in Section 4.7.2.

Elevation wrt. SWL [m]	Outer diameter [m]	Wall thickness [m]
10.000	12.660	0.061
-8.741	12.784	0.085
-18.829	16.212	0.060
-31.584	20.681	0.068
-44.312	16.314	0.061
-50.677	14.070	0.054
-56.242	12.940	0.051
-62.249	15.003	0.056
-68.117	17.055	0.064
-75.064	19.505	0.075
-80.427	21.365	0.084

Table 2: 10 MW spar properties (from Hegseth et al. [17])

Parameter	Value
Length of spar [m]	90.427
Draft [m]	80.427
Displacement [m^3]	17244
Steel mass [Te]	2854
Ballast (concrete) mass [Te]	13111
Total mass [Te]	15965
Vertical COG [m]	-65.77
Vertical COB [m]	-42.91
Ixx, Iyy [$kg \cdot m^2$]	7.99E+10
Izz [$kg \cdot m^2$]	1.18E+09

Table 3: 10 MW spar parameters

4.2 15 MW Spar

An upscaled version of the 10 MW spar was created to support the IEA 15 MW reference turbine [1]. The scaling factor is based on the cube root of the turbine-mass ratio between the 10 and 15 MW turbine, but a larger scaling factor was used for some of the cross-sections to minimize the draft. The mean pitch angle was estimated using 1 DOF and 2 DOF tests (see Section 3.7.1 and 3.7.2, respectively) to achieve a similar angle to the 10 MW spar. Additionally, the design was made while minimizing the amount of steel. The upscaling procedure is presented in Section 3.7. The cross-section properties and parameters of the design are given in Table 4 and 5, respectively. The 15 MW spar is visualized in Figure 6b in Section 4.7.2.

Elevation wrt. SWL [m]	**Outer diameter [m]**	**Wall thickness [m]**
15	10	0.083
5	12.784	0.085
-5.583	12.784	0.085
-16.662	17.805	0.066
-30.670	23.783	0.078
-44.649	17.917	0.067
-51.640	15.453	0.059
-57.751	14.212	0.056
-64.349	16.477	0.062
-70.793	18.731	0.070
-78.423	22.431	0.086
-84.313	25.638	0.101

Table 4: 15 MW spar properties

Parameter	**Value**
Length of spar [m]	99.313
Draft [m]	84.313
Displacement [m^3]	22866
Steel mass [Te]	3881
Ballast (concrete) mass [Te]	17329
Total mass [Te]	21210
Vertical COG [m]	-69.65
Vertical COB [m]	-45.29
Ixx, Iyy [$kg \cdot m^2$]	1.13E+11
Izz [$kg \cdot m^2$]	2.08E+09

Table 5: 15 MW spar parameters

4.3 Wind Turbines

4.3.1 The DTU 10 MW Reference Wind Turbine

The DTU 10 MW Reference Wind Turbine was developed in a collaboration between the Wind Energy Department at the Technical University of Denmark (DTU) and Vestas (as part of the Light Rotor project [4]). A technical summary is given in Table 6. The 10 MW turbine is compared to the 15 MW turbine in Section 4.3.2 below.

4.3.2 The IEA 15 MW Reference Turbine

The IEA 15 MW Reference Turbine was developed in a collaboration between NREL, DTU and the University of Maine [1]. The turbine is summarized in the same table as the 10 MW turbine (Table 6).

Both concepts are horizontal-axis, three bladed, upwind turbines. The hub is located at a higher altitude for the 15 MW turbine, and it has larger rotor and hub diameters. The cut-in and rated wind speed (and rotor speed) is lower for the 15 MW turbine, but both turbines have a cut-out wind speed of 25 m/s. The NRA mass is increased by 50% for the 15 MW turbine. The 10 MW turbine has a medium speed, multiple stage gearbox, while the 15 MW has a low speed, direct drive system.

Description	DTU	IEA
Rating	10 MW	15 MW
Rotor orientation, configuration	Upwind, 3 blades	Upwind, 3 blades
Control	Variable speed, collective pitch	Variable speed, collective pitch
Drivetrain	Medium speed, multiple stage gearbox	Low speed, direct drive
Rotor, Hub diameter [m]	178.3, 5.6	240, 7.94
Hub height [m]	119	150
Cut-in, Rated, Cut-out wind speed [m/s]	4, 11.4, 25	3, 10.59, 25
Cut-in, Rated rotor speed [rpm]	6, 9.6	5, 7.56
Rated tip speed [m/s]	90	95
Overhang, Shaft tilt, Pre-cone	7.07m, 5°, 2.5°	11.35m, 6°, 4°
Pre-bend	3	4
Rotor mass	229 Te (each blade ~ 41 Te)	426 Te (each blade ~ 65 Te)
Nacelle mass	446 Te	591 Te
Nacelle-rotor assembly mass	675 Te	1017 Te

Table 6: 10 MW (DTU [4]) and 15 MW (IEA [1]) wind turbine summary

4.4 Towers

The towers were modeled using RIFLEX elements, which means that they act as beams according to Section 3.3.2. The tower is a crucial part of an FWT since it can experience large bending moments, usually at the base. It is often slender and as the turbines get larger, the distance between the hub (where the thrust force acts) and the tower base increases (leading to a larger moment arm).

The two towers used in this project are described here. Interestingly, the 10 MW tower is an optimized design with a different shape than the more conventional 15 MW tower design. This should be considered when assessing the results in Section 5.

4.4.1 10 MW Tower

The optimized tower from Hegseth et al. [17] is used, and the diameters and wall thicknesses are given in Table 7. Similar to the optimized spar, the shape of the tower is somewhat unconventional. Conventional towers used for FWTs are largest at the base, since the bending moment is usually largest here. The diameter of the 10 MW tower increases from the base (z = 10 m) to z = 20.5 m, before decreasing with altitude. However, the wall thickness is largest at the base.

Elevation wrt. SWL [m]	Outer diameter [m]	Wall thickness [m]
115.630	6.774	0.015
104.500	7.789	0.018
94.000	8.904	0.021
83.500	9.892	0.024
73.000	10.473	0.027
62.500	11.422	0.029
52.000	12.742	0.029
41.500	13.827	0.030
31.000	14.096	0.033
20.500	14.377	0.037
10.000	12.660	0.061

Table 7: 10 MW tower properties (from Hegseth et al. [17])

4.4.2 15 MW Tower

Instead of upscaling the tower used for the 10 MW spar, the 15 MW tower is based on the same tower used by the University of Maine for a 15 MW semi-submersible [15]. In contrast to the 10 MW tower, this is designed in a more conventional manner. Its largest diameter is at the base, and decreases when moving up along the tower (except for the small increase from 28 to 41 m, see Table 8). The thickness is largest at the base and decreases with altitude, but has a slight increase at the top sections.

Elevation wrt. SWL [m]	Outer diameter [m]	Wall thickness [m]
15	10	0.0830
28	9.964	0.0831
41	9.967	0.0828
54	9.927	0.0299
67	9.528	0.0278
80	9.149	0.0256
93	8.945	0.0229
106	8.735	0.0203
119	8.405	0.0183
132	7.321	0.0212
144.582	6.5	0.0212

Table 8: 15 MW tower properties (from IEA [15])

4.5 Mooring Configuration

The mooring configuration was based on Hegseth et al. [17]. Three lines were used in a catenary mooring system with 120 degrees between them, see Figure 3. The mooring parameters are given in Table 9. The parameters from Hegseth et al. was used to find EA_{moor}, A_{moor} and m_{moor} using the theory presented in Section 3.6. The diameter of the spar at the fairleads vertical position ($D_{spar,fairlead}$) was found by using linear interpolation and Table 2. The mooring parameters was used to establish the fairlead and anchor locations, presented in Table 10.

Parameter	**Value**
D_{moor} [m]	0.081*
$z_{fairlead}$ [m]	-10.7*
L_{moor} [m]	1497.2*
x_{moor} [m]	1433*
EA_{moor} [N]	5.9E8
A_{moor} [m^2]	0.00515
m_{moor} [kg/m]	131
$D_{spar,fairlead}$ [m]	13.2

Table 9: Mooring parameters (*taken from Hegseth et al. [17])

Point	**X**	**Y**	**Z**
Fairlead1	-6.6	0	-10.7
Fairlead2	3.3	5.7	-10.7
Fairlead3	3.3	-5.7	-10.7
Anchor1	-1439.6	0	-320
Anchor2	719.8	1246.7	-320
Anchor3	719.8	-1246.7	-320

Table 10: Fairlead and anchor locations

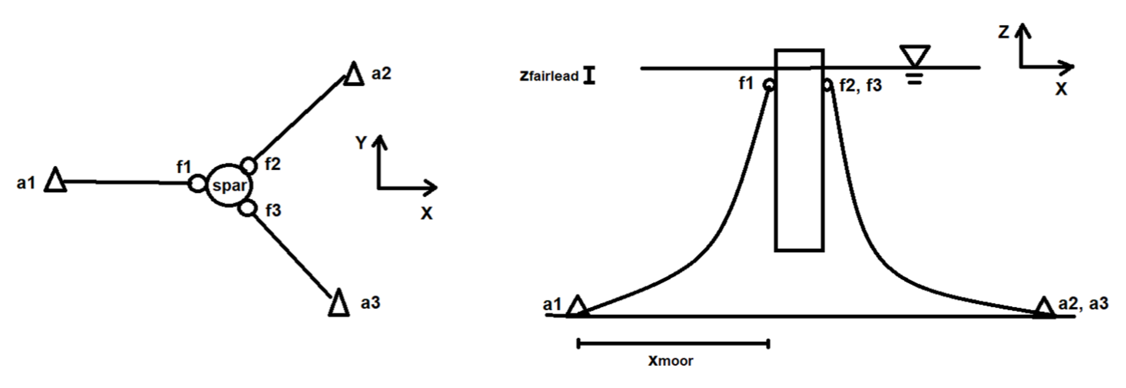

Figure 3: Mooring configuration showing anchor (a1, a2, a3) and fairlead (f1, f2, f3) points

4.6 Models

Before presenting the software modeling procedure in Section 4.7, it is convenient to introduce the models first. The models are different depending on wave load models, elasticity and size. Therefore, their names are based on this. An overview of all the models is given in Table 11. Note that the upscaled versions are not included in the table since they are based on the same concepts as the respective 10 MW versions.

The first model presented is the RigidPFT, where a panel model created in GeniE is used for a SIMO-body to represent a rigid hull based on linear potential flow theory (PFT), see Section 4.6.1. In Section 4.6.2, the same panel model is used but wave loads are modeled according to Morison's equation (ME). RIFLEX elements are used to represent an elastic spar based on beam formulation for the FlexME design in Section 4.6.3. WAMIT is used to generate the radiation and diffraction loads for FlexPFT and uses the same RIFLEX model as FlexME (Section 4.6.4).

Name	RigidPFT	RigidME	FlexME	FlexPFT
Model type	Panel	Panel	Beam	Beam
Software	GeniE, HydroD	GeniE	RIFLEX	RIFLEX, WAMIT
Elasticity	Rigid	Rigid	Flexible	Flexible
Wave load model	PFT	ME	ME	PFT

Table 11: Modelling Concepts

4.6.1 RigidPFT

The panel model for RigidPFT hull was created in GeniE based on Table 2. The panel model is continuous and does not represent elasticity, and is therefore rigid. HydroD is used to run a Wadam analysis, in order to attain hydrodynamic attributes according to linear potential flow theory (PFT). This includes frequency dependent added mass, damping, excitations and hydrostatic stiffness data. C_{44} and C_{55} are calculated based on the theory presented in Section 3.2.2, since the values calculated by HydroD does not account for the concrete ballast. For the same reason, the moment of inertia from HydroD is replaced with calculated values. A value is included for C_{66} to avoid numerical instability.

Quadratic drag is not attained from the Wadam analysis. This is represented by adding "slender elements" to the hull. Quadratic drag coefficients are used, and the value is determined in Section 3.2.4 ($C_d = 0.8$). The panel model, hydrodynamic attributes and slender elements are added to a SIMO-body, which will be used in the SIMA analyses. The 15 MW version of the RigidPFT design, which will be referred to as RigidPFT-15MW, is created in the same manner. The only difference is that the geometry is based on the upscaled spar, see Table 4.

4.6.2 RigidME

The same panel model created for RigidPFT was used for RigidME. However, the hydrodynamic loads are based on Morison's equation (ME). Hence, the hydrodynamic attributes from HydroD are removed from the SIMO-body, except for the hydrostatic stiffness data (ME does not provide estimates for this). The moment of inertia was the same. To account for added mass, slender elements was added to the hull with added mass coefficients, which is determined in Section 3.2.4 ($C_a = 1.0$). Quadratic drag coefficients was also used (still $C_d = 0.8$).

ME and strip-theory do not provide an appropriate estimate for added mass in heave (see Section 3.2.3). Hence, the zero-frequency A_{33} calculated by HydroD for the RigidPFT model was added to a slender element connected to the bottom of the RigidME model. ME is a long-wave approximation, which means that the zero-frequency A_{33} should be the most representative value. Also, added mass in heave is considered an end-effect for classical, cylindrical, constant diameter spars [34]. The spar used here has varying diameters, and adding A_{33} at the bottom is a simplification.

4.6.3 FlexME

The flexible hull for FlexME was created using RIFLEX elements that behave according to beam formulation (see Section 3.3.2). FlexME and FlexME-15MW is based on Table 2 and 4, respectively, similarly to RigidPFT and RigidPFT-15MW. However, a finer discretization was used for the flexible hulls to achieve a good representation of the elastic behavior (it was also convenient for the WAMIT integration for FlexPFT, see Section 4.6.4). Additionally, RIFLEX elements can only have constant diameters and thicknesses and more sections was therefore needed in order to accurately represent the geometry of the hull.

The elevation with respect to SWL was chosen such that no elements intersect the SWL (z = 0) or the fairleads connection at z = 10.7 m. A finer discretization from SWL to the fairleads connection was used since it is more loads acting at the top of the spar. Hence, it is interesting to represent the elastic behavior in this region more accurately. Linear interpolation was used to divide the designs into more sections. The geometry of the 10 and 15 MW flexible spars are given in Appendix A.

Quadratic drag and added mass coefficients are added directly to the cross-sections (RIFLEX elements). Thus slender elements are not needed. A_{33} is added at the bottom cross-section. After experiencing larger heave motions (compared to rigid models), the Froude-Krylov load term in the vertical direction was neglected for the flexible models. According to the RIFLEX user manual [32], the added mass in the tangential direction of a cross-section (which is the vertical direction in this case) is given with the formula for added mass in surge from Equation 28 in Section 3.2.3. This suggests that the RIFLEX formulation is more appropriate for a ship hull, and therefore this term needs to be neglected for the flexible models. This resulted in FlexPFT having heave motions similar to the rigid models, while FlexME displayed a slightly smaller heave motion.

The flexible models calculate the restoring forces in heave, roll and pitch on their own, and it is not necessary to add a hydrostatic stiffness matrix including these terms. However, larger yaw motions were experienced, especially for high wind speeds. A restoring force in yaw, C_{66}, was therefore needed to avoid numerical instabilities (similar to the rigid models). This was added to a "dummy" SIMO-body connected to the flexible models, located at the origin (0,0,0). This resulted in similar yaw motions between the rigid and flexible models. Unfortunately, this lead to a difference in yaw inertia between the models. This is indicated by the results from the yaw decay tests in Section 5.5.

4.6.4 FlexPFT

For the FlexPFT design, the initial step was to create a panel model in GeniE based on the geometry given in Appendix A. The panel model was created in a similar fashion to the rigid model, except that "feature edges" were added to subdivide the geometry. A Wadam analysis was performed in HydroD to attain the input files needed for the WAMIT integration. WAMIT was used to obtain frequency-dependent added mass, damping and excitation forces for each panel. This was added to RIFLEX elements in SIMA, using a new feature called "Potential flow library".

The RIFLEX model created for FlexME was used for FlexPFT, but a different hydrodynamic load formulation was used for the cross-sections. FlexME used "Morison" load formulation, while FlexPFT used "Potential flow with quadratic drag load coefficients". Consequently, no added mass coefficients were used for FlexPFT, but the same quadratic load coefficient was used.

4.7 Software Modelling Procedure

The software used for the modeling part of this project is presented here. GeniE-modelling of panel models is described in Section 4.7.1. The procedure for attaining hydrodynamic attributes in HydroD, along with visualizations of the spars, are given in Section 4.7.2. Furthermore, the WAMIT integration process is explained in Section 4.7.3. At last, RIFLEX elements used for modeling elasticity in towers and spars are introduced in Section 4.7.4.

4.7.1 GeniE

GeniE was used to create panel models for the rigid spars. Due to symmetry about the x- and y-axis, only one-fourth of the spar was modeled to reduce computational effort (the entire spar is represented in HydroD, see Section 4.7.2). Diameters and thicknesses are based on Table 2 in Section 4.1, but equivalent thicknesses were used assuming that the thicknesses vary linearly between the cross-sections. Equivalent thicknesses and density were assigned to the hull to ensure that HydroD calculates the mass moment of inertia (I) about the origin. This was done to obtain a reference value, but HydroD underestimates I since the concrete ballast was not included. The mass of the ballast was correct, but HydroD uses seawater instead of concrete. The surface of the hull was modeled as a wet surface, and a dummy hydrodynamic load was used to specify that the surface should be subjected to hydrodynamic loads and pressure. A mesh with an element length of 1 m was used (see Figure 5). The panel model used for the 10 MW rigid spars is shown in Figure 4a.

The 15 MW panel models were made following the same steps mentioned above, except that the geometry is different. Diameters and equivalent thicknesses are obtained from Table 4 in Section 4.2. A visualization of the 15 MW spar is given in Figure 6b in Section 4.7.2.

Panel models of the FlexPFT designs were also created in GeniE, since a panel model was needed in HydroD to generate the input files for WAMIT. It was only used in HydroD, not for the SIMA analyses of FlexPFT. The modeling approach was similar to the one used for the rigid models, but feature edges were used to subdivide the geometry to create a mesh suitable for the WAMIT integration. As a result, the panel model was divided into more sections. This is visualized in Figure 4, and the discretization of the flexible models is given in Appendix A.

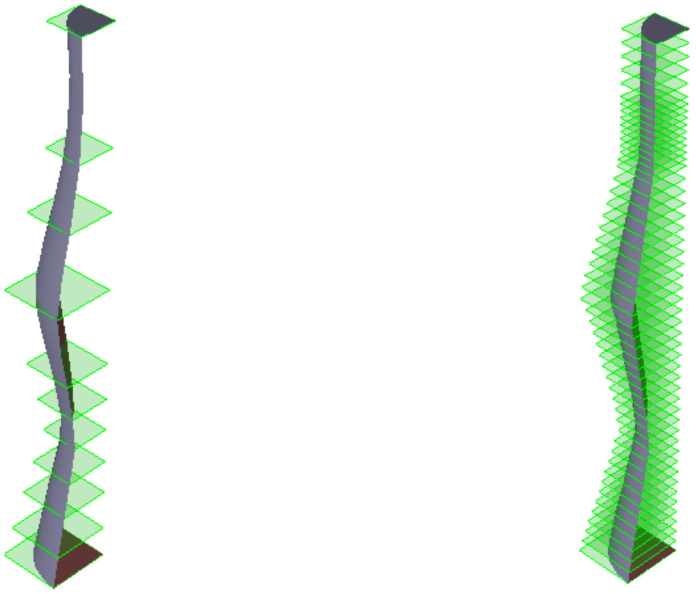
(a) For rigid spars

(b) For flexible spar (FlexPFT)

Figure 4: 10 MW panel models created in GeniE

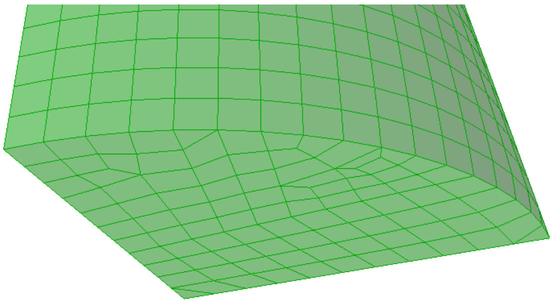
Figure 5: Mesh visualized for the 10 MW panel models

4.7.2 HydroD

After creating the panel model in GeniE, it was used in HydroD to acquire hydrodynamic attributes. Since only one-fourth of the spar was created in GeniE, the first step was to include symmetry in the xz- and yz-axis. The waterline and trim were set to zero to ensure the desired draft with no trim. The mass, COG and BG (COB to COG distance) of the FWT (spar, ballast, tower, NRA) was given as inputs. The entire FWT was considered here since the other parts of the assembly will affect the hydrodynamic attributes of the spar. If the spar is not in static equilibrium, a small change in the waterline or trim can appear. The waterline changed from 0 to -0.01 m in one case. The small change indicates that the input was slightly inaccurate. The desired draft was achieved by using a feature in HydroD called "Fill from buoyancy", which makes changes to the input in order to get the specified waterline and trim. Since the error was small, the change in mass and COG was insignificant.

After making sure that the draft was correct and that there were no trim, a direction and frequency set was specified. Directions from 0 to 360 degrees with a 15-degree step and wave periods from 3 to 60 seconds with a 1-second step were used. For the models made for the flexible designs, the input files for WAMIT were generated by specifying "Save temp. Wamit files" before performing the analysis. The last step was to run the Wadam analysis, which was executed from HydroD.

(a) 10 MW

(b) 15 MW

Figure 6: Spar models visualized in HydroD

4.7.3 WAMIT

After generating the WAMIT input files in HydroD, the files needed to be modified in order to store the correct information. The water depth was set to 320 m, the wave periods and directions were set equal to what was used in HydroD (Section 4.7.2), and the COG of the entire FWT assembly was included. Also, it was needed to specify to run the radiation and diffraction problems.

The WAMIT analysis was then executed, and the output files were used in an in-house MATLAB script. The script utilizes WAMIT results to transform the added mass, damping and wave-excitation of the spar, and produces WAMIT type output files for each section. Before executing the MATLAB script, changes needed to be made to fit the geometry of the specific case. The original script was based on equal spacing between the panels for an entire spar. The 10 and 15 MW spars needed personalized scripts in order to account for the distance between panels, since the increment is larger below the fairlead location (10.7 m below SWL).

After utilizing the script, separate output files for each panel containing frequency-dependent added mass, damping and excitation forces are obtained. Another in-house program (SIMATOOL) was used to create input files that can be inserted into the new feature in SIMA (potential flow library). By specifying the hydrodynamic load formulation of the cross-sections as "Potential flow with quadratic drag load coefficients", it is possible to assign the hydrodynamic loads found using WAMIT to RIFLEX cross-sections.

4.7.4 RIFLEX

The towers and flexible spars were modeled using RIFLEX elements with thin-walled pipe cross-sections. The diameter, thickness, density ($\rho = 7850$ kg/m^3 for spar, $\rho = 8500$ kg/m^3 for tower, see Hegseth et al. [17]), elastic ($E = 210$ GPa) and shear modulus ($G = 81$ GPa) was specified for each section. Froude-Krylov scaling was neglected in the tangential direction (vertical direction in this case) for the spars, as explained in Section 4.6.3. Quadratic drag coefficients ($C_d = 0.8$) were added for the spar models, but not for the towers. Added mass coefficients were added to FlexME. The load formulation "Morison" was used for FlexME, while "Potential flow with quadratic drag load coefficients" was used for FlexPFT. The beam formulation describing the behavior of these RIFLEX elements is given in Section 3.3.2.

Mooring lines was represented by bar elements (only deformed in axial direction [31]) with axisymmetric cross-sections. The mass coefficient (131 kg/m), external cross-section area (0.0052 m^2), gyration radius (0.05 m) and axial stiffness (1.51 GN) was given as input. In addition, the blades, nacelle and shaft are modeled as beam elements. This was not made for the project, but provided from existing, in-house models. Since little attention was given to these parts of the FWT in the analyses, they will not be described further.

4.8 Controllers

The 10 and 15 MW control systems were provided from existing in-house controllers, and have not been modified (except for minor adjustments). The controller settings determine how the wind turbine should behave and react to changes in wind, tip-speed-ratio (TSR), and more. Moreover, the minimum pitch angles specified for the blades depending on wind speed are shown in Figure 7. This was used to minimize power loss for low wind speeds, and reduce loads for higher wind speeds (see Section 3.4).

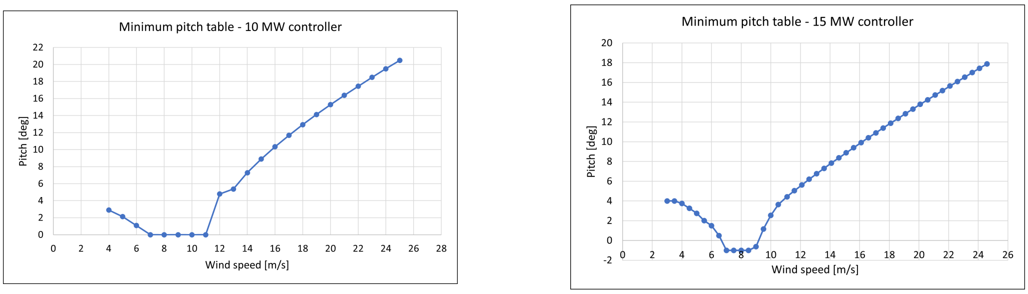

(a) 10 MW

(b) 15 MW

Figure 7: Minimum pitch angle tables for blades, specified in the controllers

4.9 Generating Wind Files

Wind files were generated using TurbSim, which is a stochastic, full-field, turbulence simulator [28]. The wind files were needed for the irregular waves tests, and the wind speeds and turbulence intensities from Table 12 in Section 5.7 were used. Unique seeds are used for each sea condition, which creates random phases for the wind components.

There are different boundary conditions for the 10 and 15 MW turbines. The hub height is 150 m for the 15 MW, in comparison to 119 m for the 10 MW. The wind speed varies with altitude, and if the same wind conditions were to be applied for the 10 and 15 MW turbines the wind speed needed to be scaled up for the 15 MW turbine. The wind profile power law was used with $\alpha = 0.14$.

Furthermore, the diameter of the span is 180 m for the 10 MW and 240 m for the 15 MW turbine. This needs to be considered when choosing the boundaries of the modeled wind speed, ensuring that the entire span is covered during the simulations regardless of platform motions. A 200x200 m grid was used for the 10 MW turbine, while a 280x280 m grid was used for the 15 MW turbine.

4.10 Filtering

In order to find the RAO from the regular waves tests, the amplitudes need to be determined (see Section 3.5). But the results do not always oscillate around zero, and there could be unwanted transient parts at the beginning or end of the simulations which is not representative for the actual response. An example of bending moment taken directly from the SIMA results is shown to the left in Figure 8. The dark line represents the mean value of the response, and indicates that it is not oscillating around zero.

A band-pass (BP) filter was used to filter out unwanted frequencies. The lowest and maximum frequencies were set to $0.9/T$ and $1.1/T$, respectively, where T is the wave period. In the middle of Figure 8, the response after applying a BP filter is shown. The response is now oscillating around zero, and there are fewer spikes. However, transient parts are still present at the end and beginning of the simulation.

An appropriate time slot was chosen for the specific cases to remove the transient parts. This is indicated by the two vertical, dashed lines in the middle of Figure 8. Accordingly, the time slot was from time step 4000 to 8000 in this case (400 to 800 s, since the time step was 0.1 s). The end result is displayed to the right in Figure 8, from which the amplitudes used for the RAO was extracted.

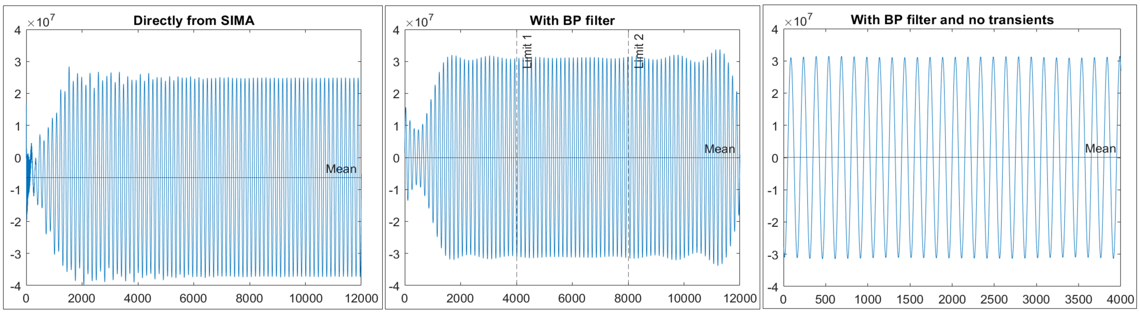

Figure 8: Example of band-pass (BP) filter used for bending moment (x-axis is time steps, y-axis is bending moment in Nm)

5 Results

In the results section, the FWTs properties will be evaluated and compared. First of all, the excitations, added mass and damping behavior will be assessed in Section 5.1, 5.2 and 5.3. The results from the constant wind tests was used to verify that the turbines behaved as expected (see Section 5.4). Decay tests were used to establish natural periods and damping coefficients in Section 5.5. Regular waves tests were performed in order to construct RAOs for motions, bending moment and stress in Section 5.6. Finally, 1-hr analyses for 15 sea conditions in irregular waves with turbulent wind were carried out to study the fatigue damage and power spectrums of the spars and towers (Section 5.7).

5.1 Excitations

The wave excitations on the spars for the different wave load models are presented here. The PFT models are based on linear potential flow theory (Section 3.2.1), and the results are extracted from the Wadam analysis in HydroD. The excitations for the ME-models are estimated based on Morison's equation (ME) and strip theory (see Section 3.2.3).

5.1.1 Surge

Excitations in surge are shown in Figure 9. ME models (dashed lines) exhibits surge excitations similar to the PFT-models (solid lines) for low wave frequencies ($\omega < 1$ rad/s). As the frequency increases, the surge excitations are larger for the ME models. The 15 MW models (red lines) have a larger deviation between wave load models for high frequencies, which indicates that the deviation between PFT and ME increase for a larger spar. This is expected according to theory (Section 3.2.3) as ME assumes the diameter of the spar to be small compared to wavelength ($\lambda/D > 5$).

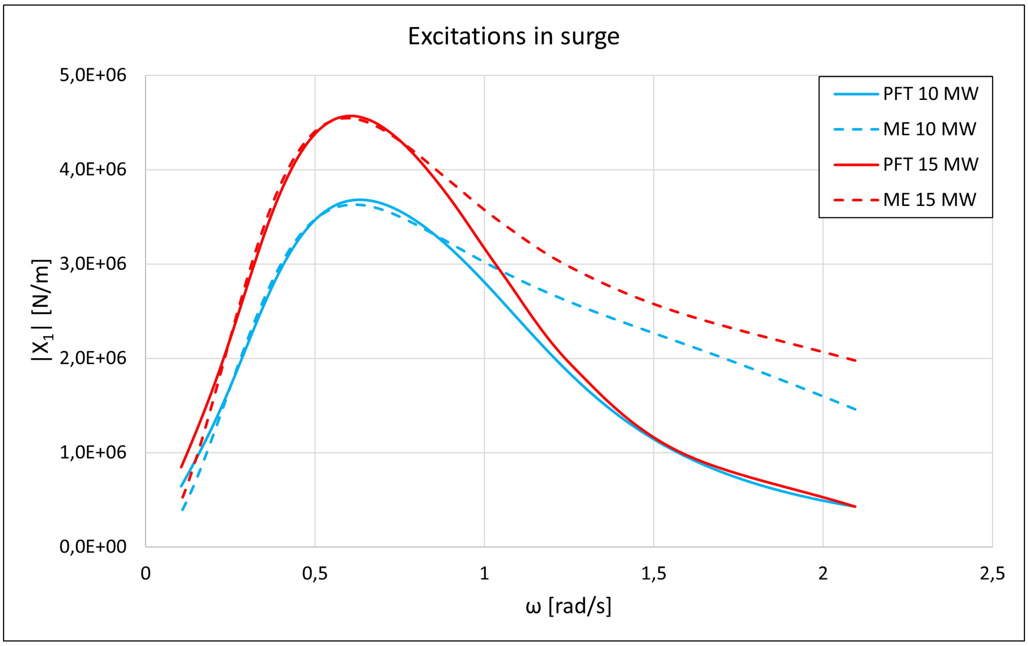

Figure 9: Wave excitations in surge

5.1.2 Heave

There are large deviations between PFT and ME models for excitations in heave (see Figure 10). ME does not give estimates for heave excitations, and it is instead estimated by the Froude-Krylov force and added mass in heave (as explained in Section 3.2.3, see Equation 26). Apart from having larger excitations, the upscaled spars excitations exhibit similar behavior to the 10 MW spars.

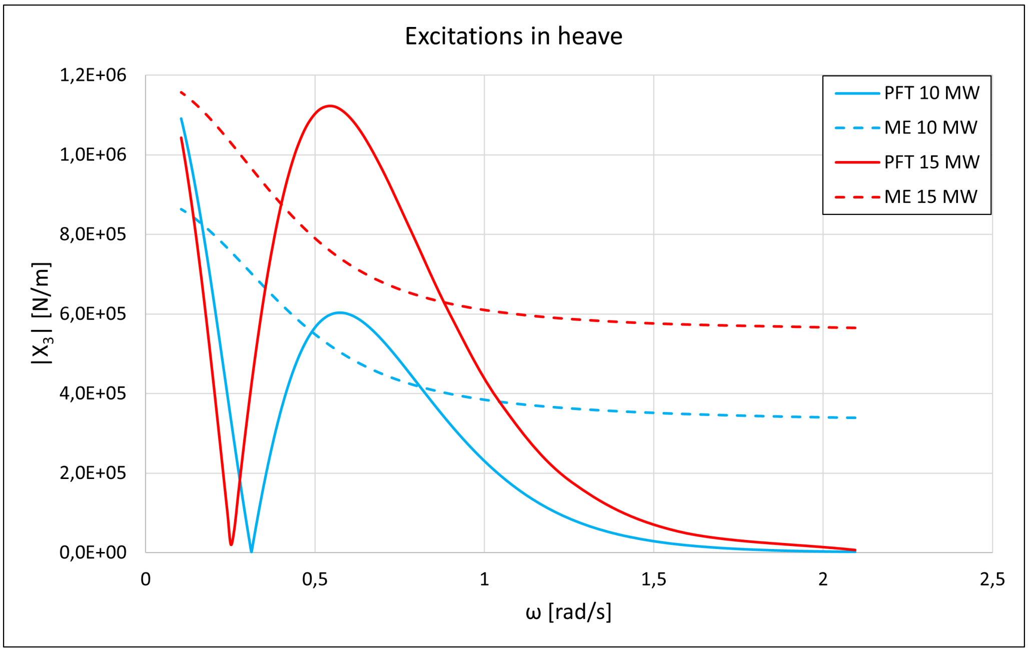

Figure 10: Wave excitations in heave

5.1.3 Pitch

The excitations in pitch (Figure 11) show, similarly to surge, that the different wave load approaches display similar results for low frequencies and the ME models have higher excitations for higher frequencies. Note that the 10 and 15 MW ME models merge for higher frequencies, which is in contrast to the surge excitations (where 15 MW models have larger excitations than 10 MW in this frequency region). This suggests that upscaling the spar does not lead to a larger deviation between ME and PFT for pitch excitations.

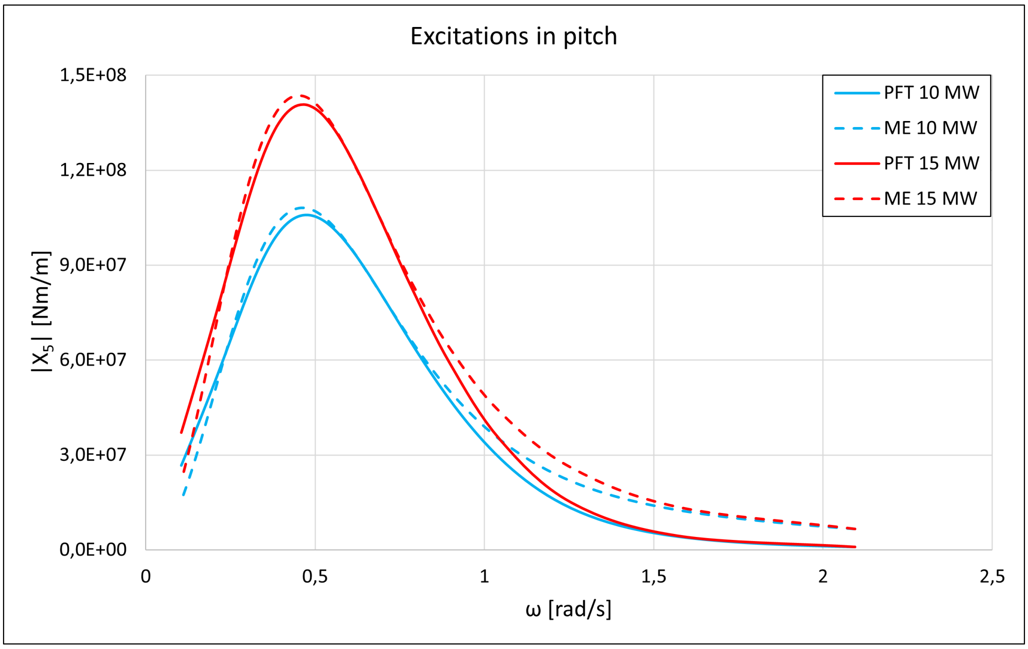

Figure 11: Wave excitations in pitch

5.2 Added Mass

The added mass varies depending on the wave load model. The most important difference is that the ME models have frequency-independent added mass. This results in larger deviations between the PFT and ME models for certain frequencies, i.e. high frequencies for surge and heave. Both the HydroD (RigidPFT) and WAMIT (FlexPFT) results are included here. Since the spars are symmetrical in the xz- and yz-plane, the added mass coefficients in surge and pitch will be identical to sway and roll, respectively. Therefore, only surge, heave, pitch and coupled surge-pitch added mass coefficients are presented.

5.2.1 Surge

In Figure 12 the added mass in surge is close to the total mass of the system (16 and 23.4 thousand tonnes for 10 and 15 MW FWTs, respectively). The added mass is larger for the ME models, especially for high frequencies. Observe how similar the results for HydroD (dotted lines) and WAMIT (dashed lines) are for both 10 and 15 MW spar. The deviation between ME and PFT is slightly larger for 15 MW spar.

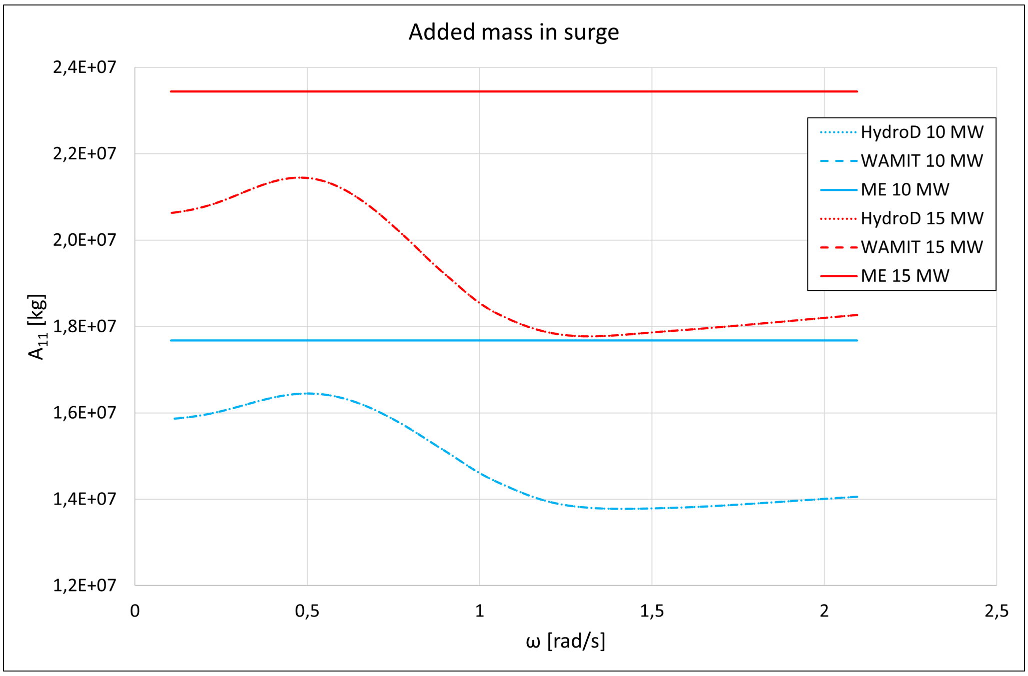

Figure 12: Added mass in surge for different calculation methods

5.2.2 Heave

The added mass in heave is shown in Figure 13. As mentioned earlier, the zero-frequency A_{33} from the PFT model was added to the bottom of the ME models. This is visualized at the lowest frequency, where the added mass is almost identical for both methods. Again HydroD and WAMIT demonstrate similar results, and the deviation between ME and PFT is slightly larger for 15 MW spar.

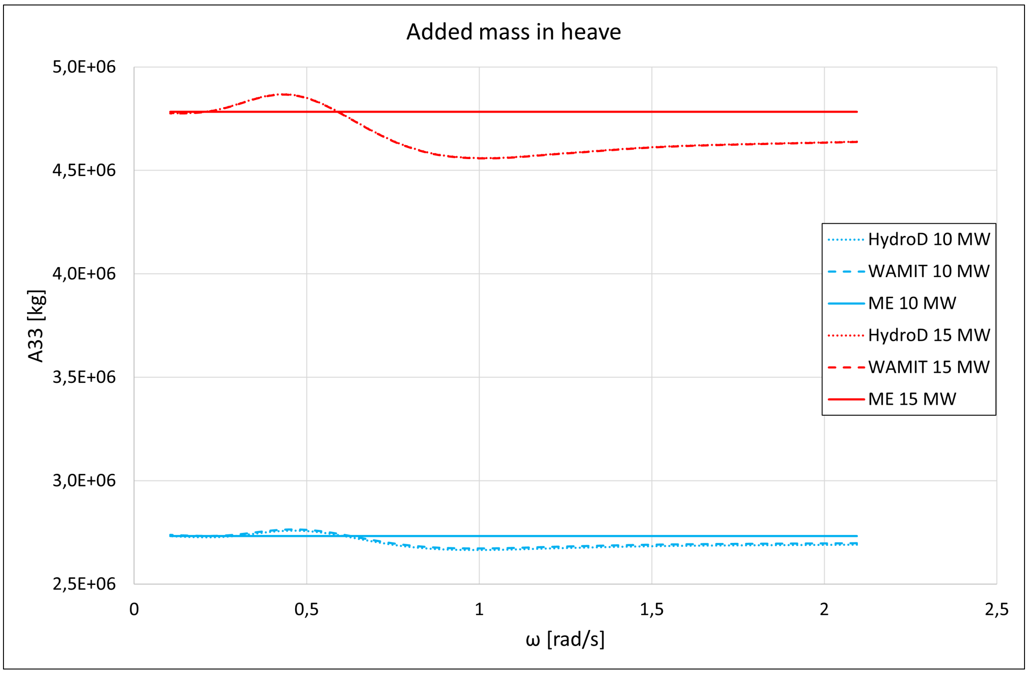

Figure 13: Added mass in heave for different calculation methods

5.2.3 Pitch

Added mass in pitch is shown in Figure 14, which exhibits that the ME models have larger values than the PFT models. WAMIT is slightly larger than HydroD for low frequencies, but again HydroD and WAMIT show good agreement. Similar to the surge and heave results, the variation between ME and PFT is slightly larger for the upscaled spar.

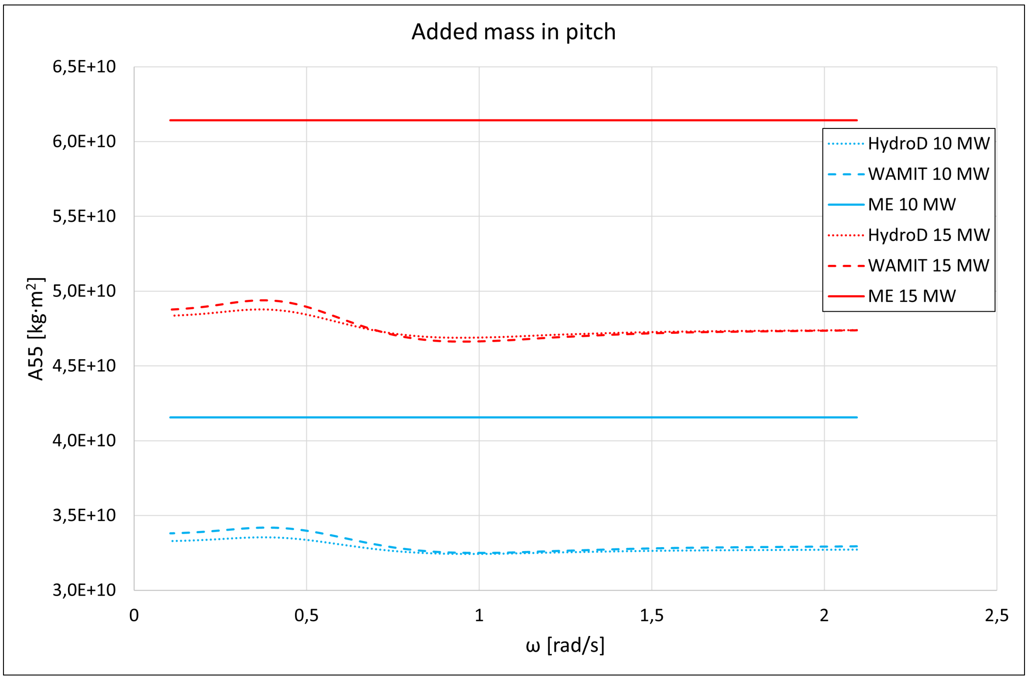

Figure 14: Added mass in pitch for different calculation methods

5.2.4 Surge-Pitch

The coupled added mass in surge-pitch exhibits similar behavior for WAMIT and HydroD, but HydroD (dotted lines) is marginally larger (see Figure 15, beware of the negative sign). In contrast to the previous results for added mass, ME displays smaller values than PFT in surge-pitch. However, the difference between the methods is still largest for the 15 MW model.

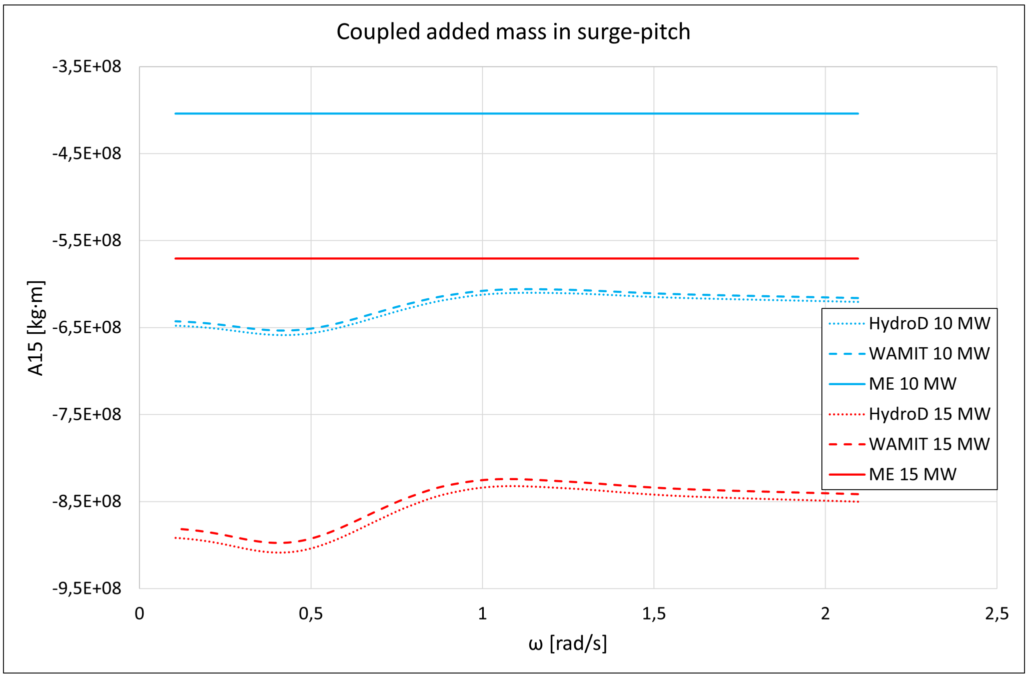

Figure 15: Coupled added mass in surge-pitch for different calculation methods

5.3 Damping

The damping from the HydroD and WAMIT calculations are presented here. For the same reasoning as for added mass, only surge, heave, pitch and surge-pitch are presented. No radiation damping was modeled for ME, but quadratic damping is included as explained in Section 4.6 (which is the same for all models). As a consequence, no results for ME are included here.

5.3.1 Surge

Figure 16 displays the damping in surge (B_{11}). The results from HydroD (dotted lines) and WAMIT (dashed lines) are practically identical for both 10 and 15 MW spars. The 15 MW models experience higher damping values, especially near $\omega = 1$ rad/s. The wave excitation in surge is larger for the upscaled spar in this frequency region, see Figure 9 in Section 5.1. For the lowest and highest frequencies, the damping values coincide for the 10 and 15 MW models, where the excitations in surge are similar.

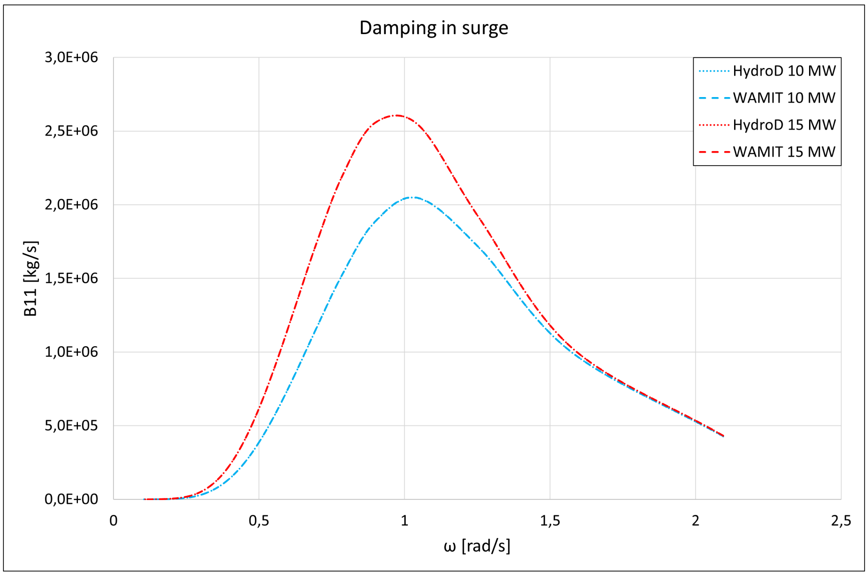

Figure 16: Damping in surge for different calculation methods

5.3.2 Heave

The damping in heave (B_{33}) is presented in Figure 17. Again, the HydroD (dotted lines) and WAMIT (dashed lines) results are identical. The 15 MW models have an approximately three times larger damping compared to the 10 MW models around $\omega = 1$ rad/s. The excitations in heave are larger for the 15 MW spar and it has larger diameters and draft. B_{33} is moving towards zero for low and high frequencies since no waves are generated by the spar for such frequencies.

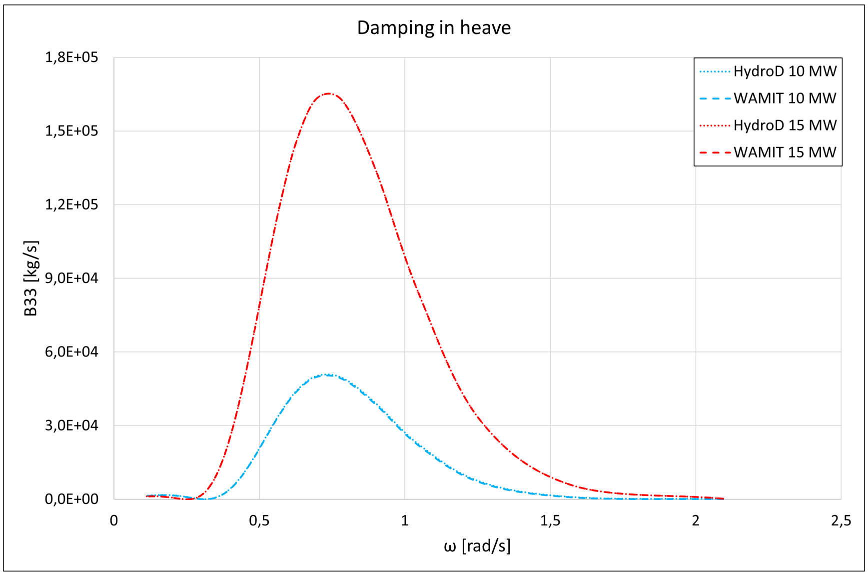

Figure 17: Damping in heave for different calculation methods

5.3.3 Pitch

Figure 18 reveals that WAMIT (dashed lines) computes a larger damping in pitch (B_{55}) than HydroD (dotted lines) for both 10 MW and 15 MW models. The spar was divided into panels with a length of 1-2 meters for the WAMIT integration and calculated the damping for each panel. HydroD estimates the damping for a continuous spar. It is reasonable to believe that WAMIT yields the most accurate B_{55}.

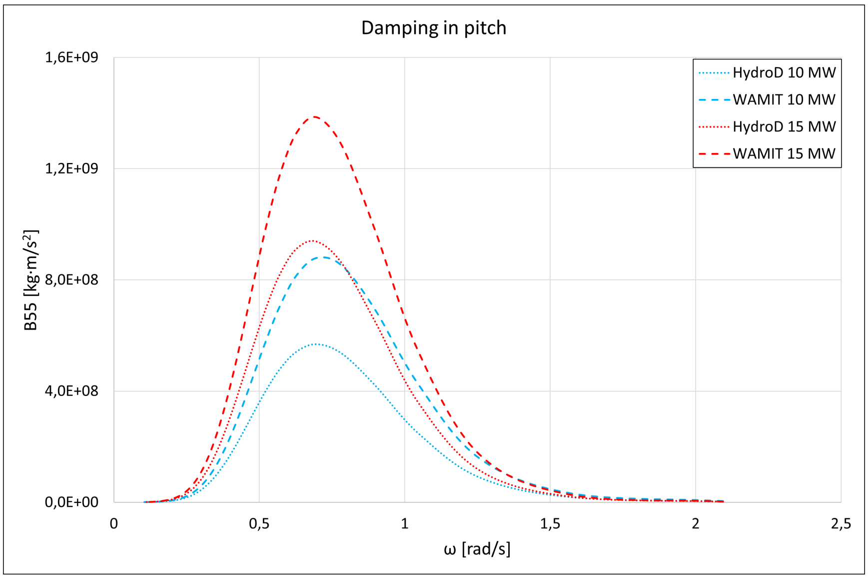

Figure 18: Damping in pitch for different calculation methods

5.3.4 Surge-Pitch

Coupled surge-pitch damping (B_{15}) is shown in Figure 19. HydroD (dotted lines) displays slightly higher damping for certain frequencies ($0.6 < \omega < 1.5$). Based on the discussion in Section 5.3.3, WAMIT is most likely the more accurate estimate.

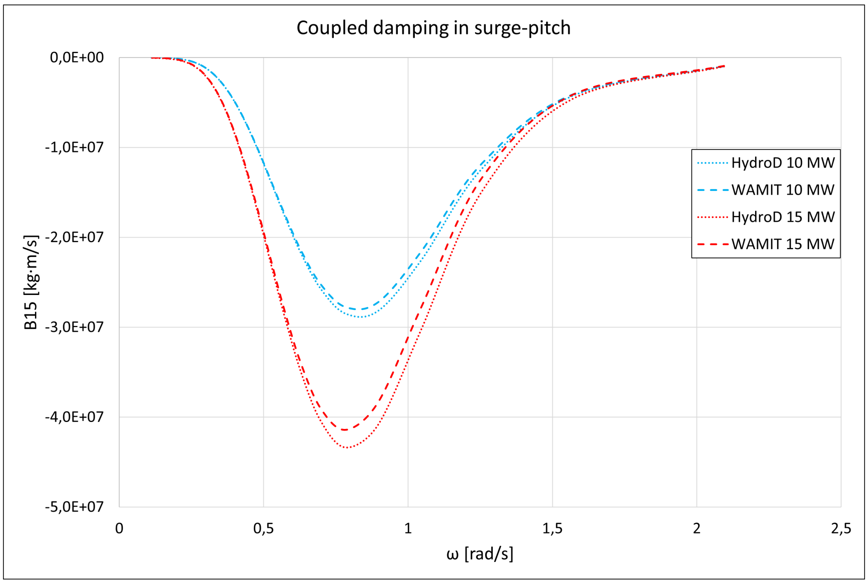

Figure 19: Coupled damping in surge-pitch for different calculation methods

5.4 Constant Wind Tests

The constant wind tests were conducted in order to verify that the controllers behaved as expected and to study spar motions. RigidPFT and FlexPFT (both 10 and 15 MW models) were tested for wind speeds ranging from cut-in to cut-out wind speeds. Fixed 10 and 15 MW rotors are also tested. The mean values for rotor speed, thrust, torque, power and blade pitch are presented as functions of wind speed (U_w). The mean surge and pitch motions of the spars are also included. The mean values were taken after the turbine and spar had reached steady-state position to make sure transients did not interfere with the results.

5.4.1 Rotor Speed

The fixed rotors (red lines, Figure 20) are behaving according to the cut-in and rated rotor speeds presented in Section 4.3. For 10 MW models, RigidPFT (blue circles) and FlexPFT (black triangles) are close to the fixed rotor. They are slightly smaller for above rated, likely due to the pitch angle of the spars (the rotor will experience an incoming wind speed with an angle). The 15 MW spars also exhibit good agreement with the fixed rotor, although the rotor speed is slightly lower for U_w = 11-12 m/s.

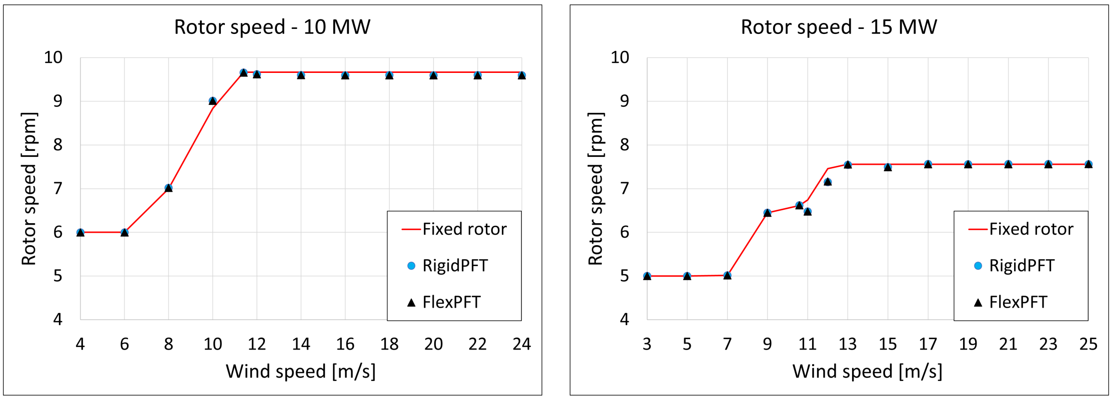

(a) 10 MW (b) 15 MW

Figure 20: Mean rotor speed

5.4.2 Thrust

Mean thrust is presented in Figure 21, which displays that it is increasing proportional to the wind speed squared (thrust $\propto U_w^2$) until rated wind speed (11.6 and 10.59 m/s for 10 and 15 MW turbines, respectively). At rated wind speed the blade pitch control is activated and the thrust will decrease. This is similar for all models.

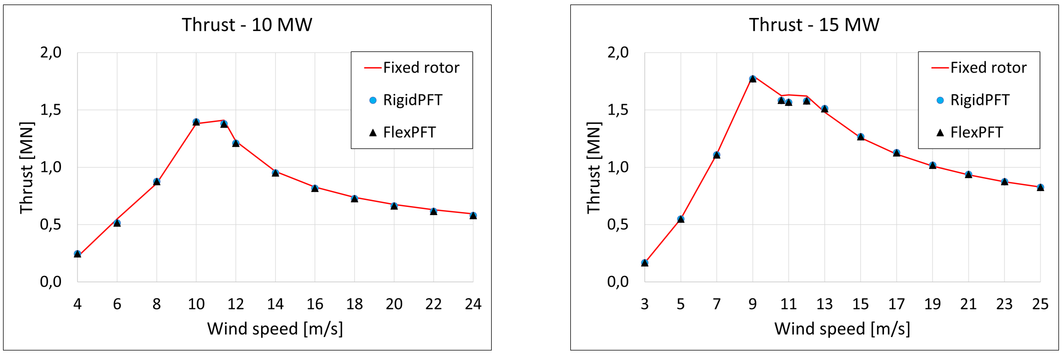

(a) 10 MW (b) 15 MW

Figure 21: Mean thrust

5.4.3 Torque

The torque increases until rated wind speed where it stabilizes at rated torque (Figure 22).

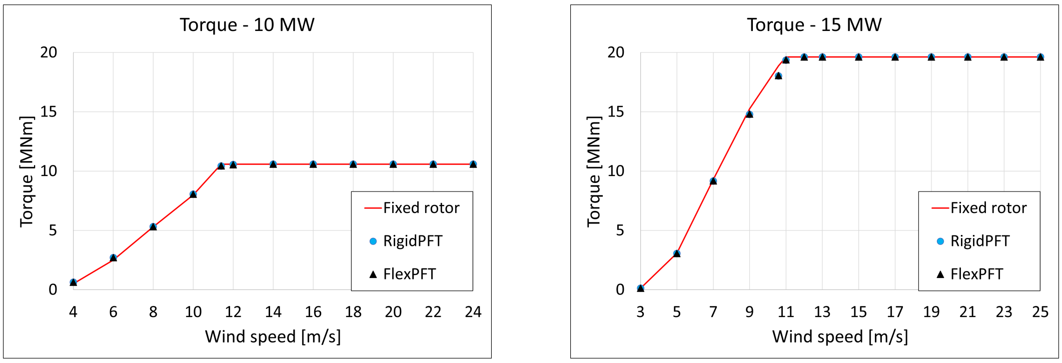

(a) 10 MW (b) 15 MW

Figure 22: Mean torque

5.4.4 Power

Figure 23 shows that the power increases with wind speed cubed (Power $\propto$ U^3), then stabilizes at rated power from rated speed and onwards.

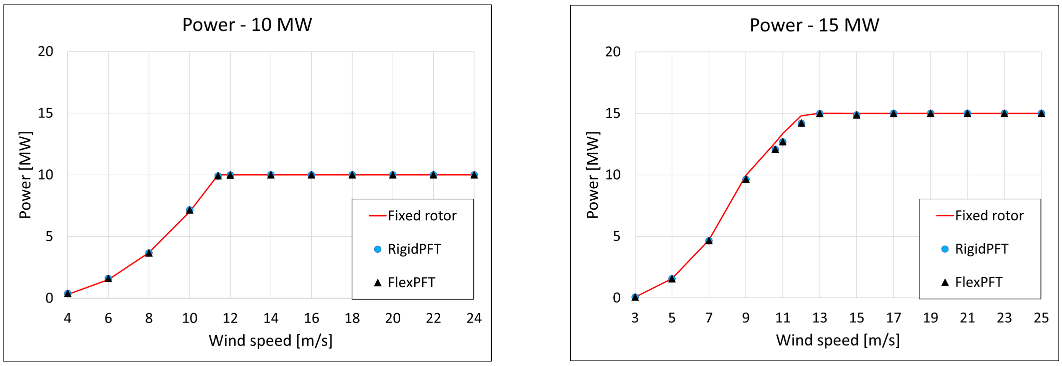

(a) 10 MW (b) 15 MW

Figure 23: Mean power

5.4.5 Blade Pitch

The blade pitch is initially non-zero to maximize the power output at low wind speeds, and increases from rated wind speed to limit structure motions while maintaining the rated power (see Figure 24). The blade pitch is behaving as specified in the minimum pitch table for the controller (see Section 4.8), except that it is 0 instead of -1 degrees from U_w = 7-9 m/s for the 15 MW turbine. This is because the minimum blade pitch is set to 0 degrees.

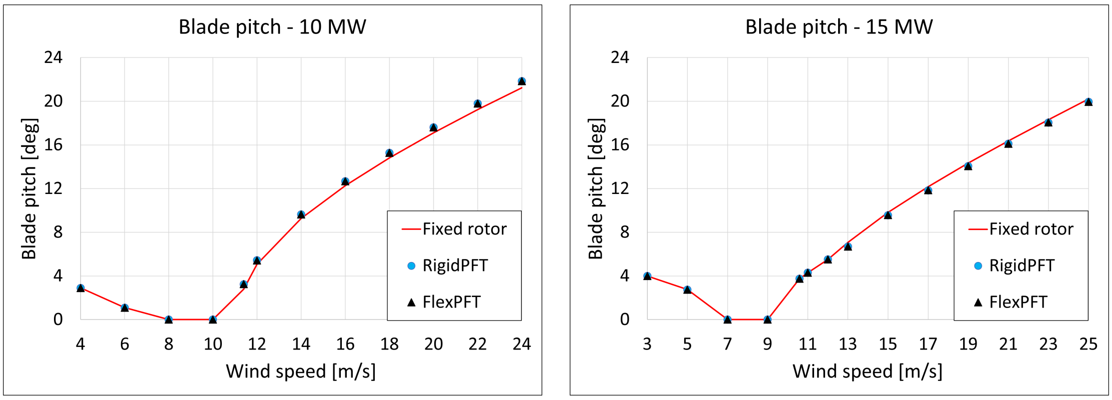

(a) 10 MW (b) 15 MW

Figure 24: Mean blade pitch

5.4.6 Mean Spar Motions

The mean motions of the spars in surge and pitch are presented in Figure 25. RigidPFT and FlexPFT exhibit similar results for both 10 and 15 MW models. The 15 MW models have larger mean motions, which is expected since the thrust forces are larger for the 15 MW turbine. The motions are largest around rated wind speed, but decrease as blade pitch control activates.

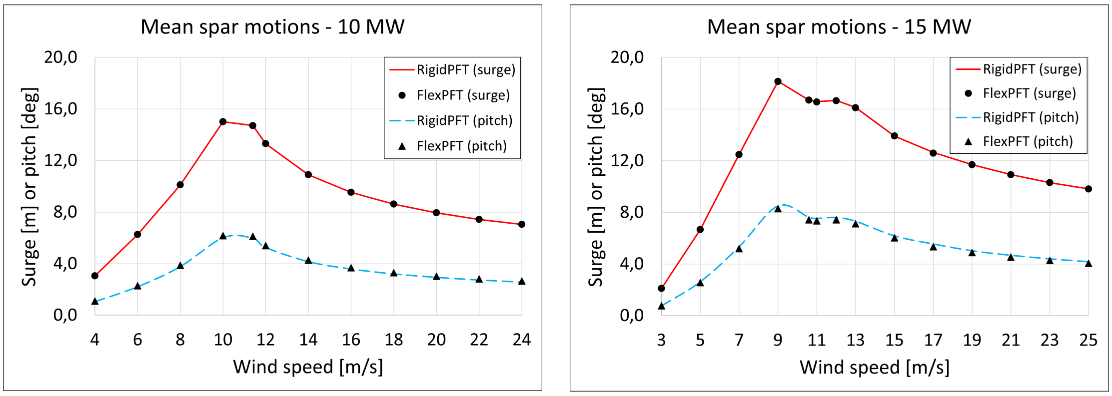

(a) 10 MW (b) 15 MW

Figure 25: Mean spar motions in surge and pitch

5.5 Decay Tests

Decay tests was performed to determine the natural periods and damping coefficients. In addition, the natural period in pitch bending moment at the tower base was found from pitch decay and compared to the rotor frequencies (1p and 3p). For the decay tests, the turbine was parked with its blades feathered. Since the BEM method is not suited for a parked turbine, the induction calculation was turned off for the decay tests.

In SIMA, the decay tests are carried out by applying an increasing load (ramp force/moment) followed by a constant load (constant force/moment) which after some time is released. The significant wave height is set to 0.001 m, the peak period is 20 s, and the wind speed is 0.01 m/s to avoid interference with the results. When the forces are gone, the structure will gradually go back to its equilibrium position. By utilizing the results, the natural period and damping coefficients for each motion can be determined (the procedure is shown in Section 3.3.3).

5.5.1 Natural Periods

The natural periods for all the models are shown in Figure 26 below, including the results from Hegseth et al. [17] for reference. Since the spars are symmetrical in the xy-plane, only surge, heave, pitch and yaw are presented (sway and roll are less relevant, and also equal to surge and pitch, respectively).

All the models have natural surge periods well outside the frequency of wave excitations. $T_{n,1}$ is linked to added mass, which is calculated differently for the respective wave calculation method. The added mass in surge (A_{11}) is larger for the ME models, and this results in a larger natural period. The difference is small, and all of the models are close to the $T_{n,1}$ presented by Hegseth et al. [17]. $T_{n,1}$ is larger for the 15 MW spars since they have a larger A_{11}.

The natural period in heave ($T_{n,3}$) is identical for all the 10 MW models (and similar to Hegseth et al.). Heave natural period is related to hydrostatic stiffness (C_{33}) and added mass (A_{33}). C_{33} is calculated in HydroD (and is similar to the theoretical value in Section 3.2.2) and is given as input to the rigid models (since ME does not provide this), while the flexible models calculate C_{33} based on RIFLEX formulation. Based on the similarity, the flexible models most likely calculate a close to identical C_{33}. This was also verified by studying the static displacement in the heave decay tests, which displayed a displacement of 2.3 m for all 10 MW models for the same applied force of 3 MN. A_{33} is calculated in HydroD for RigidPFT. This value is given as input at the bottom of the ME models since it is considered an end effect for a classical spar. This is a simplification since the spar used does not have a constant diameter. In reality, the added mass will be distributed along the spar [34]. A_{33} is calculated by stepwise integration using WAMIT for FlexPFT, but it is identical to HydroD (Figure 13). $T_{n,3}$ is also identical for all 15 MW models for the same reasons explained above.

The natural period in pitch ($T_{n,5}$) varies more than in heave. It is also related to hydrostatic stiffness (C_{55}) and added mass (A_{55}). When HydroD calculates C_{55} for the spar in HydroD, no concrete ballast is present and therefore underestimates the value. For this reason, it is calculated with concrete ballast for the rigid models based on the same theory (see Section 3.2.2). The flexible models use RIFLEX formulation, but again it seems to be similar. The ME models have slightly larger $T_{n,5}$ compared to the PFT models, which is related to the larger added mass (Figure 14).

None of the models provide hydrostatic stiffness in yaw by themselves. This lead to numerical instability, and for practical reasons a hydrostatic stiffness coefficient in yaw (C_{66} = 150 MNm) was included in all the models (see Section 4.6). Judging from the results, it becomes evident that C_{66} affects the rigid and flexible models differently. The rigid models have twice as high natural periods in yaw (see Figure 50). Since the models have the same C_{66}, it is likely that the inertia of the ballast is not included in the flexible models. Inspection of the irregular waves tests were made to ensure that the yaw motions were small for all models and should not pollute the results.

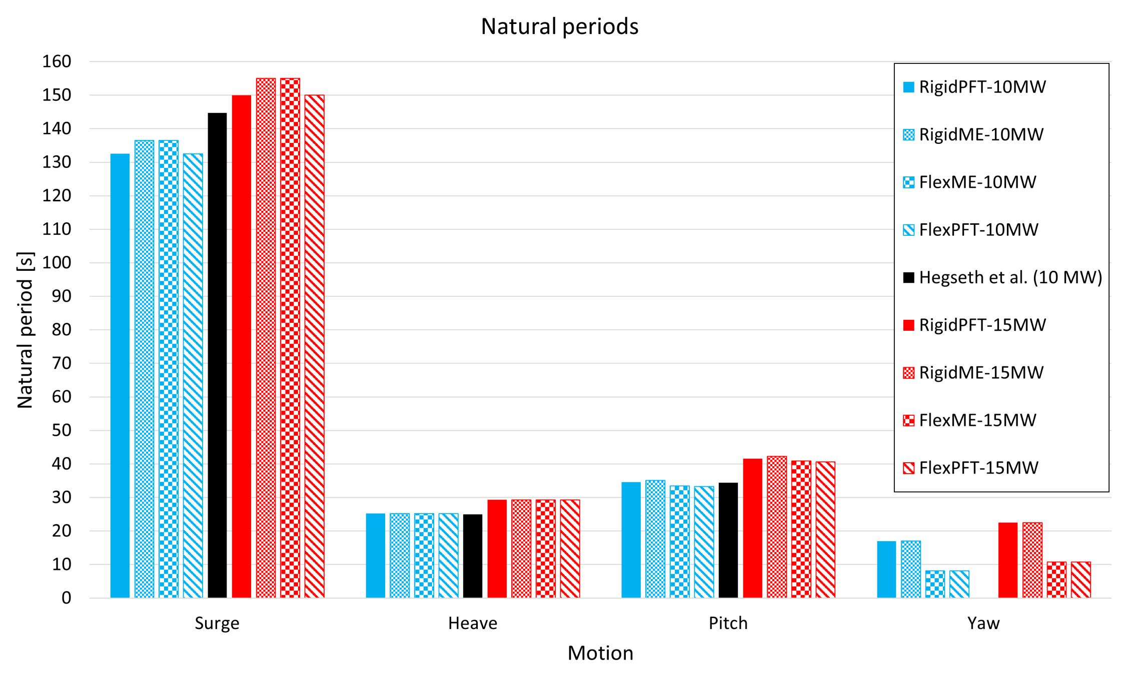

Figure 26: Natural periods in seconds

5.5.2 Damping Coefficients

The linearized linear and quadratic damping coefficients are presented in Figure 27 and 28, respectively. Comparisons between the 10 and 15 MW spars are not made since the coefficients depend on the spar mass and natural periods.

The linear damping coefficients in surge and heave show good agreement for the 10 MW spars. In pitch and yaw, b_1 is larger for the flexible models. This could be related to the mass distribution of the spars. Since the ballast was included in the flexible models by assigning mass to the bottom sections, it is likely that the inertia of the ballast was not included. The 15 MW spars exhibit similar b_1 in surge, but slightly larger values for the flexible models in heave. b_1 is also larger for the flexible spars in pitch and yaw, which also could be related to the ballast inertia.

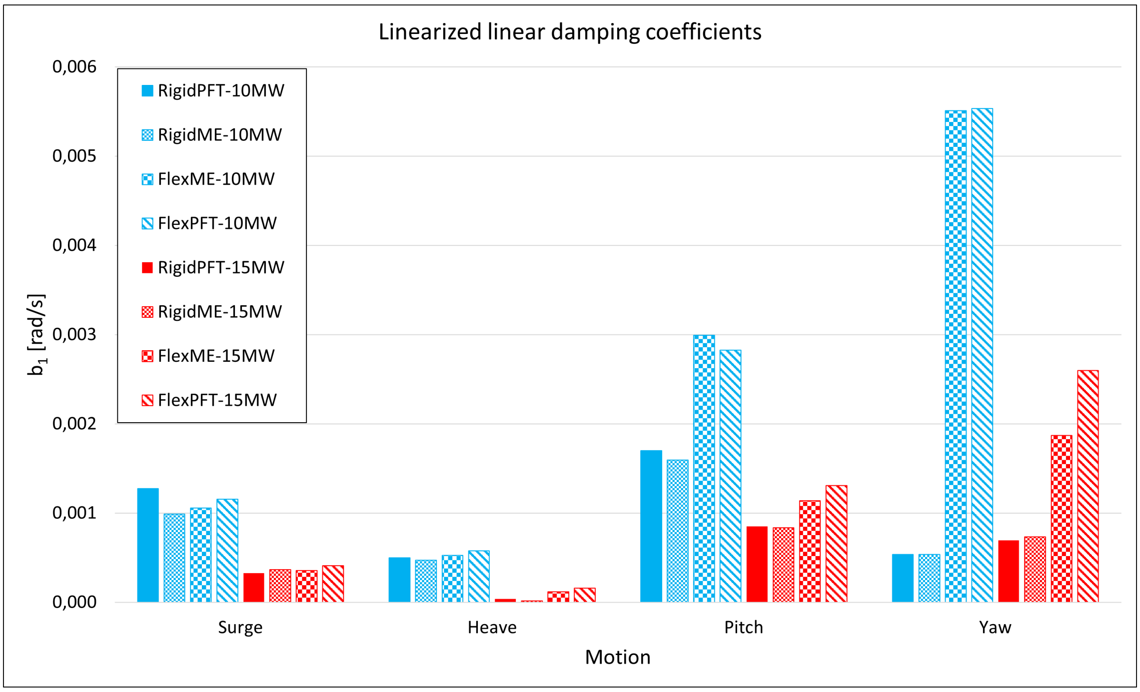

Figure 27: Linearized linear damping coefficients

The quadratic damping coefficients display similar results in surge, heave and pitch between the 10 MW models. This is also the case for the 15 MW models. b_2 in yaw is slightly larger for the flexible models.

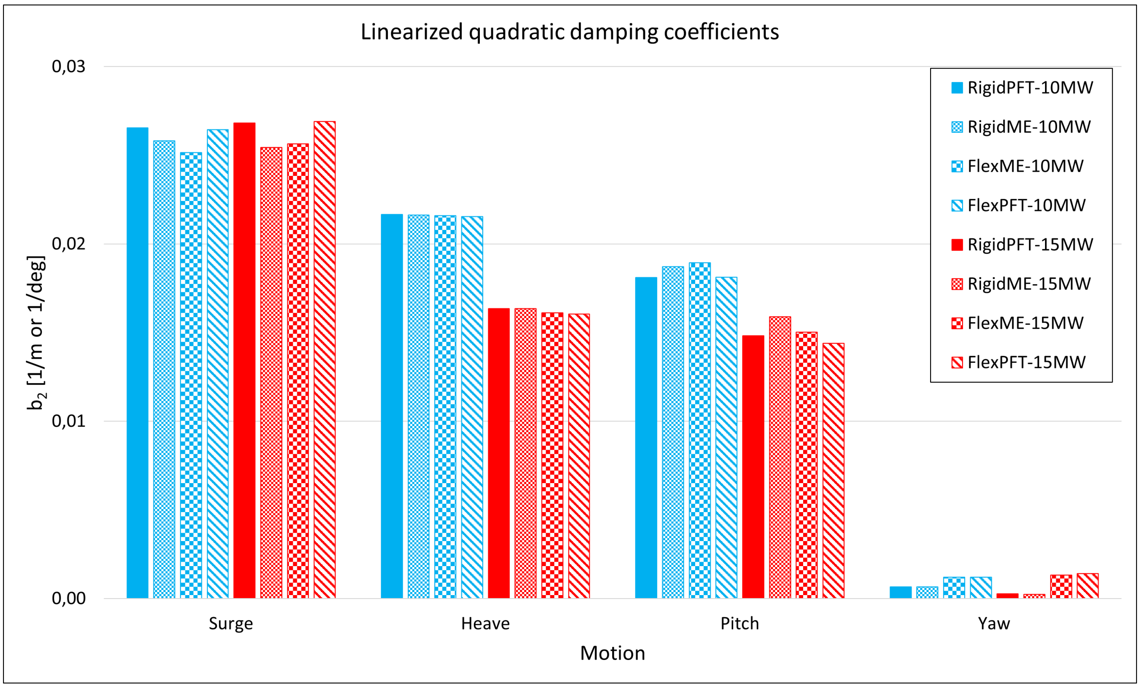

Figure 28: Linearized quadratic damping coefficients

5.5.3 Tower base fore-aft bending natural period

By using the result for the tower base fore-aft bending moment from the pitch decay test, the natural bending period in pitch can be found. This can be transformed into natural angular frequency, and then compared to the 1p and 3p rotor frequencies. These are found from taking the lowest and highest rotor speeds that the turbine will experience based on the constant wind tests.

Figure 29 shows that all the 10 MW models have bending natural angular frequencies well beyond the 3p frequency, i.e. the stiff-stiff design region. Thus, the 10 MW spars should not expericence resonance from rotor excitations. The flexible models exhibit smaller natural angular frequencies. The upscaled models come closer to the 3p frequency (see Figure 30). This can be explained by the 15 MW models being longer and the increase of steel weight in the hull being minimized in the upscaling procedure (36% increase). Natural angular frequencies are more comparable for the 15 MW models, and FlexPFT actually has a larger value than RigidME.

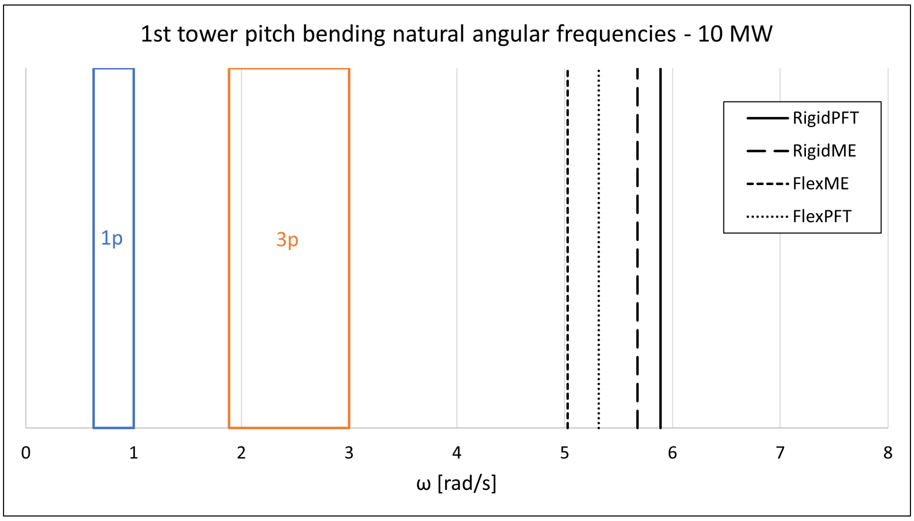

Figure 29: 1st tower pitch bending natural angular frequencies for 10 MW towers

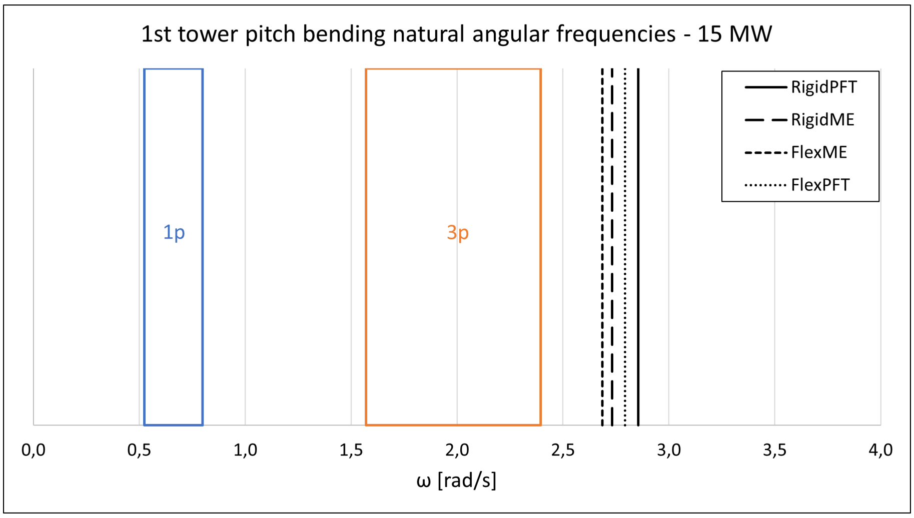

Figure 30: 1st tower pitch bending natural angular frequencies for 15 MW towers

5.6 Regular Waves

Regular waves tests were used to create RAOs for motions (surge, heave and pitch), bending moment and stress along the towers and flexible spars (explained in Section 3.5). The RAOs from HydroD, which not included the concrete ballast and therefore have different restoring forces and moment of inertia, are included for reference (referred to as "HydroD" in the results). It has the correct mass, but uses seawater for ballasting which gives a different mass distribution (compared to if concrete had been used). Additionally, the RAOs from HydroD were used along with the correct restoring forces and mass distribution to calculate it with the correct values (referred to as "Calculations" in the results). The same wave height ($H = 1$ m) and a range of wave periods (T = 3-15 s) were used. The turbine is parked, induction calculation is turned off, and the wind speed is 0.01 m/s.

5.6.1 Surge RAO

The RAO in surge for all 10 MW models, including calculated and HydroD results, is presented in Figure 31. For low wave frequencies, the four models exhibit almost identical results (ω = 0.4-1 rad/s). As the frequencies become larger, the ME models have larger responses than the PFT models (w = 1-2.1 rad/s). The reason for this is that the excitations are larger for the ME models in this frequency region (see Figure 9 in Section 5.1). The calculated values underestimate the response compared to the models, while the HydroD results overestimate it. It is not expected that the reference values should be equal to the models, but are included to verify that the models are in the same area.

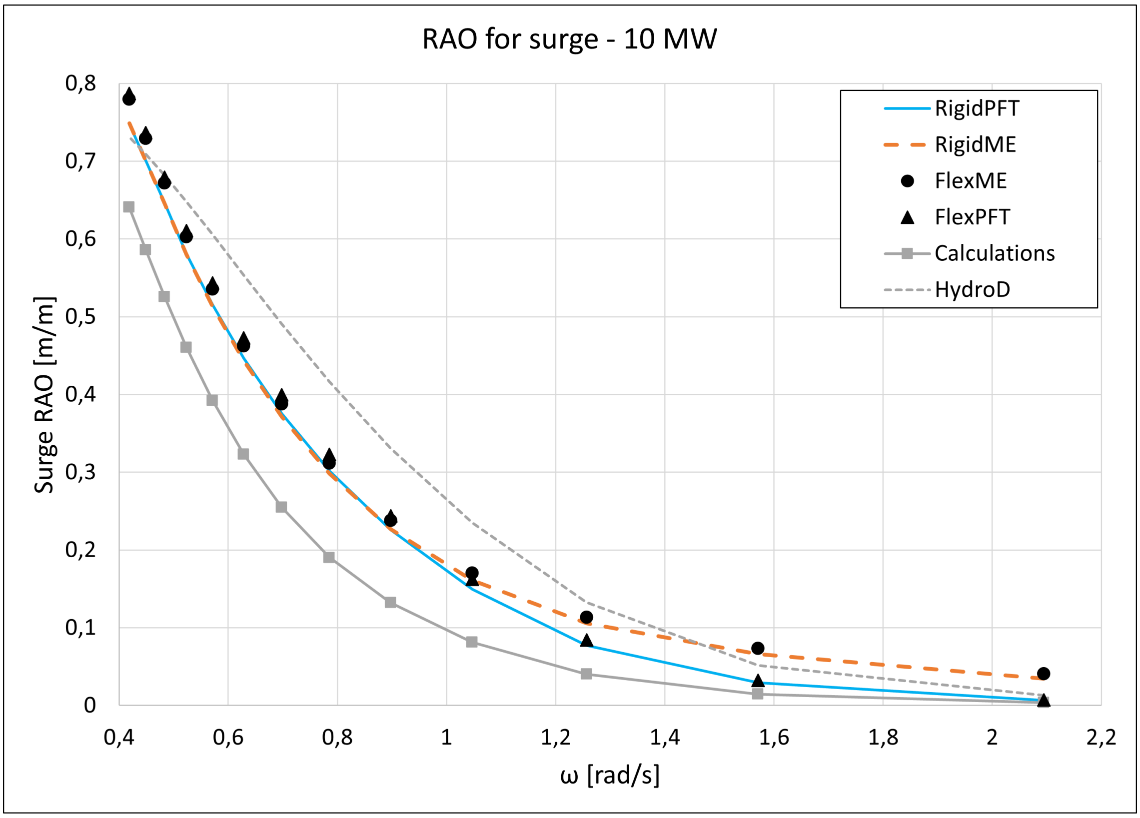

Figure 31: RAO in surge for 10 MW spars

The results for the 15 MW spars are shown in Figure 32, and the same conclusions as for the 10 MW spars are representative here. The only difference is that HydroD is way off here, which emphasizes the importance of applying the correct mass distribution for the models.

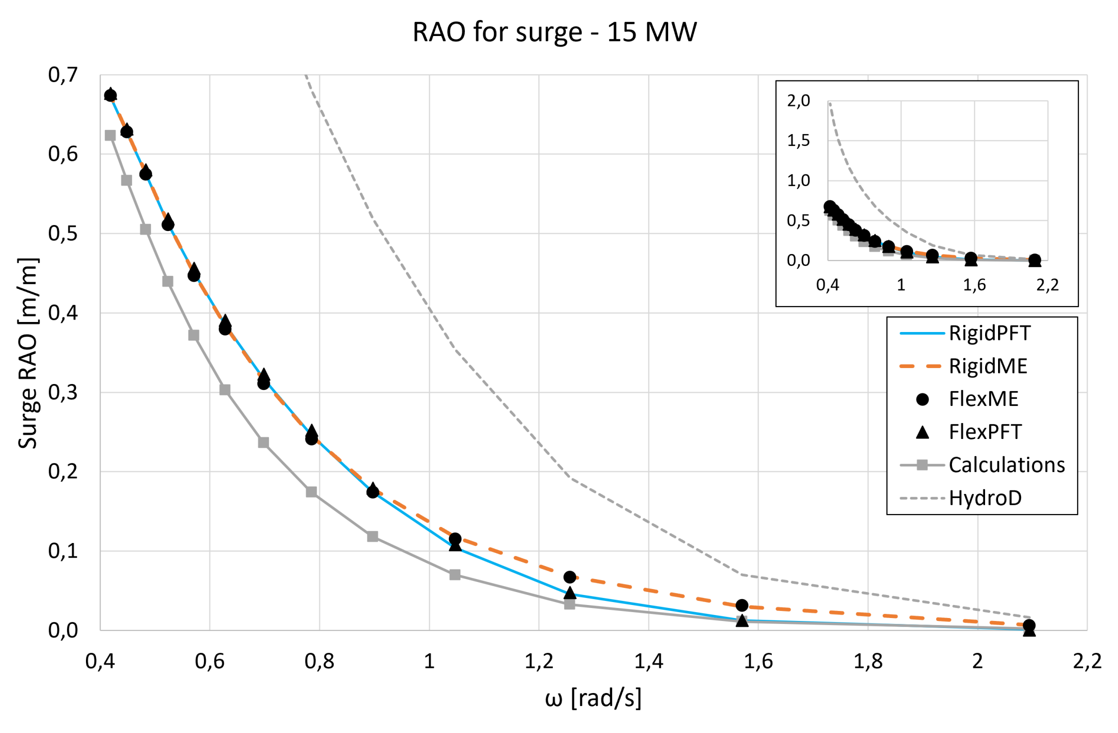

Figure 32: RAO in surge for 15 MW spars

5.6.2 Heave RAO

In heave, all the models have a similar response (Figure 33) with the exception of FlexME. Since the deviation is small and the heave motions of the spars are small in the later tests, this is not considered an issue. The HydroD results agree well with the models for heave, which is expected since C_{33} is not affected by the mass distribution (see Equation 16 in Section 3.2.2).

The heave RAOs for the 15 MW spars are shown in Figure 34. The models agree well, but the FlexME-15MW deviates more here (especially for low frequencies).

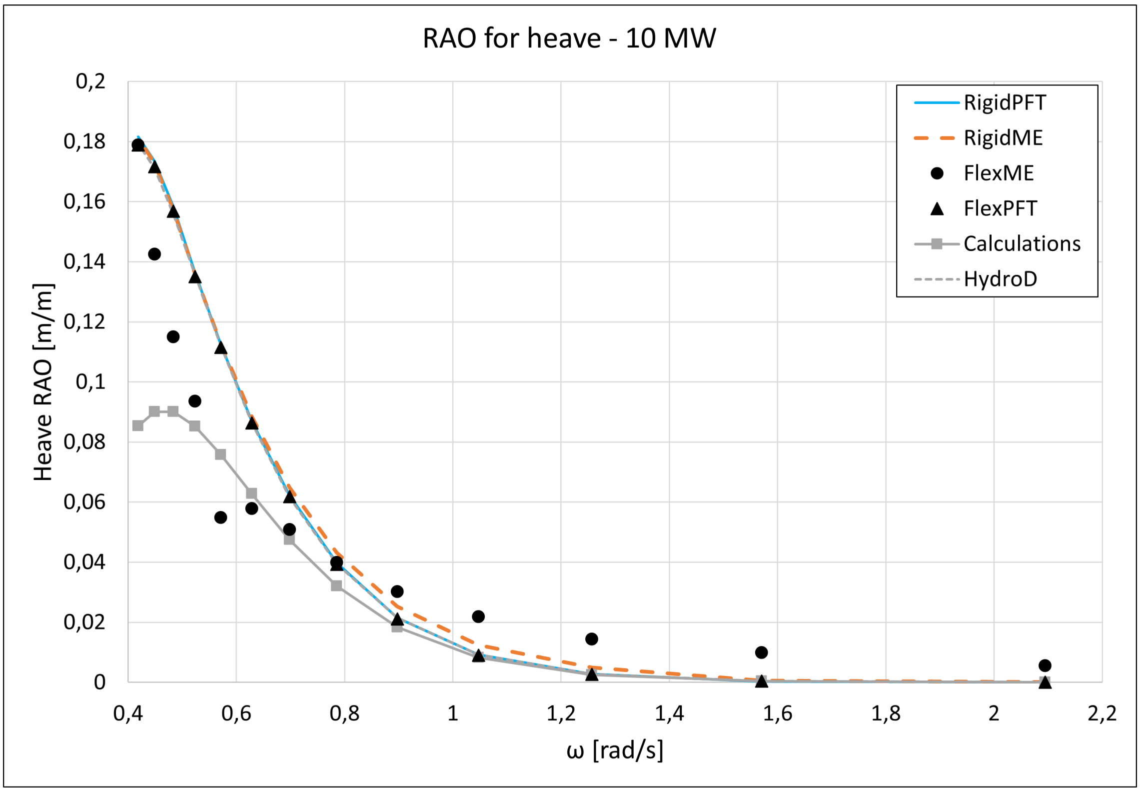

Figure 33: RAO in heave for 10 MW spars

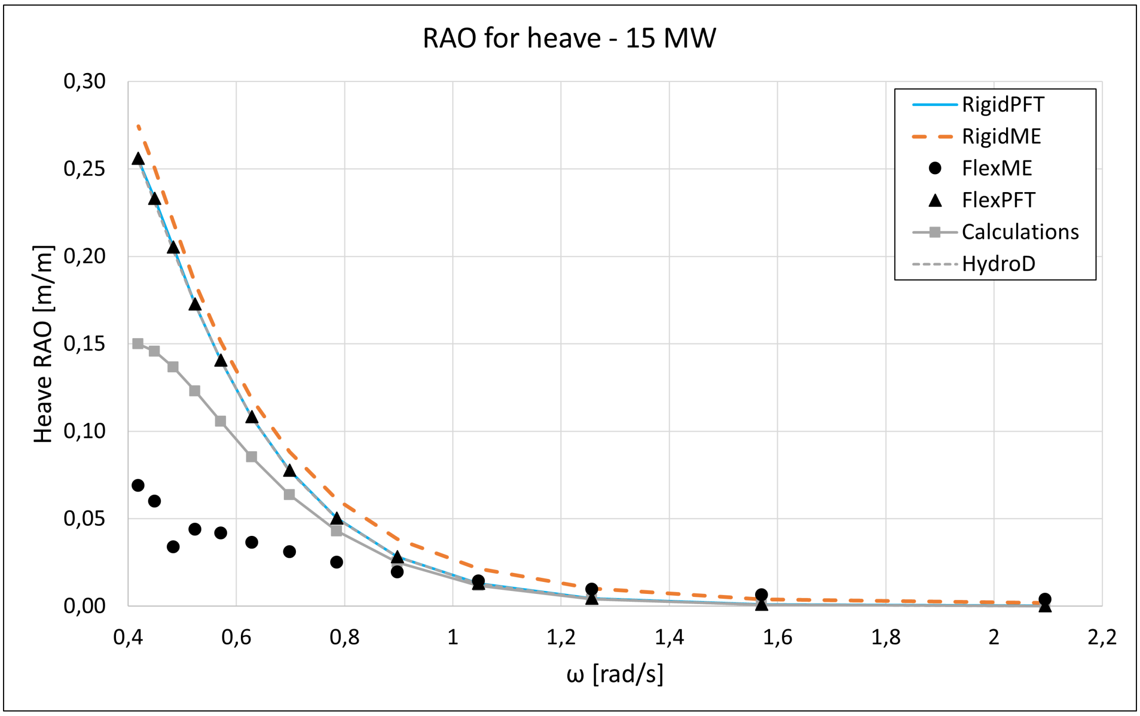

Figure 34: RAO in heave for 15 MW spars

5.6.3 Pitch RAO

For pitch, the flexible 10 MW models exhibit a slightly higher response in the low frequency region (Figure 35). For the larger frequencies, the ME models have the largest response, similar to the RAO for surge. This is due to the larger excitations in pitch for the ME-models (see Figure 11 in Section 5.1). The HydroD results are out of phase with the models due to the difference in mass distribution. C_{55} is smaller in the HydroD results.

The RAO for the 15 MW spars does not show dissimilarity for low frequencies (see Figure 36), but the ME models still have larger values for high frequencies. The HydroD response is much larger than the models, but also the calculated values are a bit off for low frequencies.

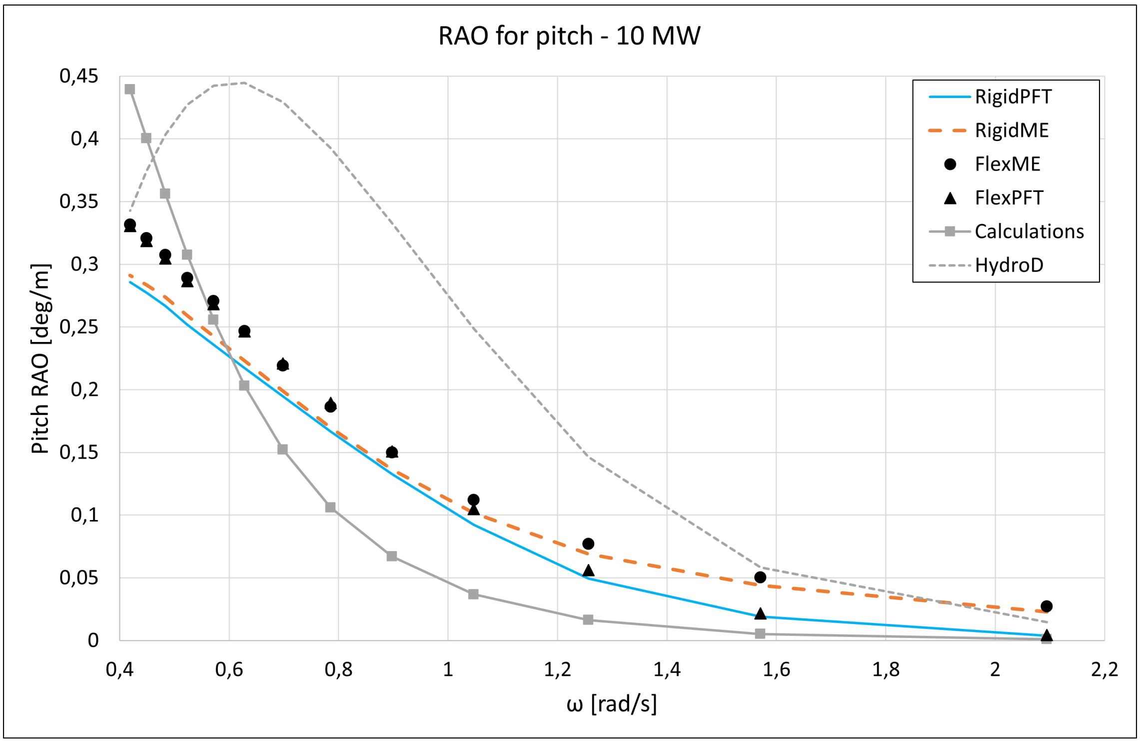

Figure 35: RAO in pitch for 10 MW spars

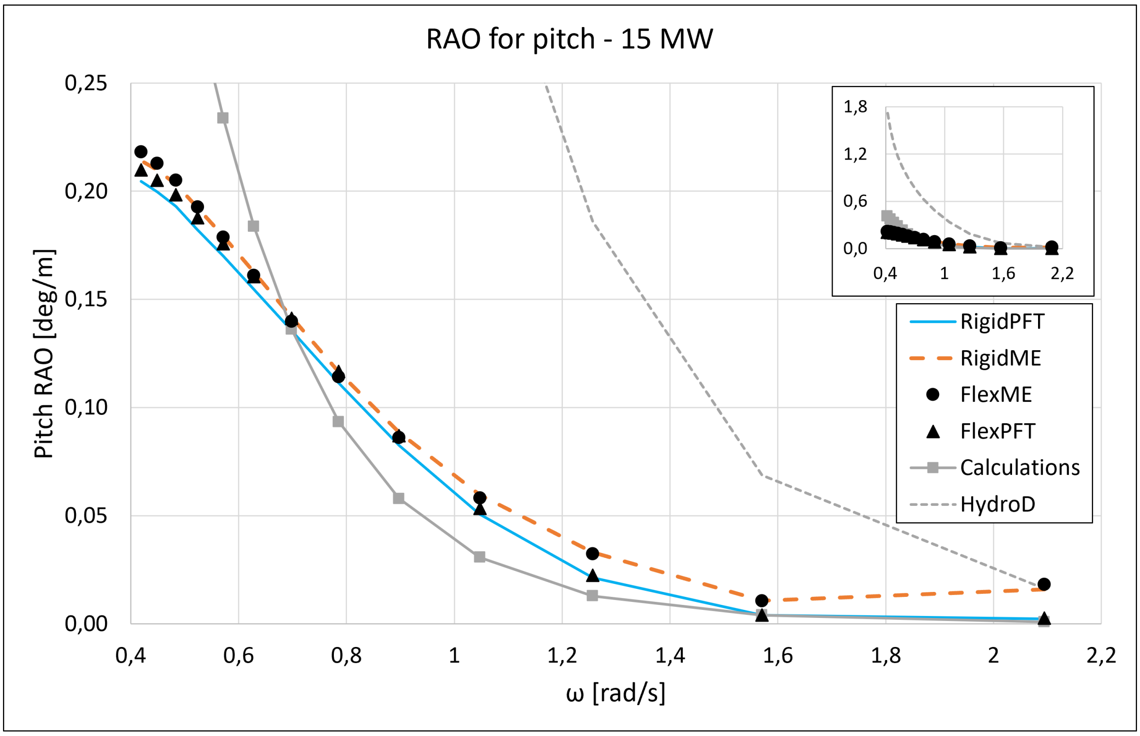

Figure 36: RAO in pitch for 15 MW spars

5.6.4 Bending Moment RAO - Towers

The bending moment RAO for the 10 MW towers are presented in Figure 37. There is a distinct difference between the PFT and ME models for high frequencies (starting from $\omega = 1$ rad/s, but more prominent from 1.2-2.1 rad/s). While the bending moment for the PFT towers goes towards zero (or at least rapidly decrease), the bending moment for the ME towers slightly increases. This leads to a significant difference in bending moment between the two wave load modeling methods for high frequencies, resulting in larger fatigue damage for the ME models at these frequencies. Also, note that the flexible models estimate slightly higher bending moments. The 15 MW towers exhibit similar results, but an even larger distinction between ME and PFT for high frequencies (see Appendix B).

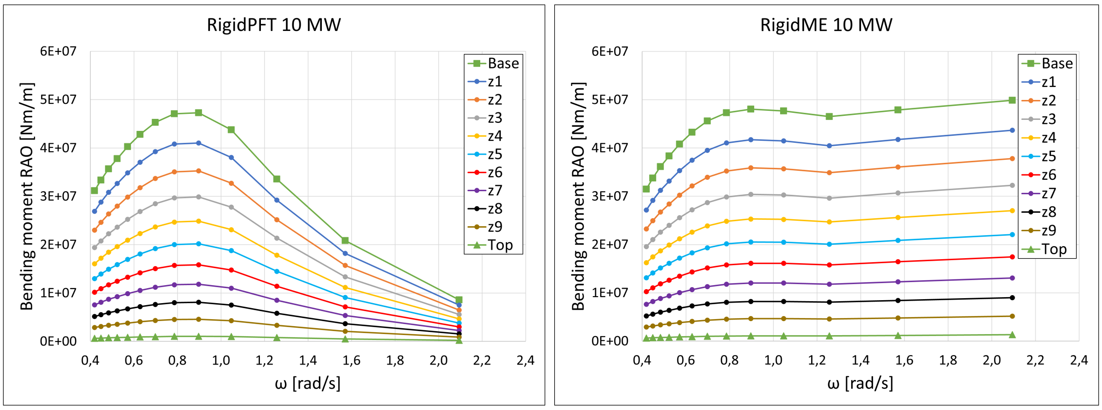

(a) RigidPFT 10 MW

(b) RigidME 10 MW

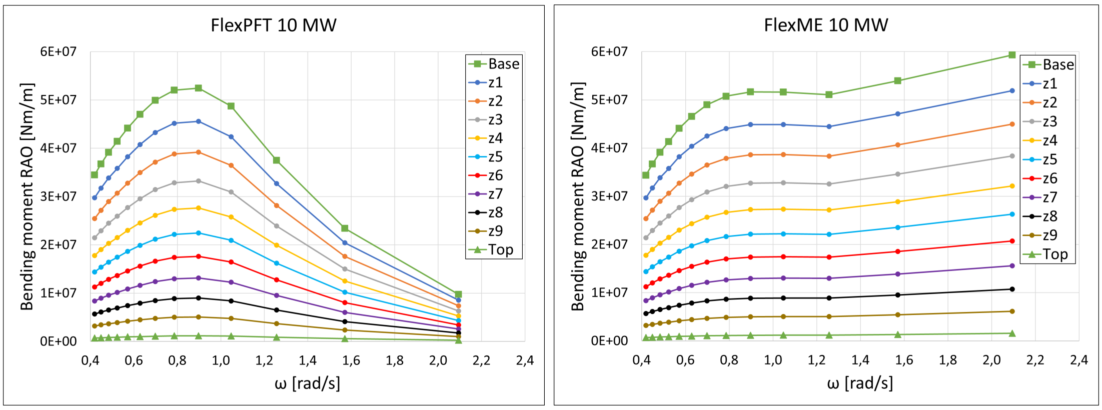

(c) FlexPFT 10 MW

(d) FlexME 10 MW

Figure 37: Bending moment RAO for 10 MW towers

5.6.5 Bending Moment RAO - Flexible Spars

Figure 38 presents the bending moment RAO for the flexible 10 MW spars, where six cross-sections along the spar is included. The largest response is at the top of the spars (z = 10 m, indicated by green lines with squares), where it is connected to the tower. The response is gradually declining when moving further away from the top. The deviation between ME and PFT for high frequencies is similar to that of the towers, which is that the ME models have a much larger response for those frequencies. The results for the 15 MW spars are similar (Figure 39), but the difference between the wave load models is even larger. This indicates that upscaling the spar increase the deviation in bending moment between ME and PFT models for large wave frequencies.

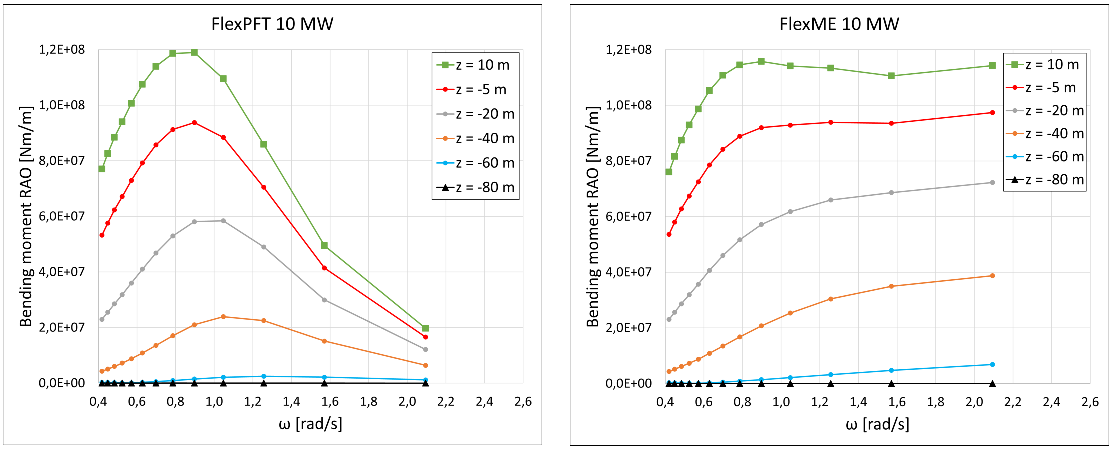

(a) FlexPFT (b) FlexME

Figure 38: Bending moment RAO for 10 MW spars

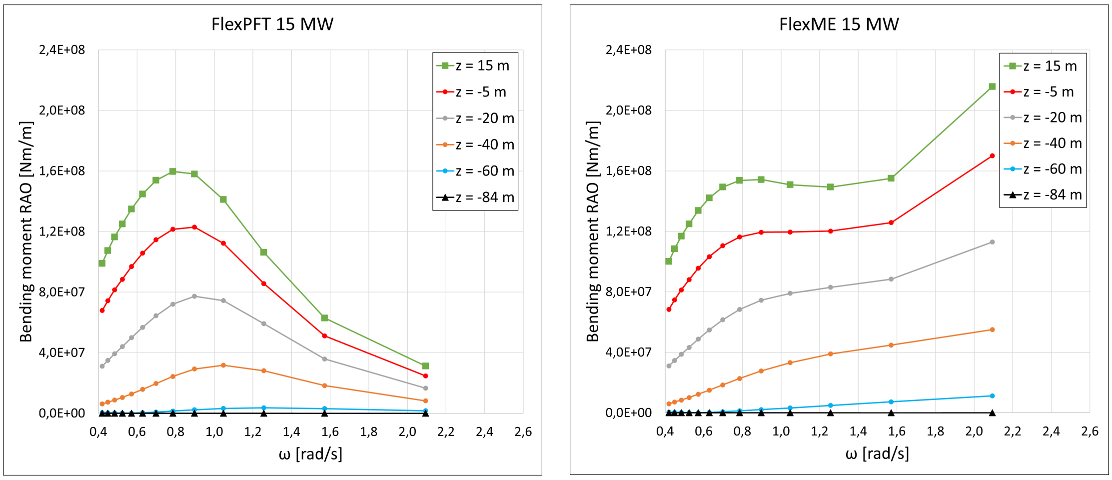

(a) FlexPFT-15MW (b) FlexME-15MW

Figure 39: Bending moment RAO for 15 MW spars

5.6.6 Bending Stress RAO

The bending stress RAO for the 10 MW towers on rigid spars is shown in Figure 40 below. Only the results for three wave periods are included, since they are sufficient in order to explain the behavior. ME and PFT show good agreement for $T = 15$ s, and the bending stress response will increase towards $T = 7$ s in a similar fashion for both models. This is where RigidPFT's tower has its highest response, before the response decreases with lower wave periods towards $T = 3$ s. In contrast to this, the bending stress response for RigidME's tower will only decrease slightly for wave periods of $T =$ 5-6 s. The response will then increase when moving towards $T = 3$ s, where RigidME's tower has its highest response. This indicates that the ME models will estimate significantly larger bending stresses for low wave periods.

On another note, the bending stress along the 10 MW towers is almost constant (disregarding the top). The various sections of the tower appear to have been modeled with the same maximum allowable stress. This reflects that the tower is an optimized design from Hegseth et al. (see Section 4.4). The diameters and thicknesses used for the tower are shown to the right in Figure 40, which displays the increase in diameter above the base. As a result, the fatigue damage should be evenly distributed along the tower.

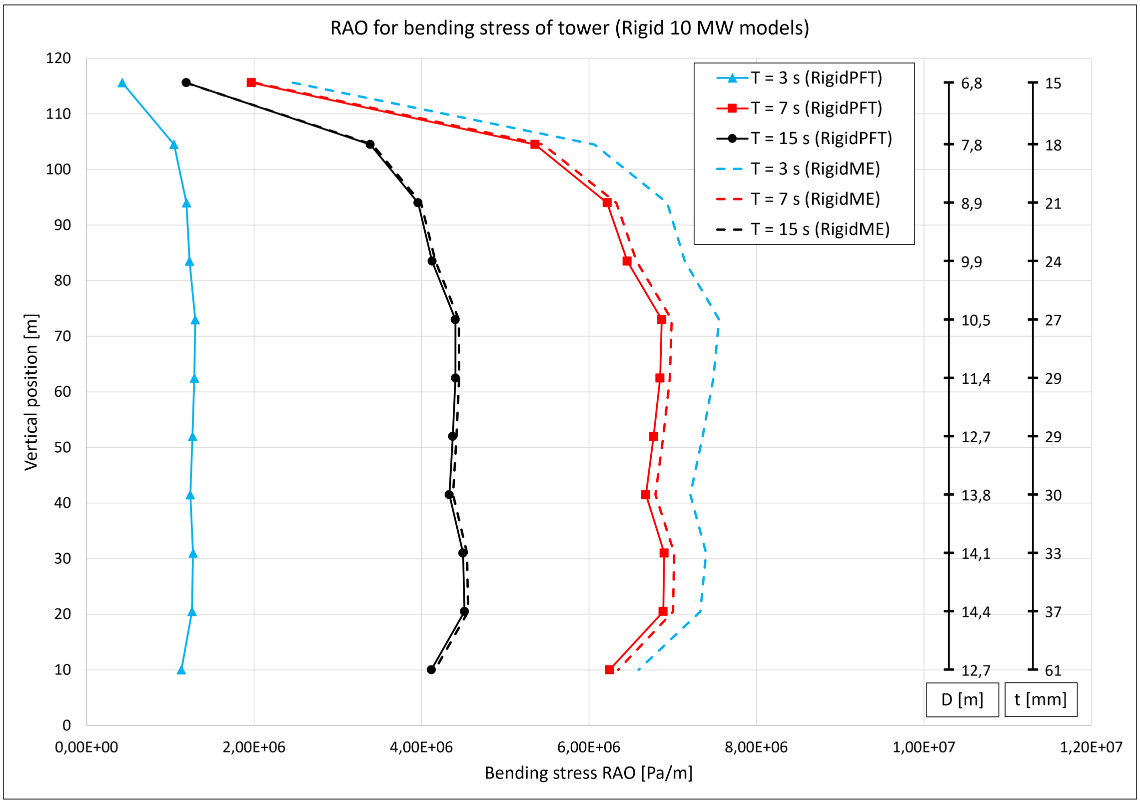

Figure 40: Bending stress RAO for tower of rigid 10 MW models

The 15 MW towers on rigid spars displays the same trend as the 10 MW towers (see Figure 41), but the RigidME-15MW tower deviates even more for $T = 3$ s. The larger deviation for low periods is not linked to the different towers used, but connected to the larger bending moment deviation that the 15 MW ME models experience compared to the 10 MW ME models. The 15 MW tower exhibits a different stress distribution along the tower. The stress is small at the top, then increases towards the cross-section at approximately $z = 52$ m (where it is largest). It drops for $z = 41$ m before it increases towards the base at $z = 15$ m. Although this is a more conventional tower, the largest stress is not at the base. Based on the results, the fatigue damage should be larger along the middle of the tower.

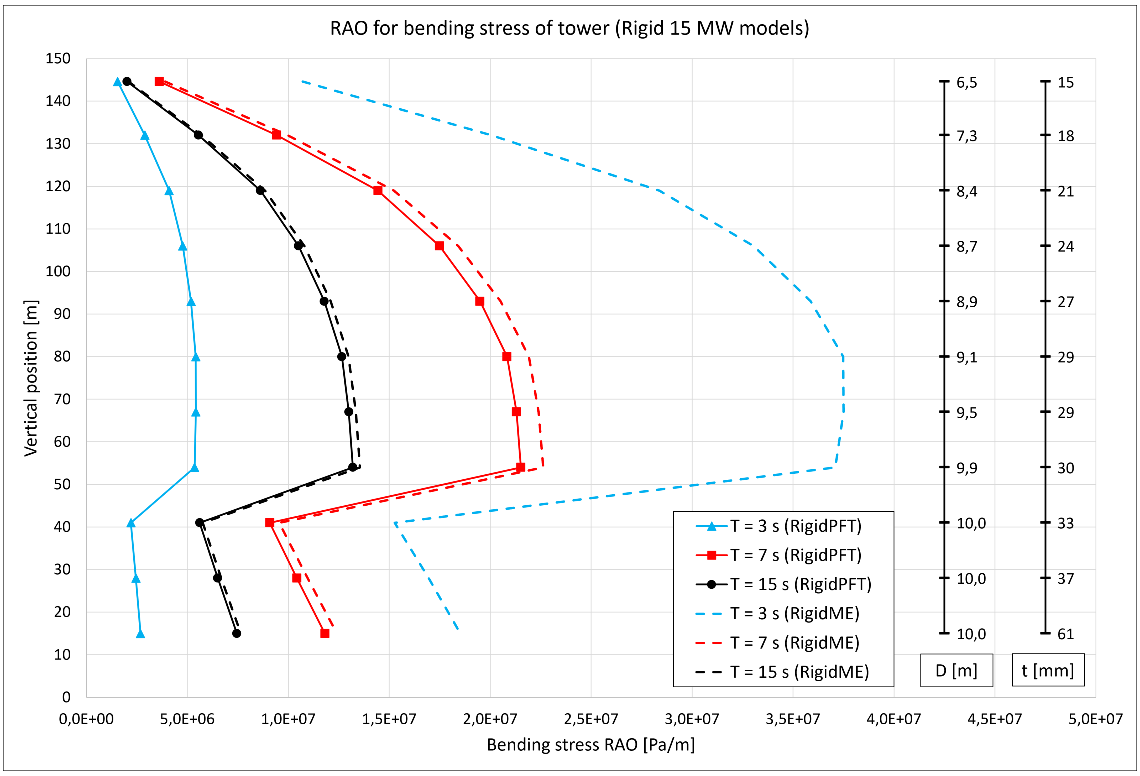

Figure 41: Bending stress RAO for tower of rigid 15 MW models

The bending stress RAO for 10 MW flexible spars with towers is presented in Figure 42. The towers are consistent with the 10 MW towers on the rigid spars. The stress along the spars decreases when moving away from the top ($z = 10$ m), except for a small increase due to the drop in diameter and thickness at $z =$ -32 m. The flexible spars exhibit similar results to the towers, meaning the ME model is larger for low wave periods.

For the 15 MW flexible spars, the maximum stress at the middle of the tower is actually larger than the stress at the top of the spar for $T = 3$ s (Figure 43). This is in contrast to the 10 MW flexible spars. Apart from this, the variation between wave periods corresponds to the previous results. The towers are in line with the 15 MW towers on rigid spars.

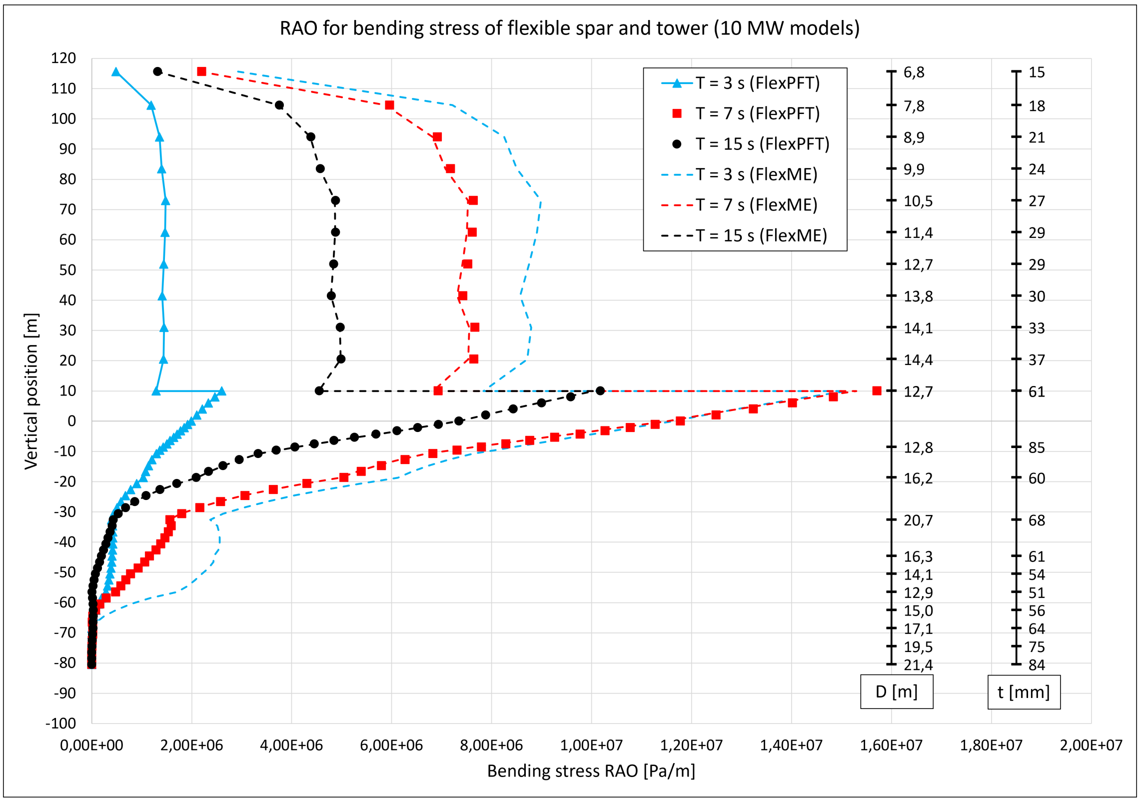

Figure 42: Bending stress RAO for flexible 10 MW models with towers

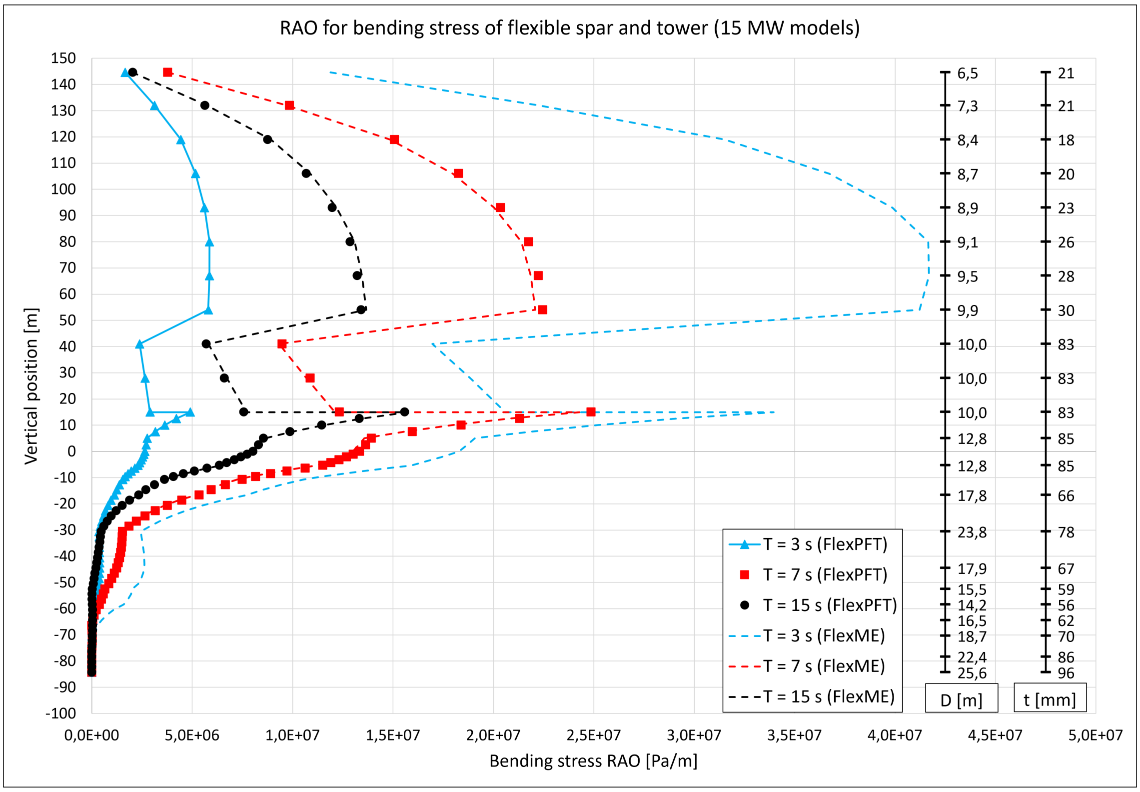

Figure 43: Bending stress RAO for flexible 15 MW models with towers

5.7 Irregular Waves

The models are tested for irregular waves with turbulent wind for 15 sea conditions. The purpose is to evaluate the fatigue damage (due to axial stress) and the power spectra. The most interesting aspect is to investigate how elasticity and wave load modeling affects the fatigue for different sea conditions. Power production is not interesting for this thesis. As a result, the probability of the sea conditions was not included.

The environmental data in Table 12 is based on the statistics from Li et al. ([25], site 14), but significant wave height (H_s) and peak period (T_p) are chosen to be more representative for this project by covering more wave periods. This means that H_s and T_p for a given sea condition is not necessarily the most probable value for the given wind velocity (thus, the word "hypothetical" is used even though it is based on a real location in the North Sea). The reason for this choice is that the smaller wave periods are where the PFT and ME models differ the most. Hence, it is the most interesting area to explore.

Condition No.	**H$_s$ [m]**	**T$_p$ [s]**	**U$_w$ [m/s]**		**Turbulence Intensity [%]**	
			10 MW	**15 MW**	**10 MW**	**15 MW**
1	0.75	4	2	2.066	31.1	30.1
2	1.25	5	4	4.132	18.5	18.1
3	2.25	7	4	4.132	18.5	18.1
4	1.50	5	6	6.198	15.1	14.8
5	2.50	8	6	6.198	15.1	14.8
6	1.50	8	8	8.264	13.6	13.4
7	2.50	10	8	8.264	13.6	13.4
8	2.00	10	10	10.329	12.9	12.7
9	4.00	14	10	10.329	12.9	12.7
10	3.00	12	12	12.395	12.5	12.4
11	2.00	10	14	14.461	12.3	12.1
12	3.50	12	14	14.461	12.3	12.1
13	3.00	10	18	18.593	12.2	12.0
14	5.50	12	18	18.593	12.2	12.0
15	5.00	10	20	20.659	12.2	12.0

Table 12: Environmental conditions for the hypothetical location

5.7.1 Fatigue Damage on 10 MW Towers

The 1-hr fatigue damage along the 10 MW towers are shown in Figure 44, 45, 46 and 47 with respect to the vertical position, and the results for all the 15 sea conditions are given. The damage at the top of the tower is inconsistent with the small bending moment and stress showed earlier, and should be neglected or at least be considered questionable. It could be that the method used for calculating the fatigue damage (see Section 3.8) is not representative for the small thicknesses at the top ($t < 25$ mm), since they are smaller than the reference thickness of 25 mm. Notice that the damage is similar for the other cross-sections of the tower (disregarding the top), which was expected based on the bending stress distribution shown earlier.

For conditions 1 to 5, the damage is largest for FlexME, followed by RigidME. RigidPFT and FlexPFT both have relatively smaller fatigue damage for these conditions, where the wave periods are small. This is in agreement with the larger bending stress the ME models experience for low wave periods. The bending stress results also revealed a higher response for FlexME compared to RigidME for low T, which explains the difference in damage between the two ME models. Observe that the most prominent variance between FlexME and RigidME is for condition 4, which is also where FlexPFT and RigidPFT vary the most. This could be related to elasticity. The distinctions between the models are less obvious for the other conditions, and some of them display close to similar results for all models (i.e. condition 6, 8-9 and 11-12).

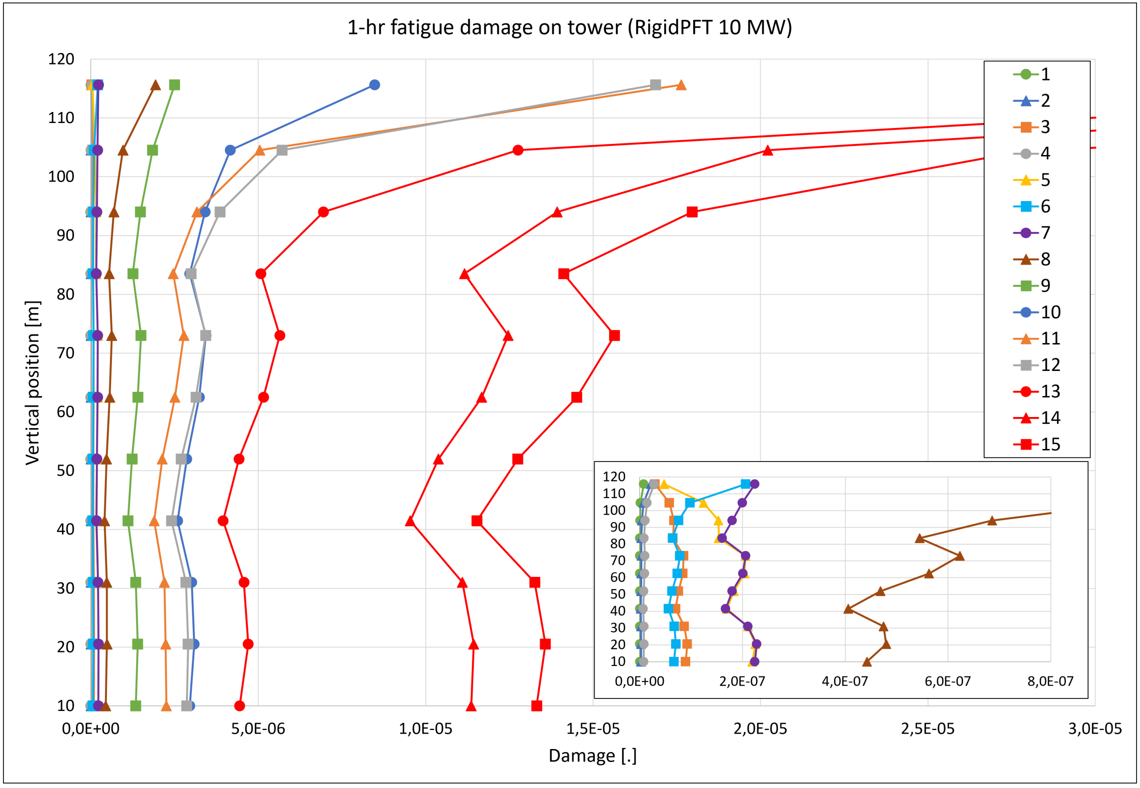

Figure 44: 1-hr fatigue damage for RigidPFT-10MW tower (Condition 1-15 in legend)

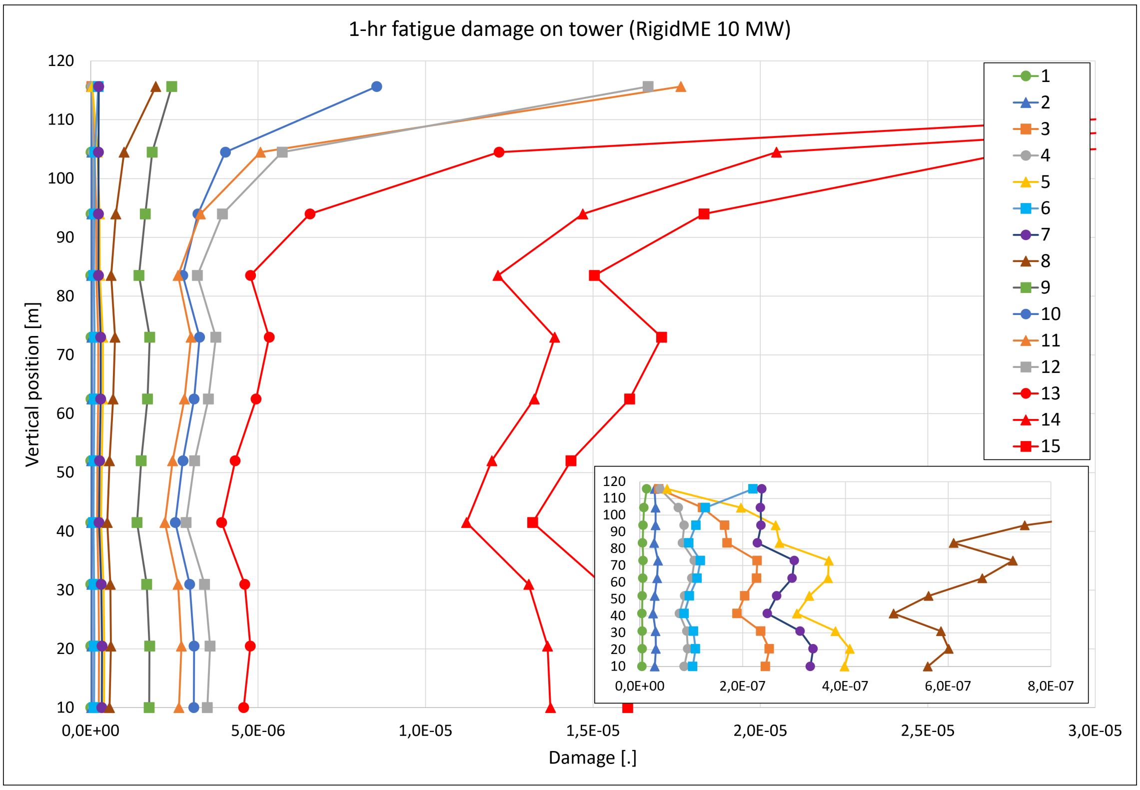

Figure 45: 1-hr fatigue damage for RigidME-10MW tower (Condition 1-15 in legend)

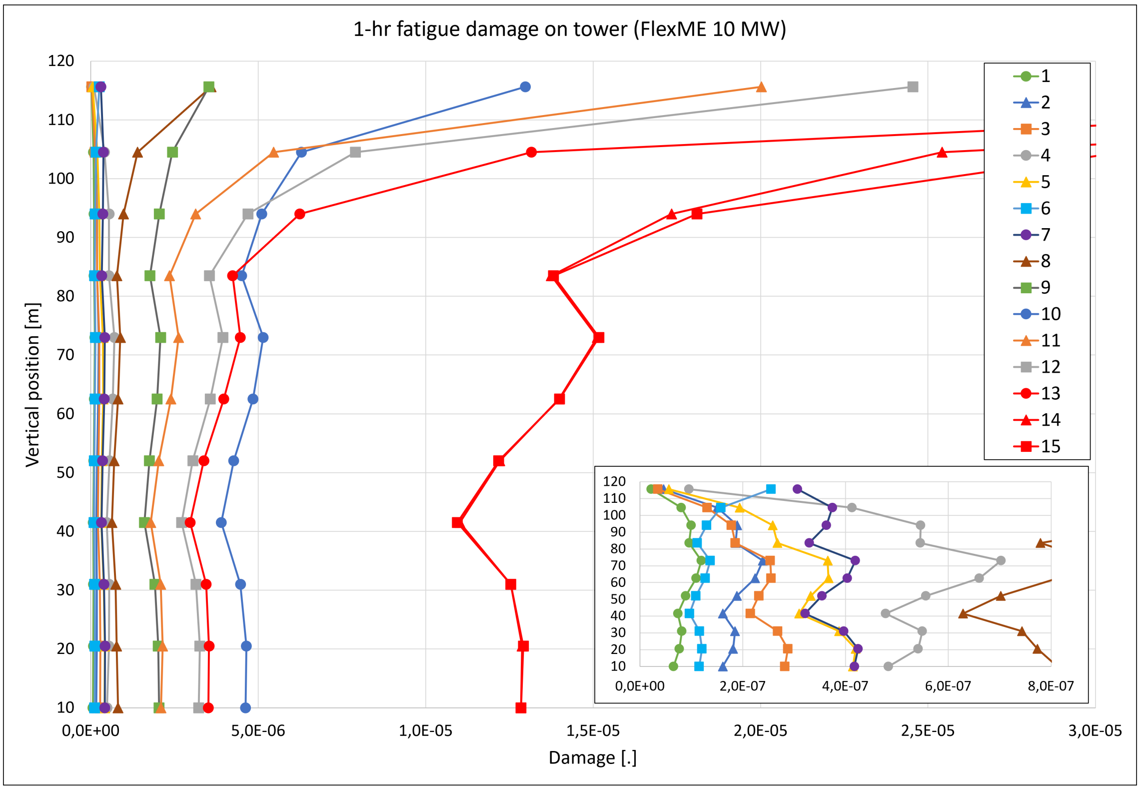

Figure 46: 1-hr fatigue damage for FlexME-10MW tower (Condition 1-15 in legend)

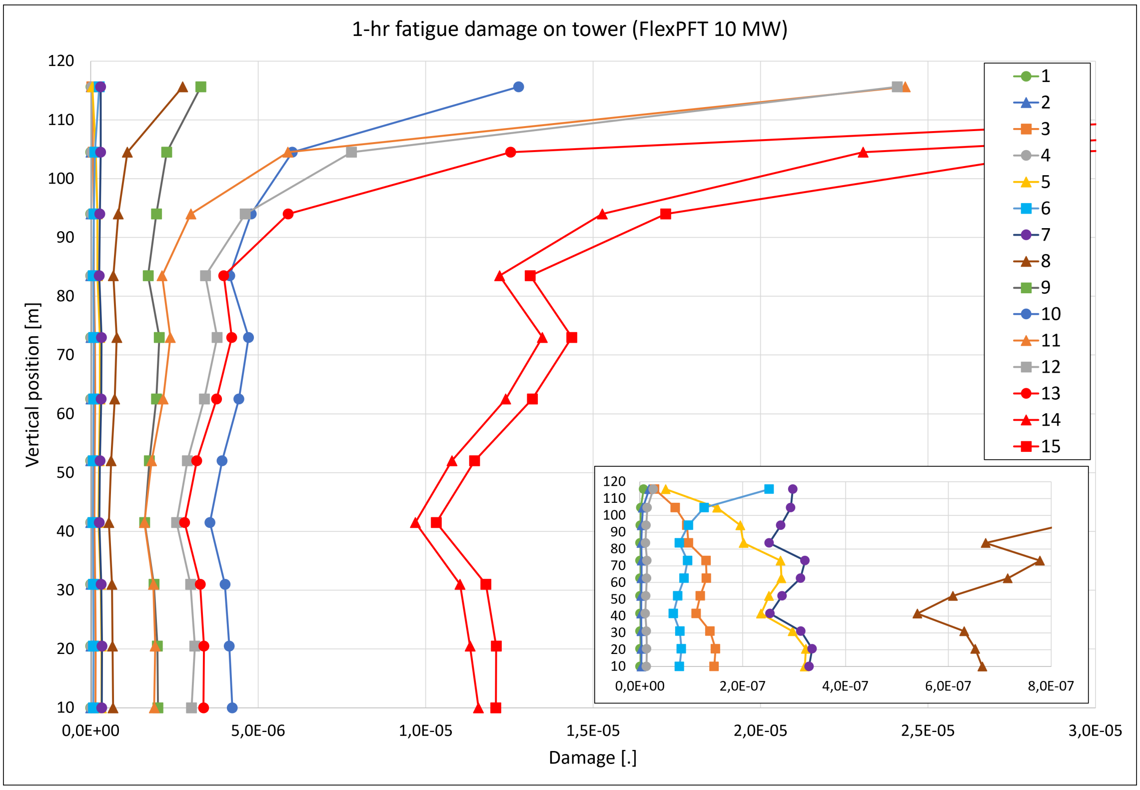

Figure 47: 1-hr fatigue damage for FlexPFT-10MW tower (Condition 1-15 in legend)

5.7.2 Fatigue Damage on 15 MW Towers

The results for the 15 MW towers are given in Figure 48, 49, 50 and 51. Unlike the 10 MW towers, the fatigue damage is low at the top section here. The thickness is larger at the top sections compared to the 10 MW towers, which could explain why it exhibits a more expected damage there. The damage is consistent with the bending stress RAO, and has its maximum at $z = 52$ m for all conditions.

For the lowest wave periods (conditions 1 to 6), FlexME-15MW demonstrates the largest damage overall. However, there is a smaller distinction between ME models and FlexPFT-15MW compared to the 10 MW results. FlexPFT-15MW has similar damage to FlexME-15MW and larger damage compared to RigidME-15MW for conditions 1, 2 and 6. For conditions 3 to 5, RigidME-15MW has larger fatigue damage than FlexPFT-15MW. The results imply that the 15 MW ME models do not necessarily have larger fatigue damage than FlexPFT-15MW for low wave periods. This does not imply that it contradicts the bending stress RAOs since the damage calculations also include axial force and moment about the z-axis (see Section 3.8.1). The difference in elasticity between RigidME-15MW and FlexPFT-15MW could affect this. In addition, RigidME-15MW has larger damage than RigidPFT-15MW for low T_p, which means that ME estimates larger tower fatigue for rigid spars.

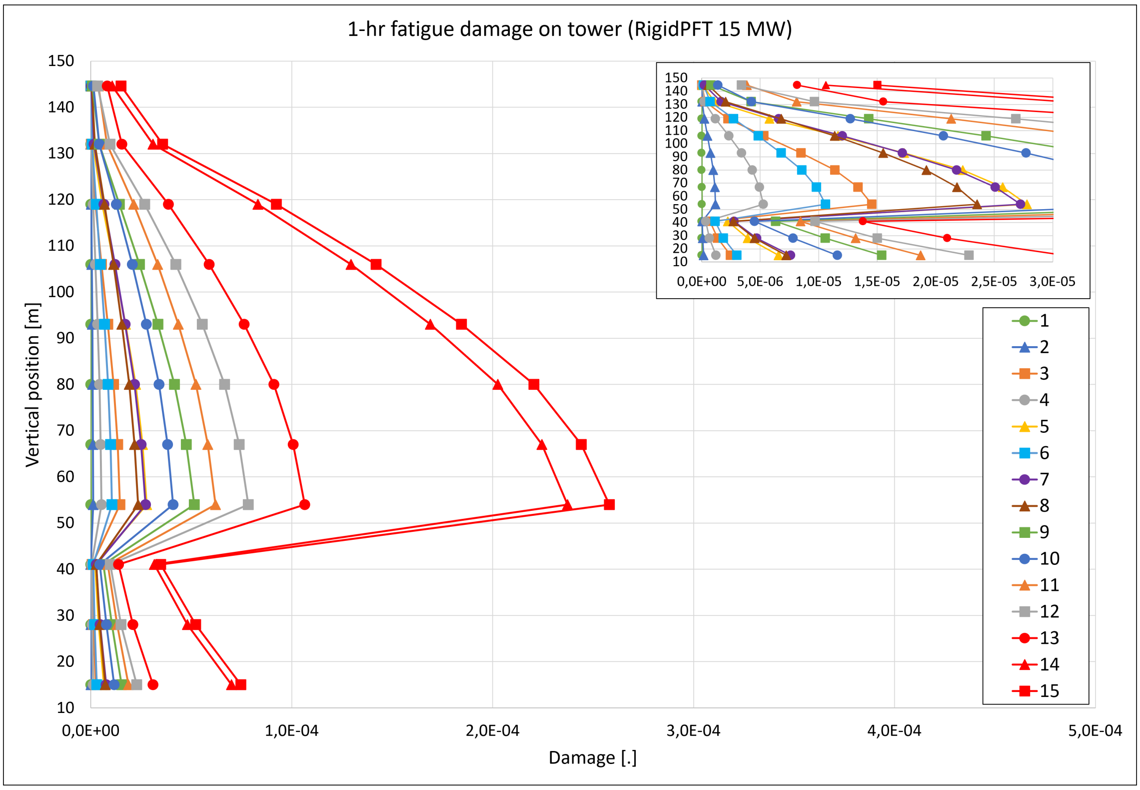

Figure 48: 1-hr fatigue damage for RigidPFT-15MW tower (Condition 1-15 in legend)

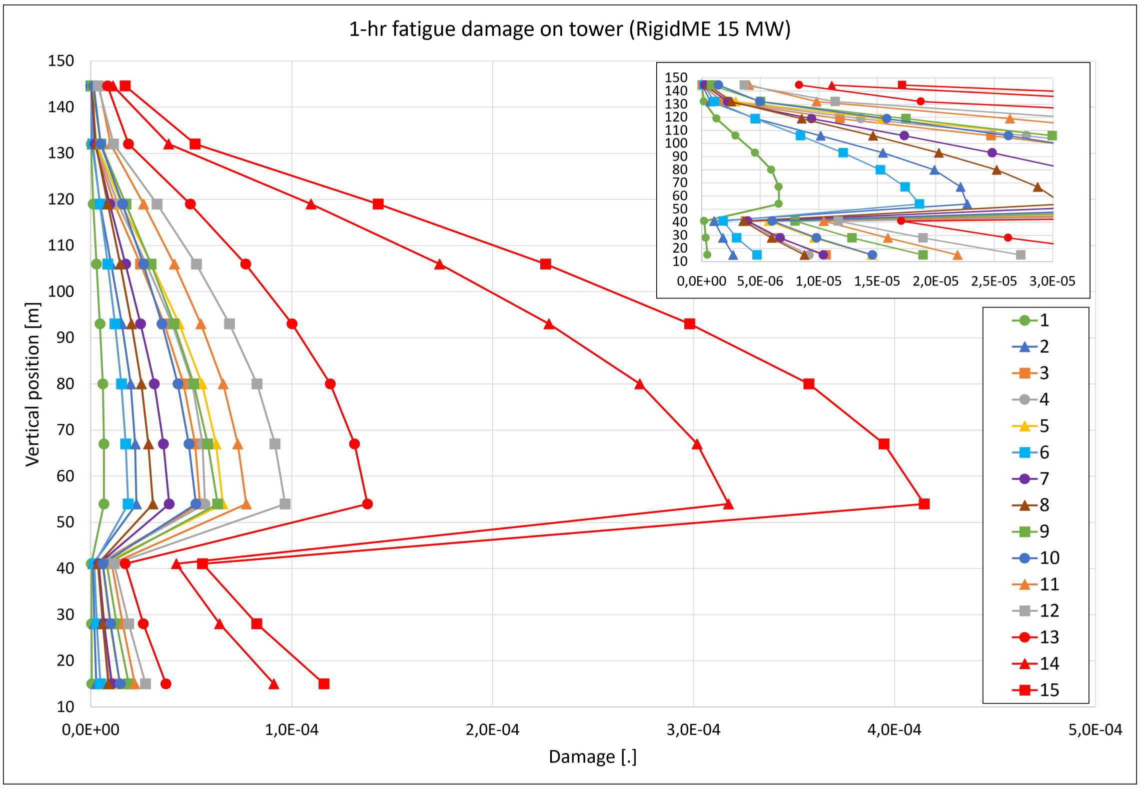

Figure 49: 1-hr fatigue damage for RigidME-15MW tower (Condition 1-15 in legend)

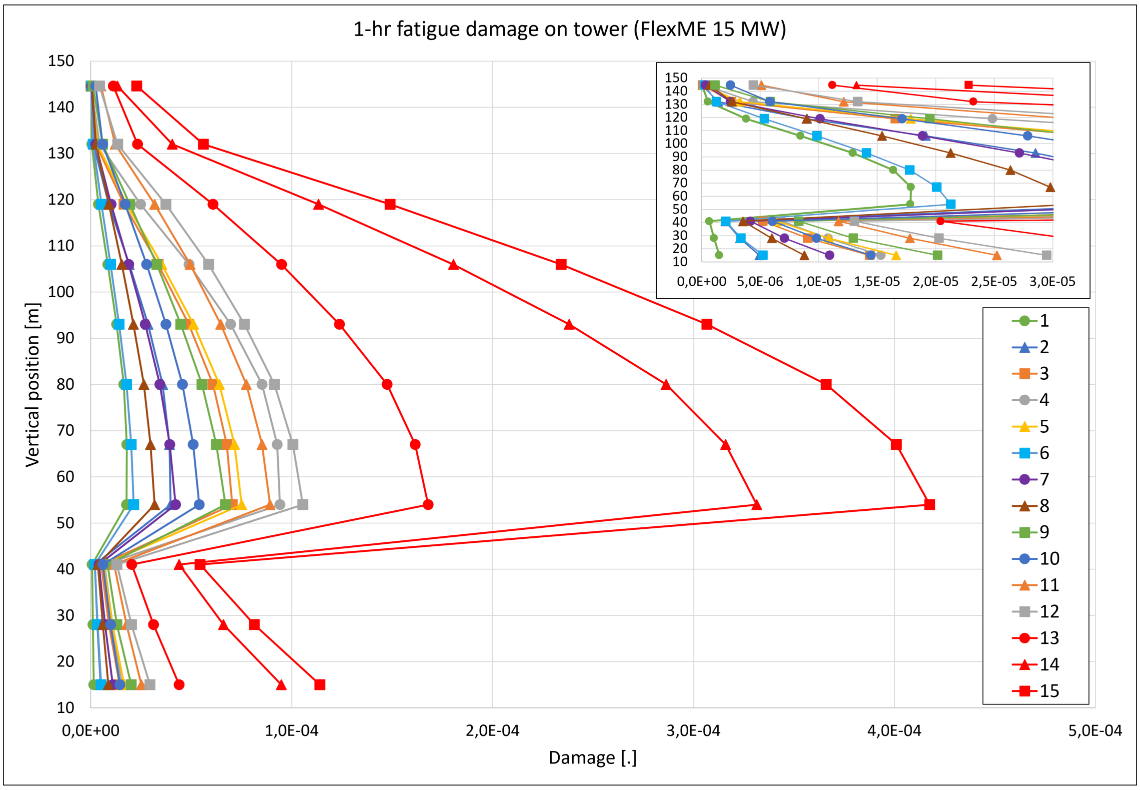

Figure 50: 1-hr fatigue damage for FlexME-15MW tower (Condition 1-15 in legend)

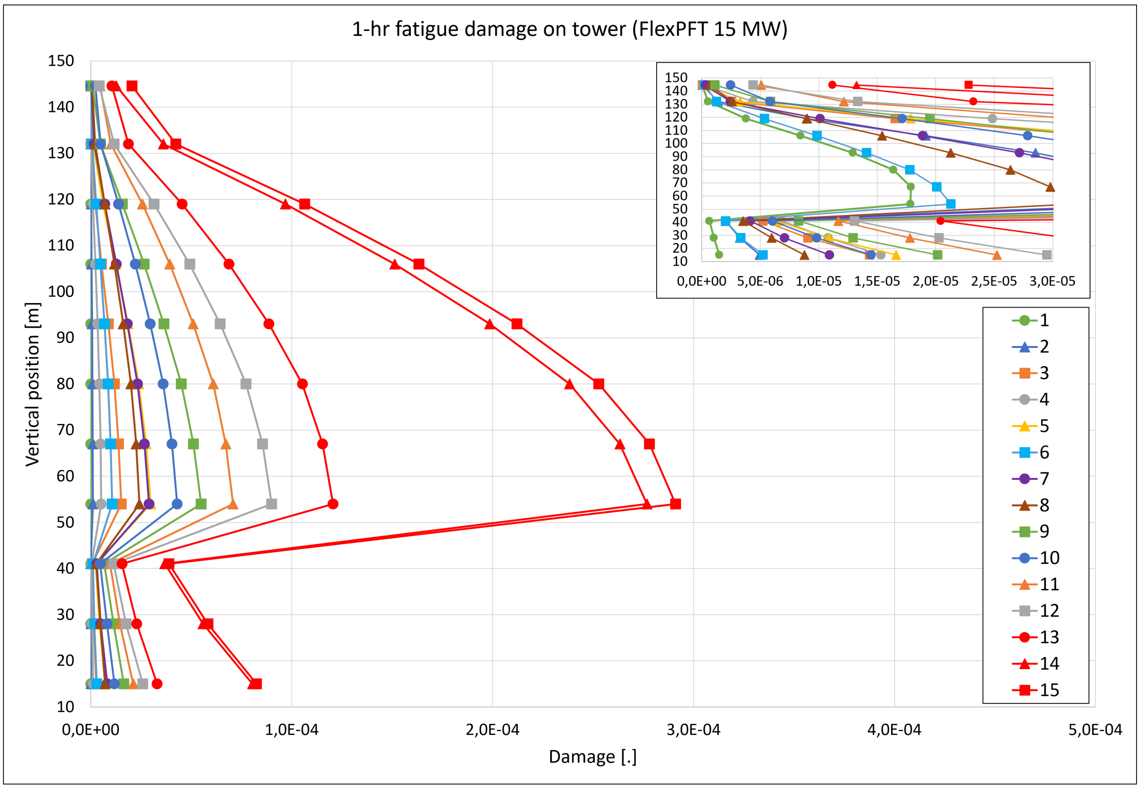

Figure 51: 1-hr fatigue damage for FlexPFT-15MW tower (Condition 1-15 in legend)

5.7.3 Fatigue Damage on 10 MW Spars

The 1-hr fatigue damage along the 10 MW flexible spars with respect to the vertical position is shown in Figure 52 and 53. Only the upper part of the spar is included because the damage is practically zero below z = -20 m. The maximum fatigue damage is at the top of the spars, and it declines in a similar fashion for both spars and all conditions. FlexME exhibits larger fatigue for low wave periods (conditions 1 to 6). The damage is similar for the other conditions, with some minor deviations.

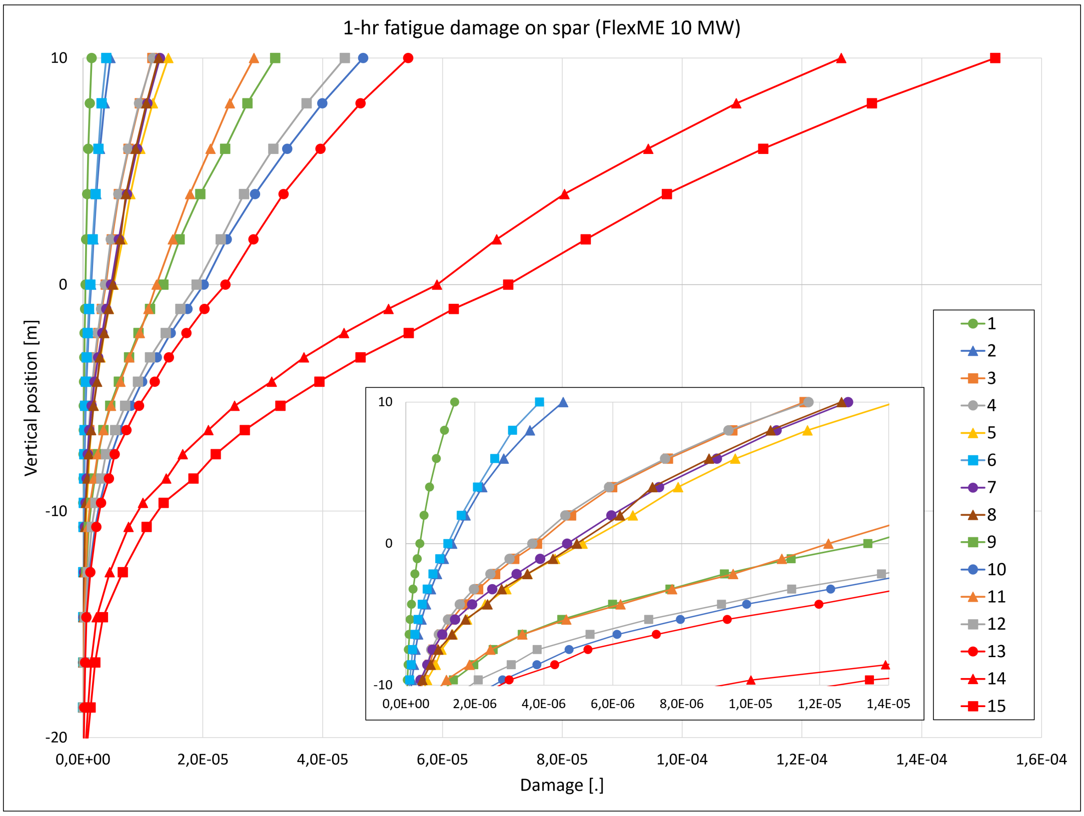

Figure 52: 1-hr fatigue damage for FlexME-10MW (Condition 1-15 in legend)

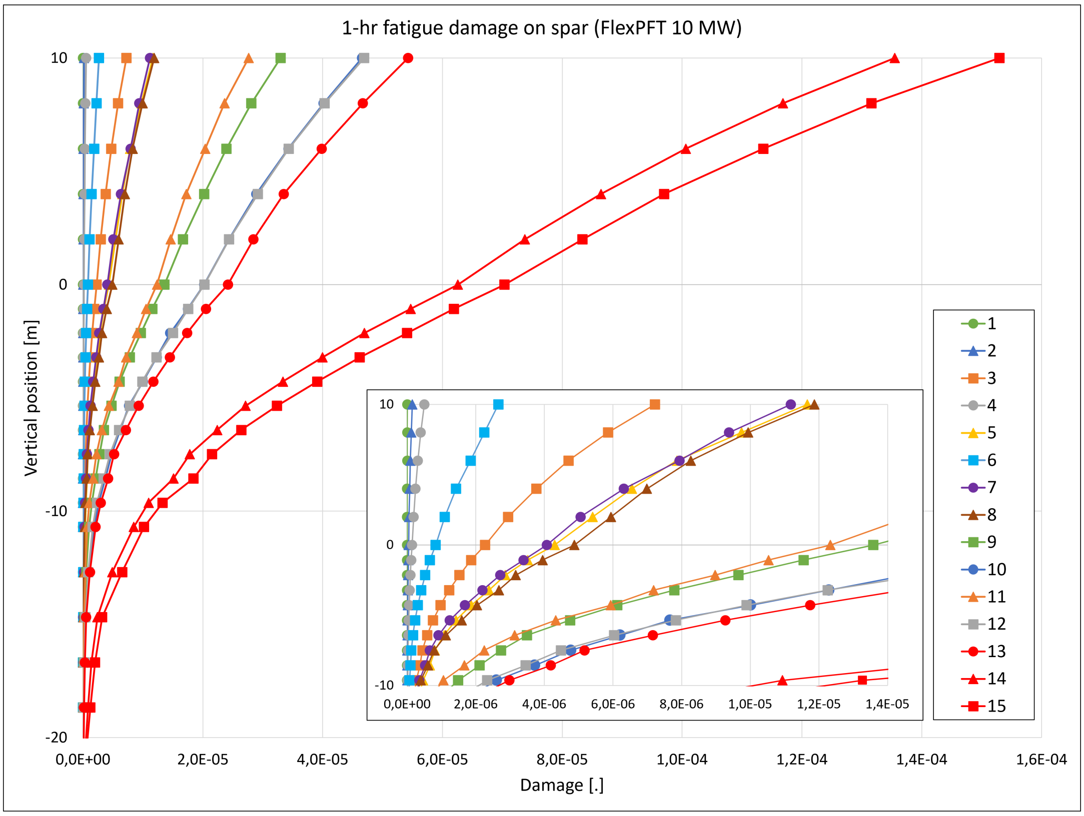

Figure 53: 1-hr fatigue damage for FlexPFT-10MW (Condition 1-15 in legend)

5.7.4 Fatigue Damage on 15 MW Spar

The results for the 15 MW flexible spars are displayed in Figure 54 and 55. The maximum fatigue damage is at the top of the spar (z = 15 m), and the damage is close to zero from z = -15 m and below. Similarly to the 10 MW spars, the FlexME-15MW displays larger fatigue for low wave periods. However, it is also larger for the other conditions. This indicates that using ME for the upscaled spar will increase the deviation in fatigue damage between ME and PFT, even for the larger wave periods.

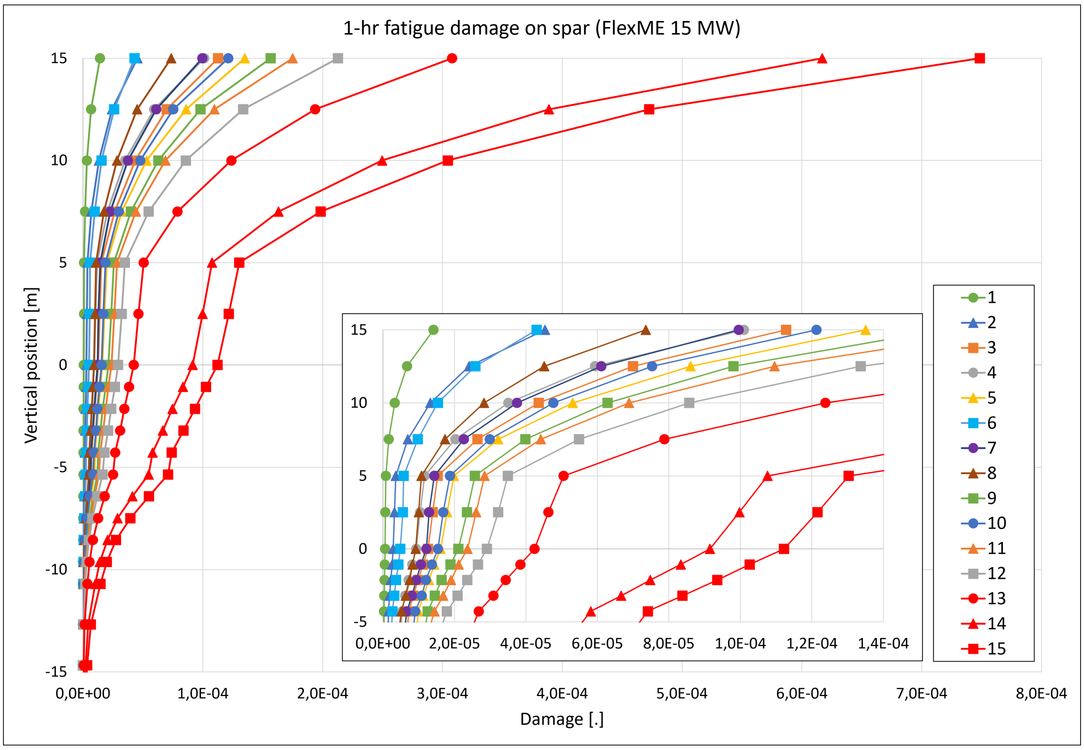

Figure 54: 1-hr fatigue damage for FlexME-15MW (Condition 1-15 in legend)

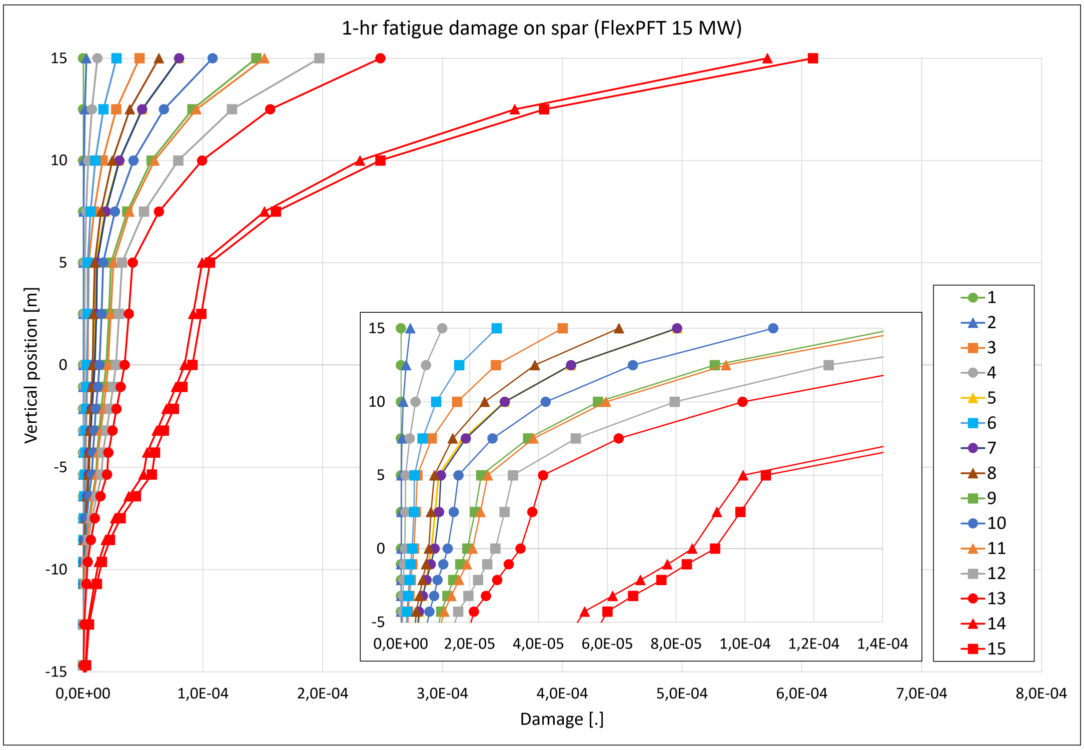

Figure 55: 1-hr fatigue damage for FlexPFT-15MW (Condition 1-15 in legend)

5.7.5 Damage Equivalent Loads

The damage equivalent loads (DEL) are calculated for condition 4 and 10 according to Section 3.8.2. The units are MPa per hour (MPa/hr) due to the time length of the irregular waves tests.

The DELs for 10 MW towers in condition 4 are shown in Figure 56a. The towers exhibit similar DELs, but the PFT models have the largest maximums (at z = 104 m). The distribution is comparable with the bending stress RAO, except for the small value at the base and larger values at z = 95 and 104 m. FlexME-15MW has smaller DELs at the lower parts of its tower compared to the other models (Figure 56b). The 15 MW towers also show a resemblance to the bending stress RAO, except for at the top, where the DELs are large. Unlike the results for fatigue damage, the DELs do not show larger values for the ME models.

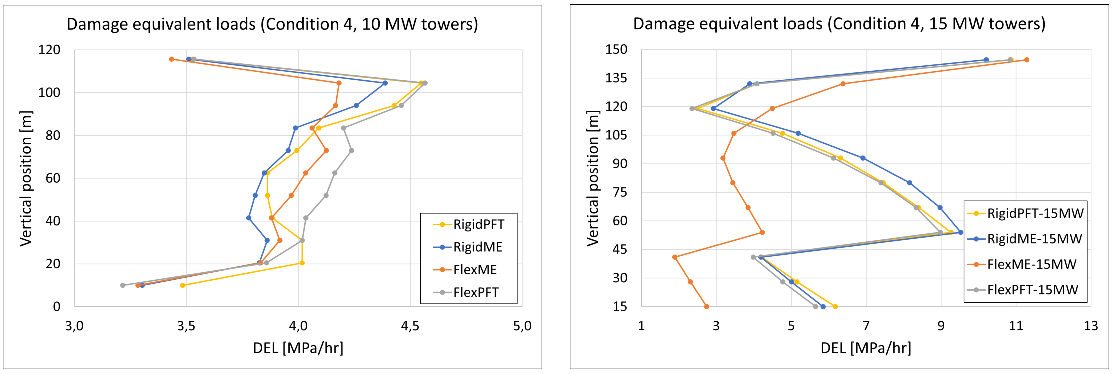

(a) 10 MW

(b) 15 MW

Figure 56: DEL on towers for condition 4

The flexible 10 MW spars has their maximum DELs at z = -5 m, below the SWL (Figure 57a). This is in contrast to both bending stress RAO and the fatigue damage, where the maximum is at the top of the spar. However, the 15 MW spars have the largest DELs at the top. Additionally, the difference between ME and PFT is small for both 10 and 15 MW spars. Hence, the spars do not display any significant deviation between the wave load models.

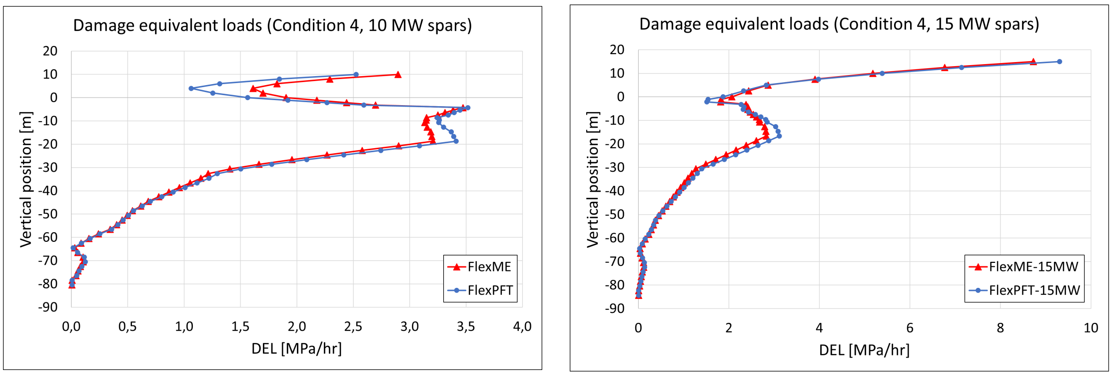

(a) 10 MW

(b) 15 MW

Figure 57: DEL on flexible spars for condition 4

For condition 10, the 10 MW flexible models have higher DELs in the tower overall (Figure 58a). The 15 MW towers has nearly identical DELs, see Figure 58b. In comparison, the fatigue damage estimates greater damage for the ME models in condition 10.

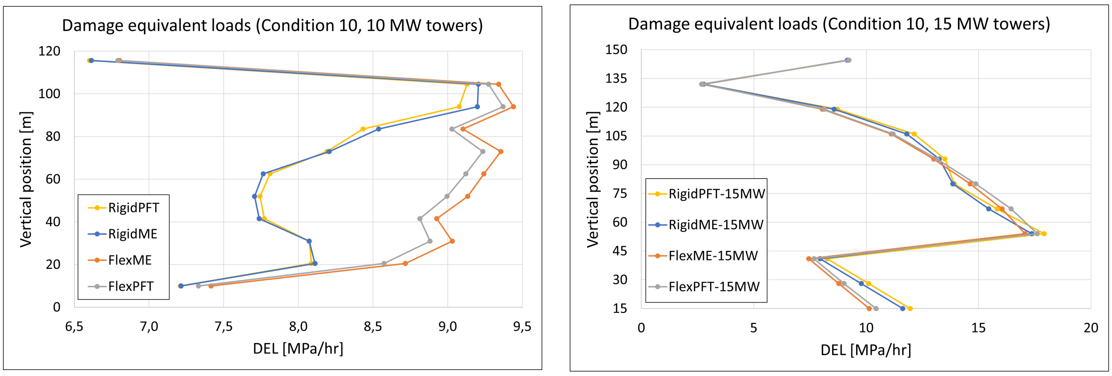

(a) 10 MW

(b) 15 MW

Figure 58: DEL on towers for condition 10

Unlike condition 4, both the 10 and 15 MW spars has its maximum DEL at the top in condition 10 (see Figure 59a and 59b). The ME and PFT models exhibit almost identical results, which is consistent with the fatigue damage along the spars for condition 10.

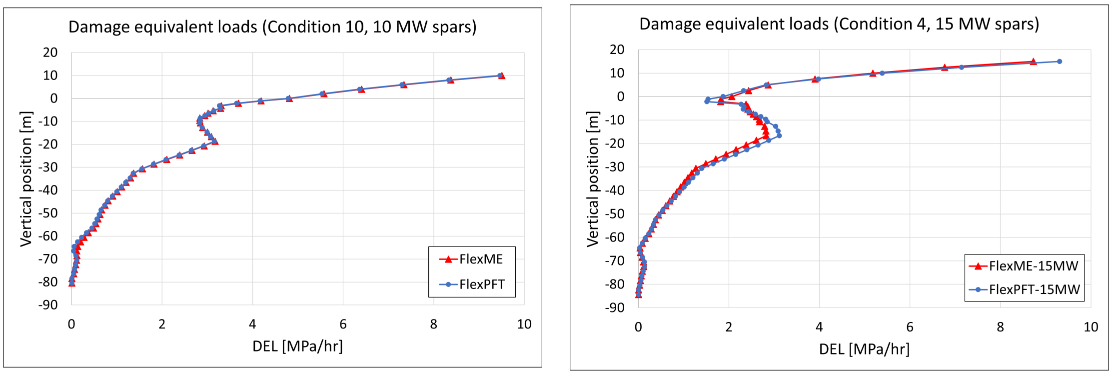

(a) 10 MW

(b) 15 MW

Figure 59: DEL on flexible spars for condition 10

5.7.6 Spectral Analysis - Surge

Spectral analysis for surge motion was performed for all models. Since the models exhibit similar results, only the FlexPFT models will be presented here. The spectral density function, $S(\omega)$, is given with respect to natural angular frequency for FlexPFT-10MW in Figure 60.

The largest energy concentrations are located to the left in Figure 60 for frequencies ω = 0-0.06 rad/s. These are wind frequencies, which means that the main excitation source in surge is wind excitation. The conditions with U_w close to rated wind speed are largest here (conditions 6 to 11). The largest peak is located near the natural period in surge ($\omega_{n,1} = 0.047$ rad/s for PFT models) and occurs for condition 8. The energy accumulation from ω = 0.12-0.18 rad/s is also from wind. The conditions with the largest U_w (14-20 m/s) displays the most energy here (condition 11 to 15).

A close-up is given in Figure 60 in order to study the wave frequencies. There is a small energy accumulation from ω = 0.3-0.7 rad/s due to wave excitation. The conditions with the largest H_s are governing here (i.e. condition 9, 14 and 15).

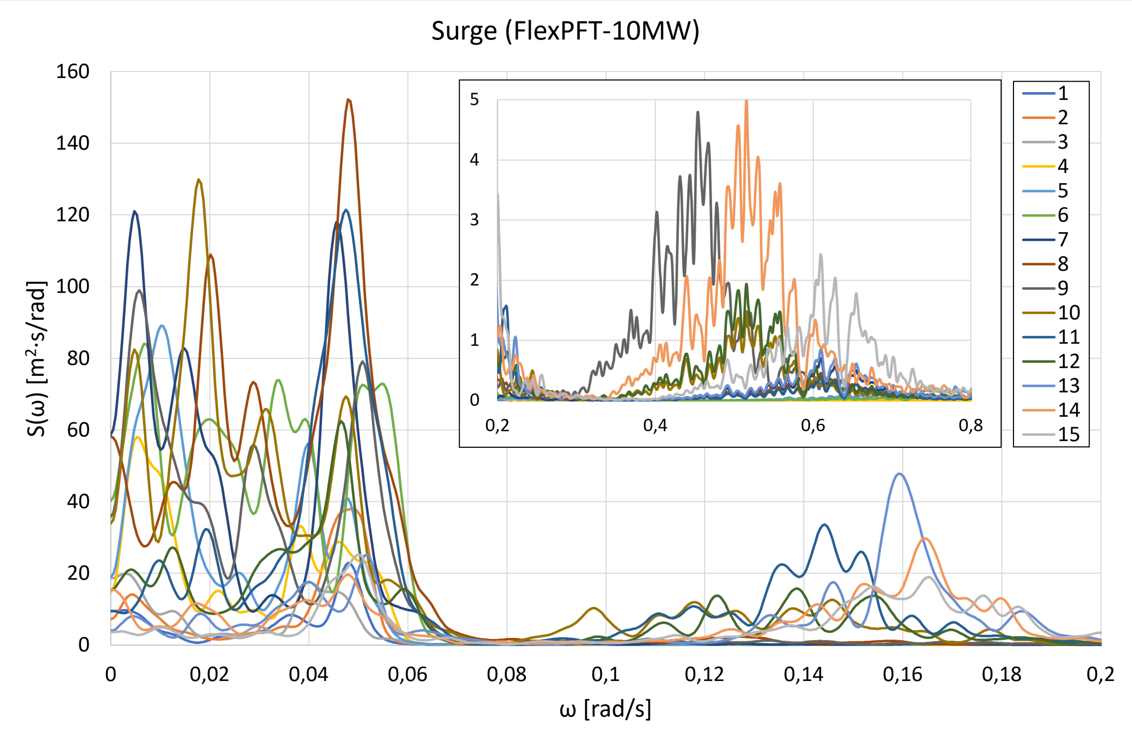

Figure 60: Spectral analysis in surge for FlexPFT-10MW, but all models have similar results (Condition 1-15 in legend)

The results for FlexPFT-15MW are shown in Figure 61 and exhibits similar results to FlexPFT-10MW, although the overall wind excitation is higher. The upscaled spar is exposed to more wind since it is located at $z = 15$ m instead of 10 m, and more importantly, the tower stretches up to 150 m compared to 119 m for the 10 MW. On another note, the largest peak is now given by condition 4, which has much higher energy in the wind frequency region in comparison to FlexPFT-10MW.

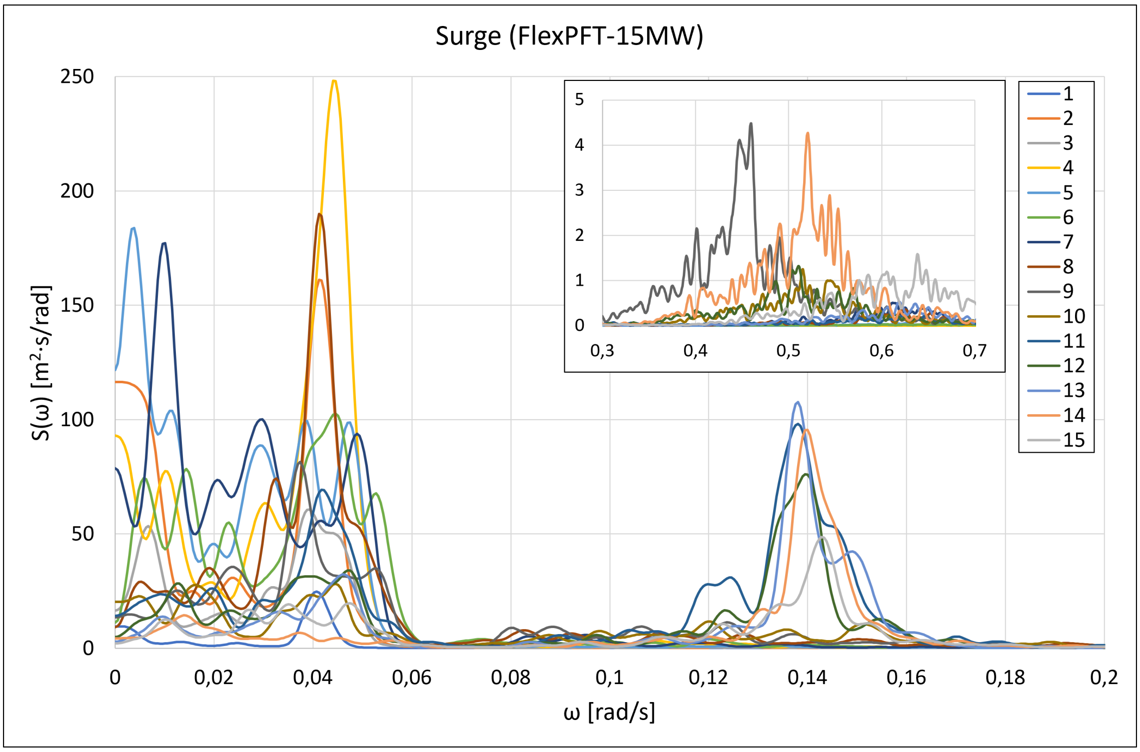

Figure 61: Spectral analysis in surge for FlexPFT-15MW, but all models have similar results (Condition 1-15 in legend)

5.7.7 Spectral Analysis - Pitch

Spectral analysis in pitch was performed in the same manner as in surge, and only the FlexPFT models are shown here due to corresponding results between the models. The pitch spectrum for FlexPFT-10MW is given in Figure 62.

The spectrum is smaller for low frequencies (ω = 0-0.06 rad/s) compared to surge, but has a larger energy accumulation from ω = 0.1-0.2 rad/s. The conditions with the largest U_w is excited the most here (conditions 10 to 15), and condition 13 has the maximum peak at $\omega = 0.16$ rad/s. The natural period in pitch is $\omega_{n,5} = 0.189$ rad/s, but no concentration of energy is shown there.

Similar to surge the pitch spectrum has low energy in the wave excitation region, see close-up in Figure 62 (ω = 0.3-0.7 rad/s). The conditions with largest H_s are most significant here (conditions 9, 14 and 15).

The overall wind excitation is larger for FlexPFT-15MW, but other than that, the results display much of the same (see Figure 63). The energy is accumulated within a smaller region, and condition 13 has the maximum peak at $\omega = 0.14$ rad/s. Also, condition 10 exhibits much smaller energy compared to FlexPFT-10MW. No significant energy concentrations are located at the natural period in pitch ($\omega = 0.155$ rad/s).

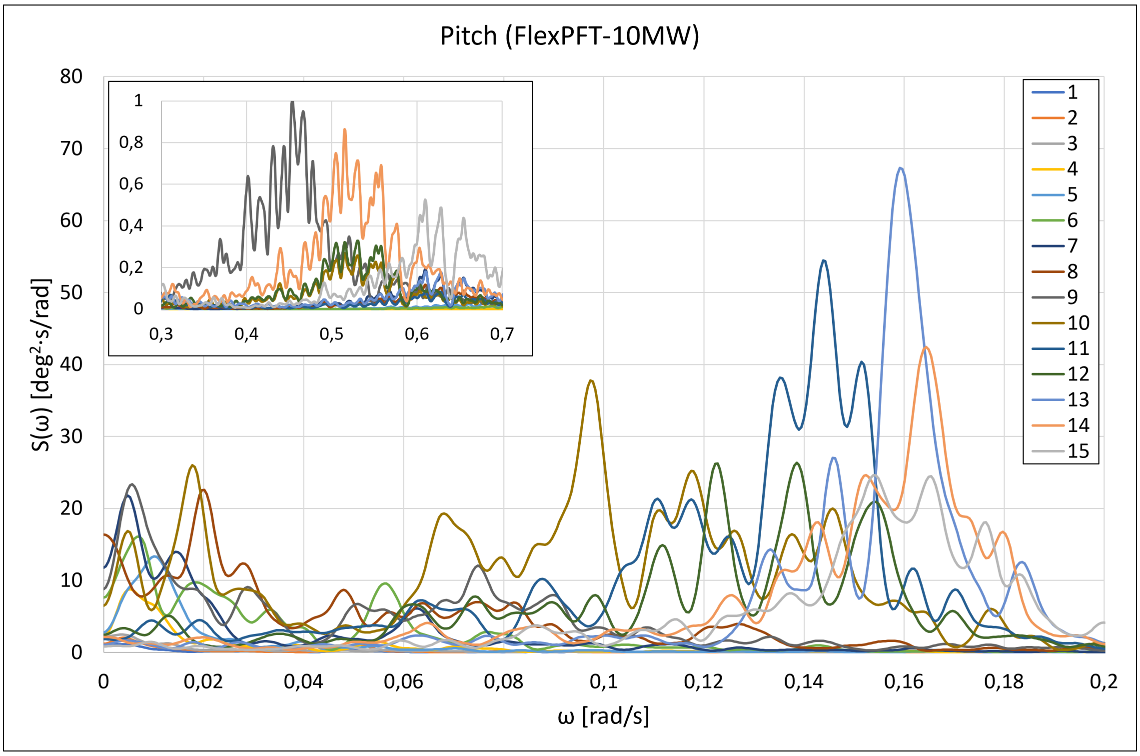

Figure 62: Spectral analysis in pitch for FlexPFT-10MW, but all models have similar results (Condition 1-15 in legend)

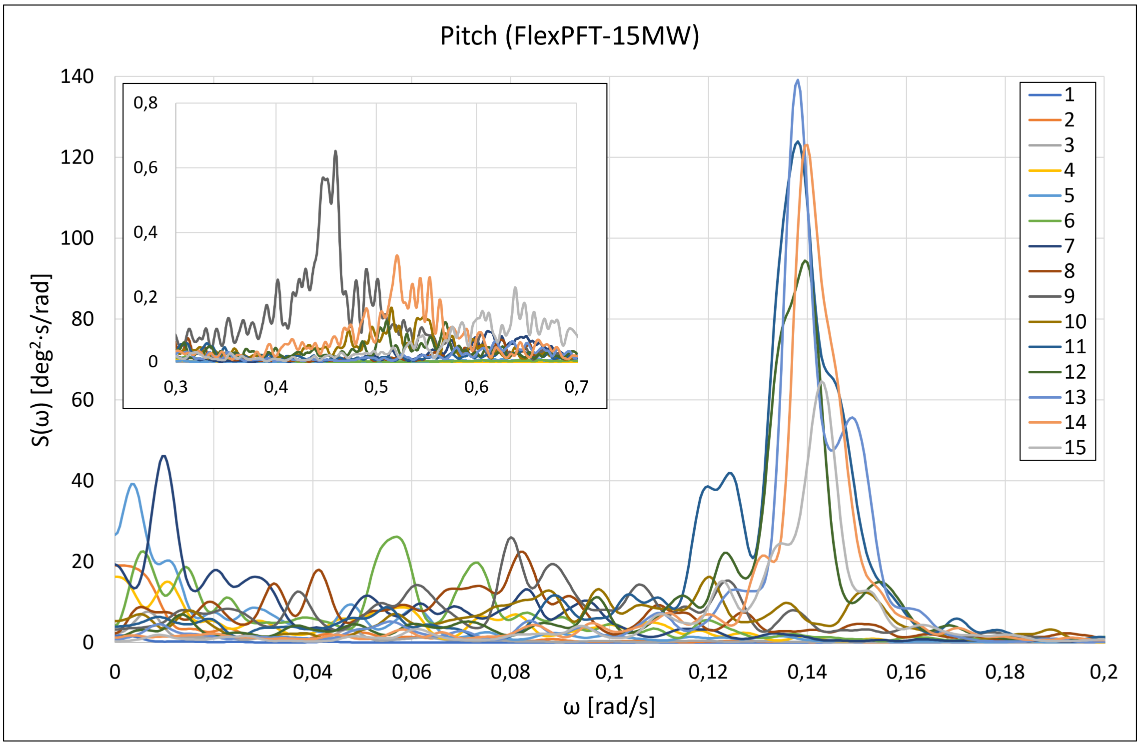

Figure 63: Spectral analysis in pitch for FlexPFT-15MW, but all models have similar results (Condition 1-15 in legend)

5.7.8 Spectral Analysis - Bending Moment at Tower Base

In order to study the tower excitations, spectral analysis for the bending moment at the base of the towers was conducted. The tower base was excited by wind and waves, and the bending moment is clearly linked to pitch excitations. The bending moment spectrum essentially replicates the pitch spectrum in the wind and wave frequency regions, resulting in similar behavior to pitch for the different conditions. The results are therefore included in Appendix C.

For larger frequencies outside the range of wind and wave excitations, the bending moment experience concentrations of energy for all models. They are smaller than the values for wind and waves, but not insignificant. These concentrations represent the tower base fore-aft bending natural periods, estimated in the decay tests earlier (Section 5.5.3). Recall that the 1st bending natural periods of the 10 MW towers are well within the stiff-stiff region, and should not experience resonance due to the rotational frequency (1p) or blade passing frequency (3p).

The natural periods for the 10 MW towers can be found in Figure 64 below. Since all the periods are outside the frequencies of excitation (wind, waves, 1p, 3p), the towers could be excited by one of the multiples of 1p or 3p. The results from the decay tests estimated natural periods of 5.89, 5.68, 5.03 and 5.32 rad/s for RigidPFT, RigidME, FlexME and FlexPFT, respectively. This agrees well with Figure 64.

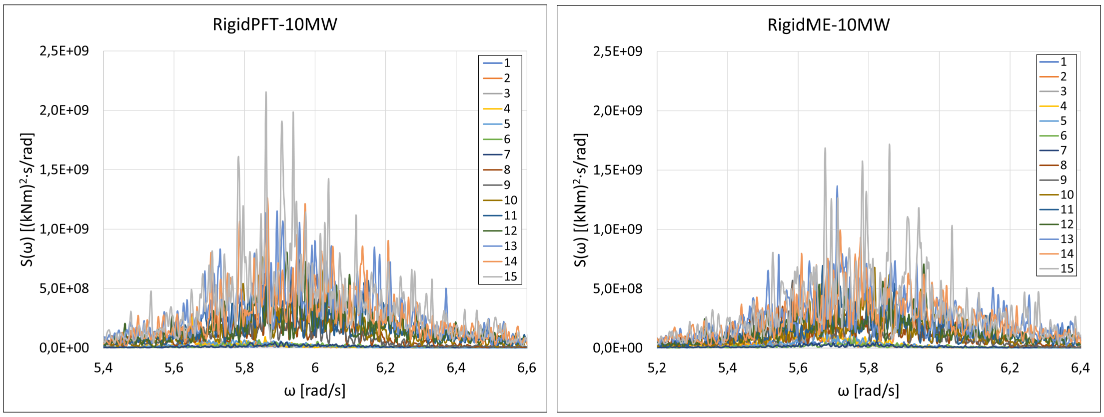

(a) RigidPFT 10 MW

(b) RigidME 10 MW

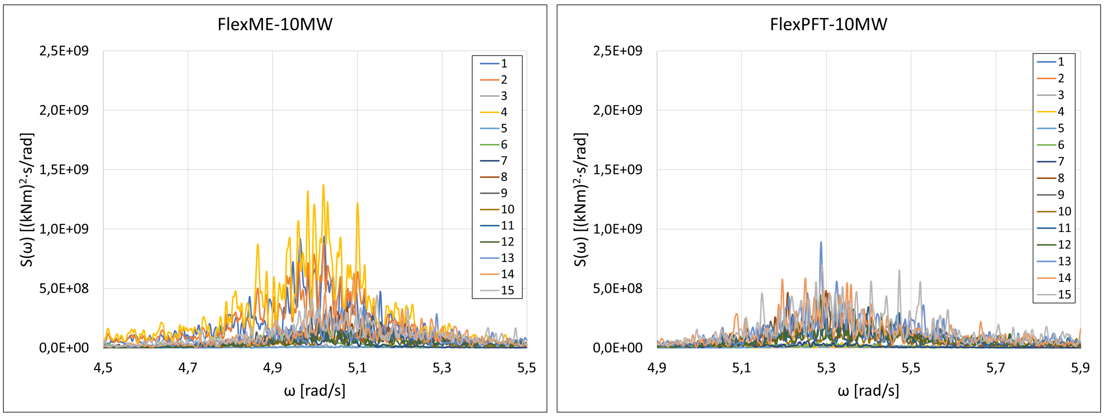

(c) FlexME 10 MW

(d) FlexPFT 10 MW

Figure 64: Excitation of 1st bending mode, 10 MW towers (Condition 1-15 in legend)

Excitation of the 1st bending natural periods for the 15 MW towers is shown in Figure 65, which appears at lower frequencies compared to the 10 MW towers. The natural periods are closer to 3p frequency here, but still within the stiff-stiff region. However, it is possible that high-frequency waves could excite the 15 MW towers due to the small natural periods.

The natural periods from the decay tests are 2.9, 2.73, 2.69 and 2.79 rad/s for RigidPFT-15MW, RigidME-15MW, FlexME-15MW and FlexPFT-15MW, respectively. Notice that larger values are used on the y-axis for the ME models, since they are excited more than the PFT models (especially FlexME-15MW). Condition 4 (yellow line) has a $T_p = 5$ s, and the ME models are excited considerably more for this condition. Based on this observation, condition 4 will be inspected in greater detail in the next section.

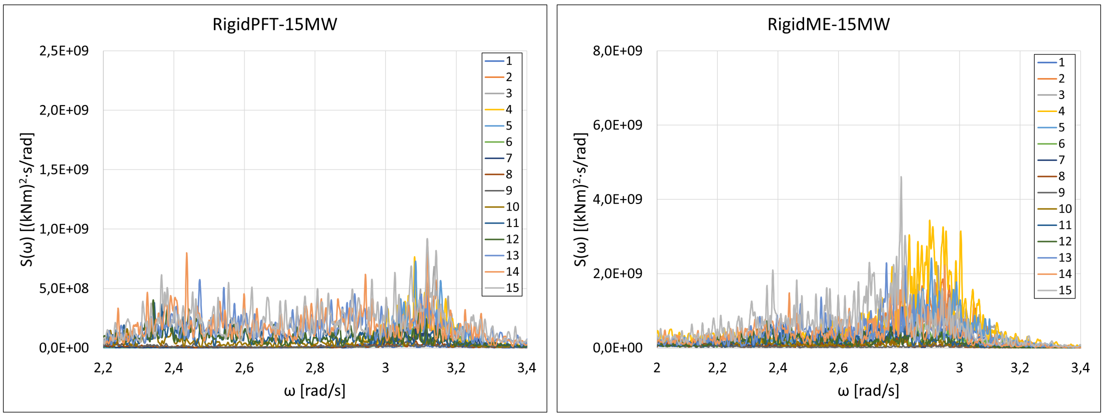

(a) RigidPFT 15 MW

(b) RigidME 15 MW

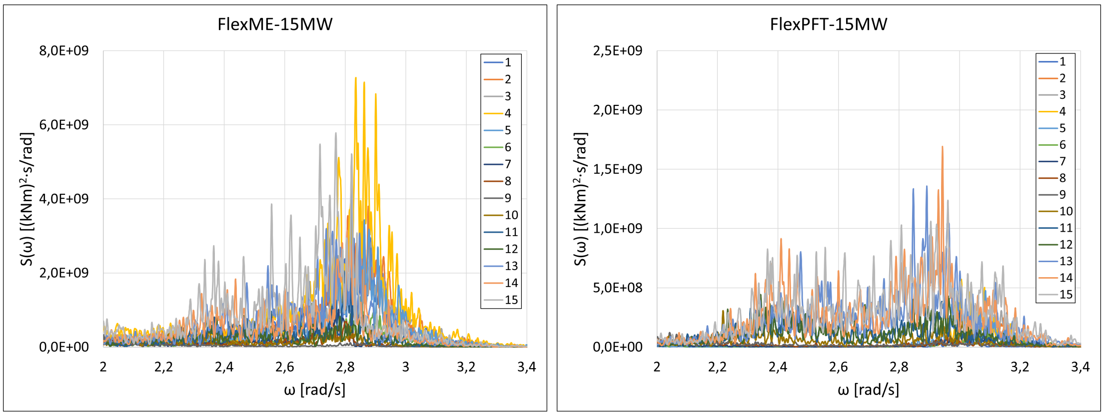

(c) FlexME 15 MW

(d) FlexPFT 15 MW

Figure 65: Excitation of 1st bending mode, 15 MW towers (Condition 1-15 in legend)

5.7.9 Spectral Analysis - Bending Moment in Condition 4

The spectral analysis for bending moment in condition 4 ($H_s = 1.5$ m, $T_p = 5$ s, $U_w = 6$ m/s) is shown in Figure 66 for 10 MW towers. The ME models exhibit larger wave excitations. Note that they are similar until $\omega = 1$ rad/s. Recall the bending moment RAO from earlier (Figure 37), where the bending moment starts to decrease for the PFT models from $\omega = 1$ rad/s while it increases for the ME models. This leads to the large deviation for higher frequencies. In addition, the 1st bending mode of the tower is significantly excited for the ME models, especially FlexME (northeast corner of Figure 66). This implies that other excitations than waves is affected by choice of wave load model.

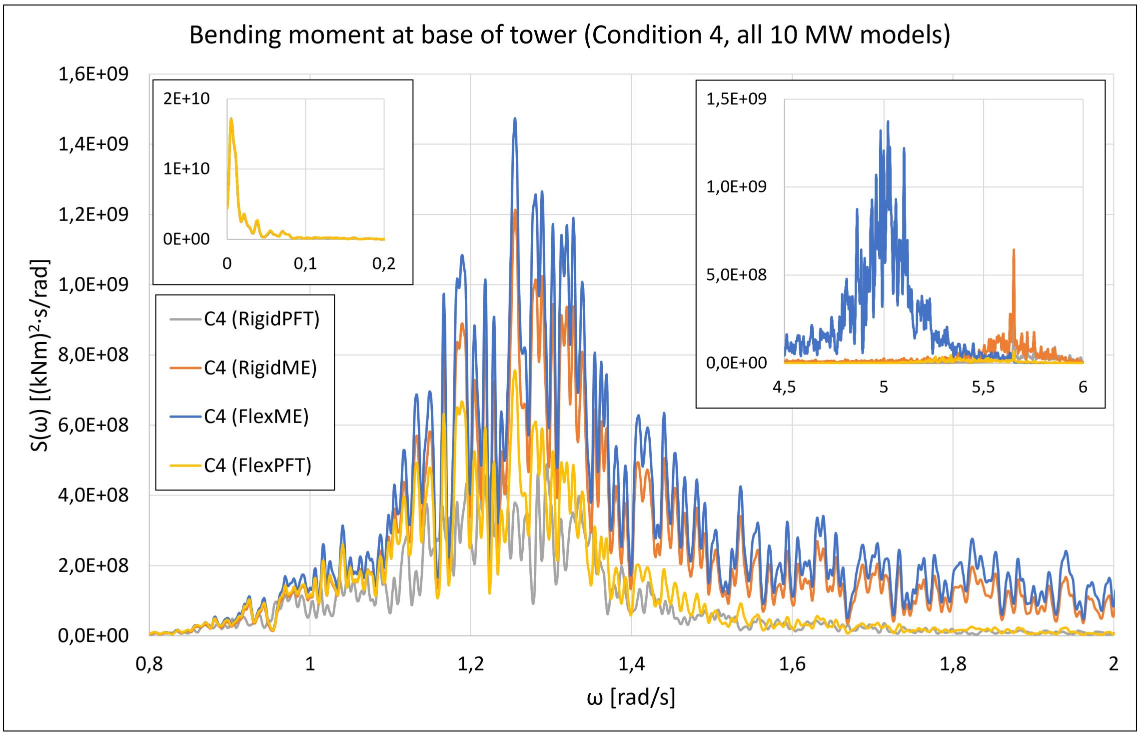

Figure 66: Condition 4, 10 MW models

The 15 MW towers display similar results, but the difference between the ME and PFT models are even higher (Figure 67). Recall that the bending moment RAO for the 15 MW towers exhibits a larger deviation between ME and PFT for $\omega > 1$ rad/s compared to 10 MW towers (Figure 68). The 1st bending mode is only excited for the ME models. The 15 MW towers are excited by waves due to the low natural angular periods.

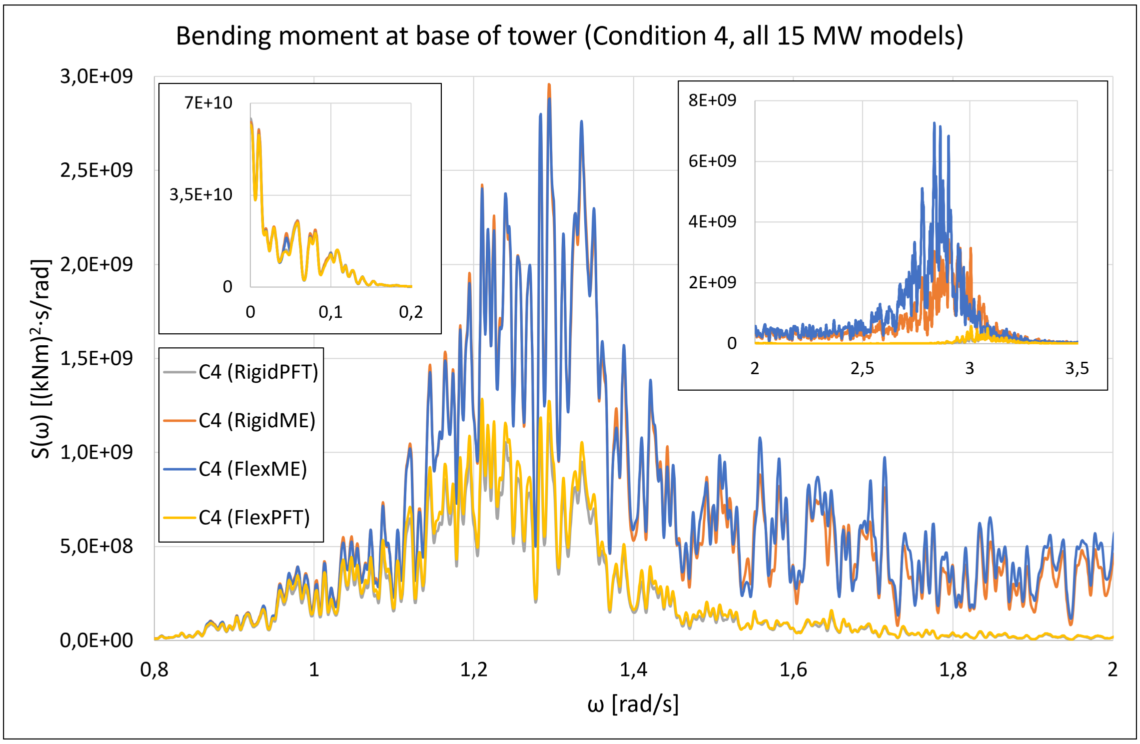

Figure 67: Condition 4, 15 MW models

6 Conclusion

This thesis was conducted in order to investigate how elasticity, wave load modeling and upscaling effects the wave-induced responses on spar foundations. The optimized 10 MW design made by Hegseth et al. [17] was used to support the 10 MW DTU wind turbine [4]. Rigid and flexible models were developed to compare elasticity. Linear potential flow theory (PFT) and Morison's equation (ME) was used to model wave loads. Based on a similar approach used by Svendsen [33], radiation and diffraction pressures from linear potential theory were computed using WAMIT and then implemented to a flexible model. An upscaled version of the 10 MW spar was designed to support the 15 MW IEA wind turbine [1] and the tower developed by the University of Maine [15].

The hydrodynamic properties were established for the spars. Wave excitations in surge and pitch were larger for the ME models for higher wave frequencies ($\omega > 1$) since ME is based on a long-wave approximation. The added mass is greater for the ME models in surge and pitch, and it is frequency-independent since it is based on strip theory. WAMIT estimates larger damping in pitch compared to the rigid PFT model. Radiation damping is not included in the ME models, and quadratic damping is the same for all models. The constant wind tests demonstrated reassuring results, and the rotor behaved as expected.

The natural periods found from free decay tests displayed similar outcomes for surge, heave and pitch. Yaw natural periods are twice as high for the rigid models, and it is suspected that the inertia from ballast is not included for the flexible models. To ensure this did not pollute the results, the yaw motions were validated by inspection of the results. The 1st pitch bending natural frequencies at the tower base reveals that all 10 MW models are well within the stiff-stiff region, and that the flexible models have smaller natural frequencies. 15 MW models are closer to the 3p frequency, since they are longer and hull steel weight was minimally increased (36% larger than 10 MW spar).

The response amplitude operators (RAO) in surge, heave and pitch indicates similar behavior for the models, except for the flexible ME model in heave. The bending moment is largest at the base of the tower and the top of the spar. The bending stress takes the cross-sections into account, and the 10 MW tower shows an even distribution of stress along its length (optimized design). The more conventional 15 MW tower exhibits larger stress at the middle. The RAOs are linked to excitations and explains why the surge, pitch, moment and stress are larger for the ME models when $\omega > 1$. The deviation is more prominent for the upscaled spar, although the excitations in pitch are similar for the 10 and 15 MW ME models when $\omega > 1$. This could be an upscaling effect independent of wave load modeling and rather a result of the 15 MW model being longer and more elastic.

Fifteen sea conditions were tested in irregular waves with turbulent wind. The fatigue damage is generally larger for the ME models in conditions with low peak periods (T_p). This is consistent with the bending stress RAO. Damage equivalent loads (DEL) does not exhibit the same deviation between ME and PFT. The spectral analysis displays similar results for all models in surge and pitch, and both motions are mainly excited by wind. The spectra for bending moment at the base of the tower resembles the pitch spectra in the wind and wave frequencies. Small peaks are located near the natural bending frequencies. The 10 MW models are likely excited by a multiple of 3p, while the 15 MW models have such low natural frequencies that they are excited by waves. In condition 4 ($T_p = 5$ s) the ME models were significantly excited at the natural bending frequencies while PFT models were not excited. The 10 MW natural periods are well outside of wave frequencies, and implies that other excitations than waves can be affected by choice of wave load model.

7 Recommendations for further work

The recommendations for further work are given below.

1. It is suspected that the inertia from ballast is missing in the flexible models. If true, this affects the yaw inertia and also the pitch inertia to some extent. If these models are to be used further, this should be looked into.
2. Based on the results, the upscaling procedure seems to have worked well. The upscaled spar shows similar hydrodynamic properties to the 10 MW spar. It would be interesting to use the same upscaling procedure to create a spar able to support a 20 MW wind turbine.
3. The different towers used for the 10 and 15 MW spars opens up for misinterpretations of the results. Making an upscaled version of the 10 MW tower to fit the 15 MW spar could give more insight into upscaling effects.
4. Damage equivalent loads (DEL) are commonly used in the industry when examining towers and substructures of FWTs. The results indicate that they provide a different perception of the fatigue damage, and this area could be interesting to explore. The methods could prove more conservative for different cases, which is always important to keep in mind when working with structural design. Developing a code for when the different approaches should be used would be beneficial.
5. The models could be tested for extreme weather conditions to investigate how the different modeling approaches (elasticity, wave load models) affect the results.
6. Reducing the costs of FWTs is a hot topic. It would be relevant to compare the expenses of the 10 and 15 MW spars, for example by determining the levelized cost of energy (LCOE).
7. The approach used to implement radiation and diffraction pressures from linear potential flow theory to a flexible spar provides a more complete, combined representation of elasticity in the hull and hydrodynamic loads. Although it would be more challenging to use this approach for a semi-submersible with more complex geometry than a spar, it would be very interesting. A simpler option would be a barge, perhaps with a moonpool since that is more relevant for the industry.

Bibliography

[1] Allen et al. *Definition of the IEA 15-Megawatt Offshore Reference Wind Turbine.* Golden, CO: National Renewable Energy Laboratory, 2020.

[2] O. Apata and D. T. O. Oyedokun. *An overview of control techniques for wind turbine systems*, 2020. Url: https://www.sciencedirect.com/science/article/pii/S2468227620303045.

[3] E. E. Bachynski. *Design and Dynamic Analysis of Tension Leg Platform Wind Turbines.* Norwegian University of Science and Technology, 2014.

[4] C. Bak et al. *The DTU 10-MW Reference Wind Turbine.* Technical University of Denmark (DTU), 2013. Url: https://backend.orbit.dtu.dk/ws/portalfiles/portal/55645274/The_DTU_10MW_ Reference_Turbine_Christian_Bak.pdf.

[5] N. D. P. Barltrop. *Floating Structures: A Guide for Design and Analysis.* Centre for Marine and Petroleum Technology, 1998.

[6] Beatrice Offshore Windfarm Ltd. *Beatrice Offshore Windfarm Ltd - Scotland's largest operational offshore wind farm*, 2021. Url: https://www.beatricewind.com/.

[7] Det Norske Veritas. *Environmental Conditions and Environmental Loads.* 2010. Url: https://rules.dnv.com/docs/pdf/DNVPM/codes/docs/2010-10/rp-c205.pdf.

[8] Det Norske Veritas. *Fatigue Design of Offshore Steel Structures.* 2011.

[9] Equinor. *The future of offshore wind is afloat*, 2020. Url: https://www.equinor.com/en/what-we-do/floating-wind.html.

[10] Equinor. *Hywind Scotland remains the UK's best performing offshore wind farm*, 2021. Url: https://www.equinor.com/en/news/20210323-hywind-scotland-uk-best-performing-offshore-wind-farm.html.

[11] Equinor. *Hywind Demo*, 2021. Url: https://www.equinor.com/en/what-we-do/floating-wind/hywind-demo.html.

[12] Equinor. *Hywind Scotland*, 2021. Url: https://www.equinor.com/no/what-we-do/floating-wind/hywind-scotland.html.

[13] Equinor. *Hywind Tampen*, 2021. Url: https://www.equinor.com/en/what-we-do/hywind-tampen.html.

[14] Faltinsen, O.M. *Sea Loads on Ships and Offshore Structures.* Cambridge University Press, 1990.

[15] Gaertner et al. *Definition of the UMaine VolturnUS-S Reference Platform Developed for the IEA Wind 15-Megawatt Offshore Reference Wind Turbine.* Golden, CO: National Renewable Energy Laboratory, 2020.

[16] T. Haukaas. *Euler-Bernoulli Beams*, 2020. Url: http://civil-terje.sites.olt.ubc.ca/files/2020/02/Euler-Bernoulli-Beams.pdf.

[17] J. M. Hegseth, E. E. Bachynski, and J. R. R. A. Martins. *Integrated design optimization of spar floating wind turbines.* Elsevier Ltd, 2020.

[18] J. R. Hoff. *Estimation of linear and quadratic roll damping from free-decay tests.* Technical Report, 601882, NTNU, 2001.

[19] Y. Kikuchi and T. Ishihara. *Upscaling and levelized cost of energy for offshore wind turbines supported by semi-submersible floating platforms.* Journal of Physics: Conference Series 1356 012033, 2019.

[20] H. Lamb. *Hydrodynamics.* Cambridge University Press, Cambridge, 1932.

[21] I. Langen and R. Sigbjørnsson. *Dynamisk analyse av konstruksjoner.* Tapir, Trondheim, 1979.

[22] C. M. Larsen. *Marine Dynamics.* Department of Marine Technology, NTNU, 2015.

[23] C.-H. Lee. *WAMIT Theory Manual.* Massachusetts Institute of Technology, 1995. Url: https://www.wamit.com/Publications/tmanual.pdf.

[24] M. Leimeister, E. E. Bachynski, M. Muskulus, and P. Thomas. *Rational upscaling of a semi-submersible floating platform supporting a wind turbine.* Elsevier Ltd, 2016.

[25] L. Li, Z. Gao, and T. Moan. *Joint Environmental Data at five European Offshore Sites for Design of Combined Wind and Wave Energy Devices.* ASME, 2013.

[26] E. Martiniussen. *Aker Solutions utfordrer Equinor på flytende havvind*, 2019. Url: https://www.tu.no/artikler/aker-solutions-utfordrer-equinor-pa-flytende-havvind-br/473077.

[27] MathWorks. *Rainflow counts for fatigue analysis*, 2020. Url: https://www.mathworks.com/help/signal/ref/rainflow.html.

[28] National Renewable Energy Laboratory. *TurbSim*, 2021. Url: https://www.nrel.gov/wind/nwtc/turbsim.html.

[29] Rystad Energy. *Size matters in offshore wind: Why Costlier 14 MW turbines actually reduce the large-scale farm bill*, 2020. Url: https://www.rystadenergy.com/newsevents/news/press-releases/size-matters-in-offshore-wind-why-costlier-14-mw-turbines-actually-reduce-the-large-scale-farm-bill/.

[30] Siemens. *Calculating damage with Miner's Rule.* 2019.

[31] SINTEF Ocean. *RIFLEX 4.18.1 Theory Manual.* 2020.

[32] SINTEF Ocean. *RIFLEX 4.18.1 User Guide.* 2020.

[33] K. F. Svendsen. *Structural Design and Dynamic Analysis of a Tension Leg Platform Wind Turbine, Considering Elasticity in the Hull.* Norwegian University of Science and Technology / Delft University of Technology, 2016.

[34] L. Tao and K. Thiagarajan. *Heave Response of Classic Spar with Variable Geometry.* Journal of Offshore Mechanics and Arctic Engineering, 2004.

A Geometry of Flexible Spars

Segment	Elevation wrt. SWL [m]		L [m]	D [m]	t [m]
	End 1	**End 2**			
1	10	8	2	12.66	0.0623
2	8	6	2	12.673	0.0648
3	6	4	2	12.686	0.0674
4	4	2	2	12.7	0.0700
5	2	0	2	12.713	0.0725
6	0	-1.07	1.07	12.726	0.0745
7	-1.07	-2.14	1.07	12.733	0.0759
8	-2.14	-3.21	1.07	12.74	0.0772
9	-3.21	-4.28	1.07	12.747	0.0786
10	-4.28	-5.35	1.07	12.754	0.0800
11	-5.35	-6.42	1.07	12.762	0.0813
12	-6.42	-7.49	1.07	12.769	0.0827
13	-7.49	-8.56	1.07	12.776	0.0842
14	-8.56	-9.63	1.07	12.784	0.0839
15	-9.63	-10.7	1.07	13.086	0.0815
16	-10.7	-12.692	1.9922	13.45	0.0777
17	-12.692	-14.684	1.9922	14.127	0.0727
18	-14.684	-16.677	1.9922	14.804	0.0678
19	-16.677	-18.669	1.9922	15.481	0.0627
20	-18.669	-20.661	1.9922	16.212	0.0606
21	-20.661	-22.653	1.9922	16.854	0.0618
22	-22.653	-24.645	1.9922	17.552	0.0630
23	-24.645	-26.638	1.9922	18.25	0.0643
24	-26.638	-28.63	1.9922	18.948	0.0655
25	-28.63	-30.622	1.9922	19.646	0.0668
26	-30.622	-32.614	1.9922	20.344	0.0677
27	-32.614	-34.606	1.9922	20.681	0.0672
28	-34.606	-36.599	1.9922	19.644	0.0658
29	-36.599	-38.591	1.9922	18.96	0.0647
30	-38.591	-40.583	1.9922	18.277	0.0636
31	-40.583	-42.575	1.9922	17.593	0.0625
32	-42.575	-44.567	1.9922	16.91	0.0615
33	-44.567	-46.56	1.9922	16.314	0.0598
34	-46.56	-48.552	1.9922	15.522	0.0574
35	-48.552	-50.544	1.9922	14.819	0.0552
36	-50.544	-52.536	1.9922	14.07	0.0535
37	-52.536	-54.528	1.9922	13.692	0.0525
38	-54.528	-56.521	1.9922	13.288	0.0515
39	-56.521	-58.513	1.9922	12.94	0.0519
40	-58.513	-60.505	1.9922	13.72	0.0537
41	-60.505	-62.497	1.9922	14.404	0.0553
42	-62.497	-64.489	1.9922	15.003	0.0575
43	-64.489	-66.482	1.9922	15.786	0.0604
44	-66.482	-68.474	1.9922	16.483	0.0629
45	-68.474	-70.466	1.9922	17.055	0.0659
46	-70.466	-72.458	1.9922	17.883	0.0693
47	-72.458	-74.45	1.9922	18.586	0.0729
48	-74.45	-76.443	1.9922	19.505	0.0762
49	-76.443	-78.435	1.9922	19.983	0.0807
50	-78.435	-80.427	1.9922	21.365	0.0823

Table 13: 10 MW flexible spar properties, where L, D and t are the length, diameter and thickness of a segment, respectively.

Segment	**Elevation wrt. SWL [m]**		**L [m]**	**D [m]**	**t [m]**
	End 1	**End 2**			
1	15	12.5	2.5	10	0.0832
2	12.5	10	2.5	10.696	0.0837
3	10	7.5	2.5	11.392	0.0842
4	7.5	5	2.5	12.088	0.0847
5	5	2.5	2.5	12.784	0.0850
6	2.5	0	2.5	12.784	0.0850
7	0	-1.07	1.07	12.784	0.0850
8	-1.07	-2.14	1.07	12.784	0.0850
9	-2.14	-3.21	1.07	12.784	0.0850
10	-3.21	-4.28	1.07	12.784	0.0850
11	-4.28	-5.35	1.07	12.784	0.0850
12	-5.35	-6.42	1.07	12.784	0.0843
13	-6.42	-7.49	1.07	13.163	0.0826
14	-7.49	-8.56	1.07	13.648	0.0808
15	-8.56	-9.63	1.07	14.133	0.0789
16	-9.63	-10.7	1.07	14.618	0.0771
17	-10.7	-12.690	1.9895	15.103	0.0745
18	-12.690	-14.679	1.9895	16.005	0.0710
19	-14.679	-16.669	1.9895	16.906	0.0676
20	-16.669	-18.658	1.9895	17.805	0.0668
21	-18.658	-20.648	1.9895	18.657	0.0685
22	-20.648	-22.637	1.9895	19.506	0.0703
23	-22.637	-24.627	1.9895	20.355	0.0720
24	-24.627	-26.616	1.9895	21.204	0.0738
25	-26.616	-28.606	1.9895	22.053	0.0755
26	-28.606	-30.595	1.9895	22.902	0.0773
27	-30.595	-32.585	1.9895	23.783	0.0774
28	-32.585	-34.575	1.9895	22.980	0.0759
29	-34.575	-36.564	1.9895	22.145	0.0743
30	-36.564	-38.554	1.9895	21.310	0.0727
31	-38.554	-40.543	1.9895	20.475	0.0711
32	-40.543	-42.533	1.9895	19.640	0.0695
33	-42.533	-44.522	1.9895	18.805	0.0678
34	-44.522	-46.512	1.9895	17.917	0.0660
35	-46.512	-48.501	1.9895	17.260	0.0639
36	-48.501	-50.491	1.9895	16.559	0.0617
37	-50.491	-52.480	1.9895	15.858	0.0599
38	-52.480	-54.470	1.9895	15.453	0.0585
39	-54.470	-56.459	1.9895	14.878	0.0572
40	-56.459	-58.449	1.9895	14.474	0.0564
41	-58.449	-60.439	1.9895	14.212	0.0571
42	-60.439	-62.428	1.9895	15.134	0.0591
43	-62.428	-64.418	1.9895	15.818	0.0607
44	-64.418	-66.407	1.9895	16.477	0.0629
45	-66.407	-68.397	1.9895	17.197	0.0657
46	-68.397	-70.386	1.9895	17.893	0.0687
47	-70.386	-72.376	1.9895	18.731	0.0719
48	-72.376	-74.365	1.9895	19.498	0.0757
49	-74.365	-76.355	1.9895	20.463	0.0798
50	-76.355	-78.344	1.9895	21.428	0.0841
51	-78.344	-80.334	1.9895	22.431	0.0886
52	-80.334	-82.324	1.9895	23.471	0.0934
53	-82.324	-84.313	1.9895	25.638	0.0983

Table 14: 15 MW flexible spar properties, where L, D and t are the length, diameter and thickness of a segment, respectively.

B Bending Moment RAO - 15 MW Towers

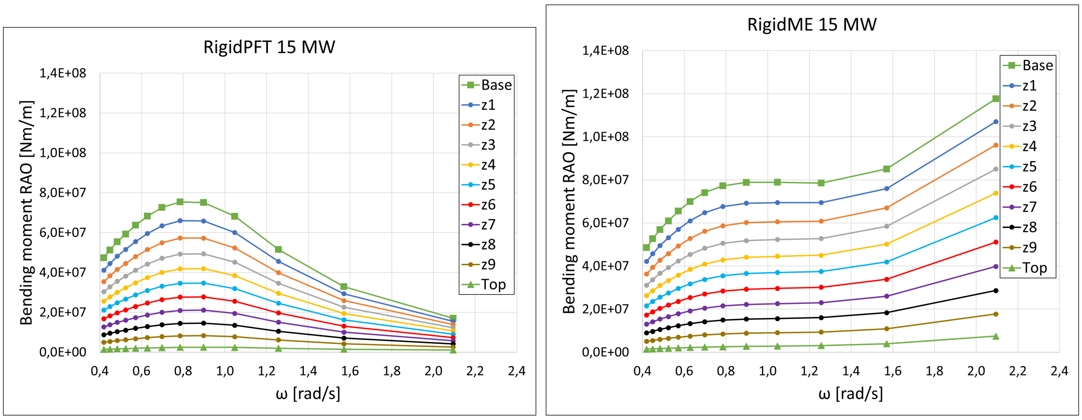

(a) RigidPFT 15 MW (b) RigidME 15 MW

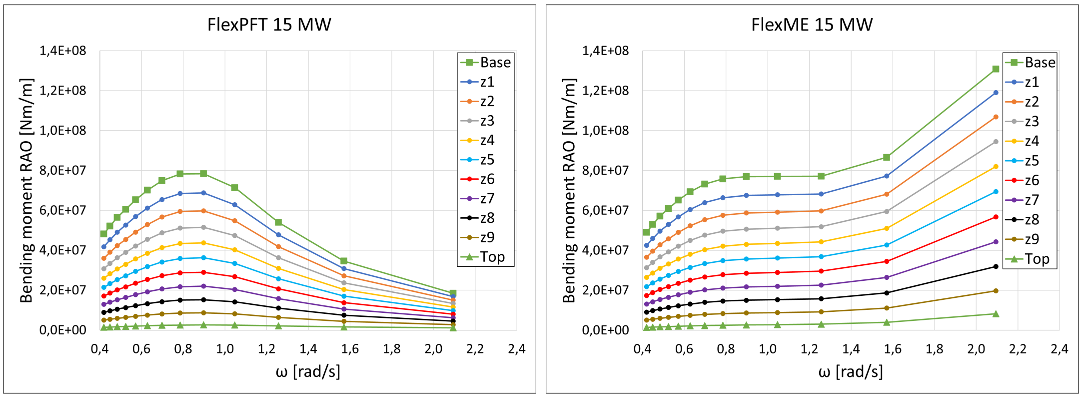

(c) FlexPFT 15 MW (d) FlexME 15 MW

Figure 68: Bending moment RAO for 15 MW towers

C Spectral Analysis - Bending Moment at base of Towers

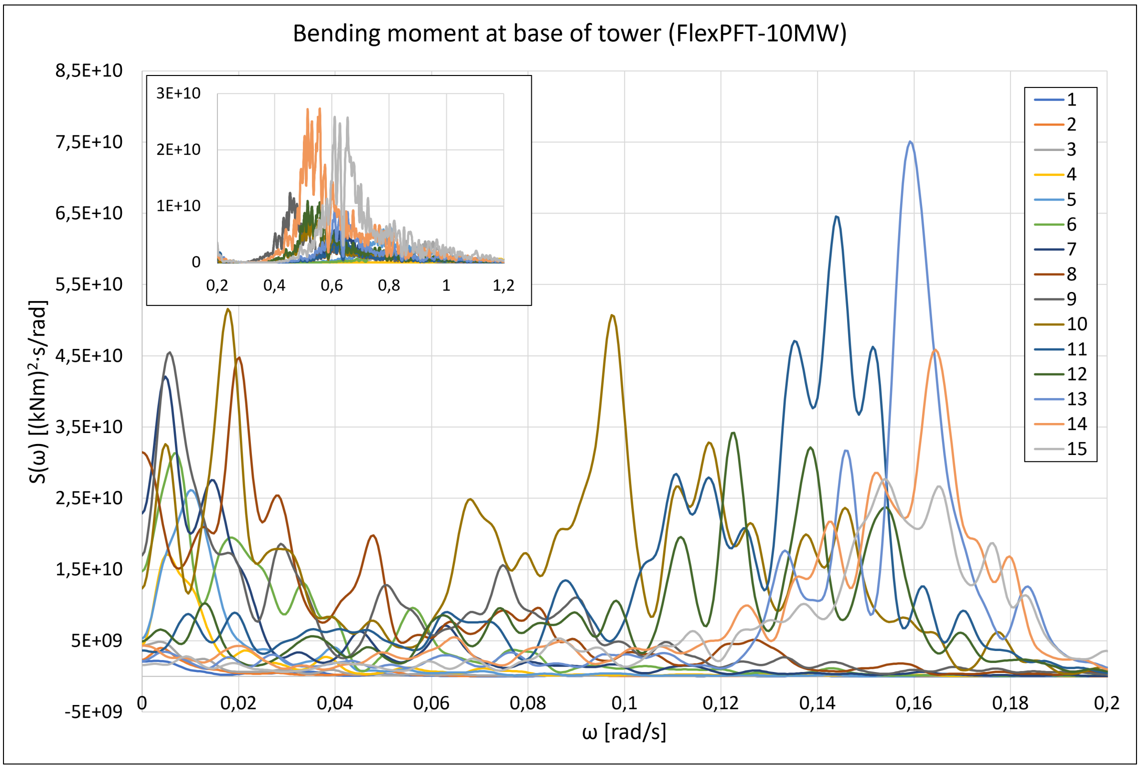

Figure 69: Spectral analysis of tower base bending for FlexPFT-10MW, but all models have similar results in these frequency regions (Condition 1-15 in legend)

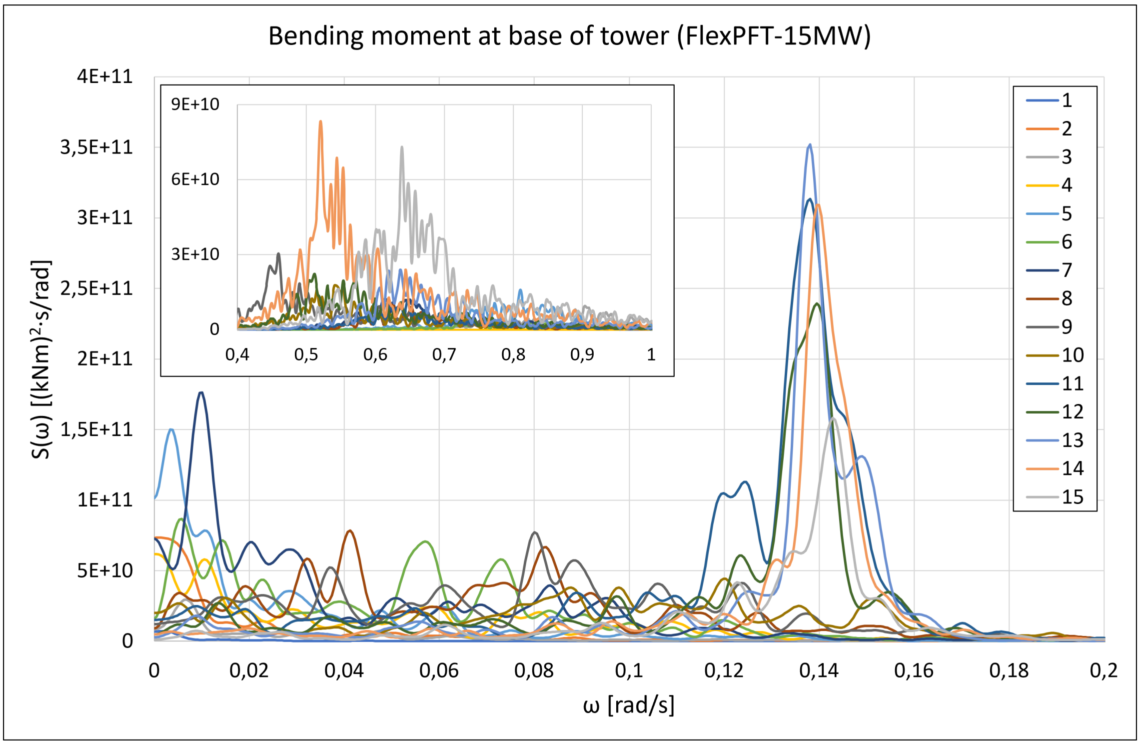

Figure 70: Spectral analysis of tower base bending for FlexPFT-15MW, but all models have similar results in these frequency regions (Condition 1-15 in legend)

Vebjørn Nicholas Brevik

Elasticity, Wave Load Modeling and Upscaling of Spar Floating Wind Turbine

NTNU
Kunnskap for en bedre verden